Author:
Eaton, Andrew

Title:
Nonlinear Dynamics of High-Aspect-Ratio Wings
Using Numerical Continuation

Nonlinear Dynamics of High-Aspect-Ratio Wings

Using Numerical Continuation

By

ANDREW JAMES EATON

Department of Aerospace Engineering
UNIVERSITY OF BRISTOL

A dissertation submitted to the University of Bristol in accordance with the requirements of the degree of DOCTOR OF PHILOSOPHY in the Faculty of Engineering.

DECEMBER 2019

Word count: 57,426

Abstract

High-aspect-ratio wings are of interest to civil aircraft manufacturers, due to the aerodynamic benefit they provide; however, the flexibility of these wings means that nonlinear dynamical phenomena, such as limit cycle oscillations (LCOs), may exist, which cannot be captured by classical tools for aeroelastic flutter prediction. This thesis makes novel contributions by investigating the nonlinear dynamics of high-aspect-ratio wings using numerical continuation techniques, which are path-following methods well-suited for the study of parameter dependancy in nonlinear dynamical systems without using time histories. A fully nonlinear, low-order beam formulation is combined with strip theory aerodynamics, and it is shown that the geometric nonlinearity inherent in high-aspect-ratio wings can be a fundamental driver of undesirable dynamical phenomena, without need for aerodynamic nonlinearity.

A 2 degree-of-freedom (DoF) binary flutter wing is first used as the basis for an analytical and physical discussion, and it is shown that the criticality of the flutter point (i.e. the supercritical or subcritical nature of the Hopf bifurcation) can be changed depending on how the frequencies of the linearised system vary with airspeed. A high altitude, long endurance (HALE) wing is then investigated, and the one-parameter continuation of equilibria and LCOs reveals that complex dynamics exist in this system; the two-parameter continuation of Hopf and periodic fold bifurcations reveals the sensitivity of these dynamics to variations in bending and torsional stiffness. Observations from the 2 DoF wing, relating to Hopf criticality, are investigated in the HALE wing. Finally, the dynamics of a 'free-free' HALE aircraft are investigated; while the continuation of LCOs reveals the flutter point to be relatively benign, detrimental nonlinear phenomena are found to affect the rigid-body flight dynamics due to the presence of periodic fold bifurcations. These undesirable phenomena are shown to be removed by varying torsional stiffness.

DEDICATION AND ACKNOWLEDGEMENTS

First and foremost, I would like to thank Prof. Mark Lowenberg and Prof. Simon Neild for their excellent academic supervision; it goes without saying that, without their guidance, this work would not have been possible. I am indebted to Dr. Chris Howcroft for his support with the aeroelastic modelling, which has been a key enabler for the novelty of this work. I also thank Dr. Etienne Coetzee for his vision for the project and Prof. Jonathan Cooper for providing context within the wider research field. I would also like to thank my fellow QB 2.80-ers; this project has been a very enjoyable experience, which is in no small part due to the excellent working environment at the University. (It won't be so painful when we look back in a few years!) Finally, I thank my friends and family for their encouragement and, most importantly, patience.

This research was funded by the UK Aerospace Technology Institute Agile Wing Integration (AWI) project (TSB-113041). Prof. Simon Neild is supported by an EPSRC Fellowship (EP/K005375/1) and Prof. Jonathan Cooper holds a Royal Academy of Engineering Research Chair.

"Inevitably, underlying instabilities begin to appear."
Dr. Ian Malcolm
Jurassic Park (1993)

AUTHOR'S DECLARATION

I declare that the work in this dissertation was carried out in accordance with the requirements of the University's Regulations and Code of Practice for Research Degree Programmes and that it has not been submitted for any other academic award. Except where indicated by specific reference in the text, the work is the candidate's own work. Work done in collaboration with, or with the assistance of, others, is indicated as such. Any views expressed in the dissertation are those of the author.

SIGNED: ..... DATE: .....

Table of Contents

List of Tables

List of Figures

Figure **Page**

CHAPTER 1

INTRODUCTION

This chapter outlines the motivations for the research and introduces the engineering problem pertaining to flexible, high-aspect-ratio wings. The general themes of the thesis are discussed, and the research aims are stated. The novel contributions are summarised, and a breakdown of the thesis structure is provided, which includes a summary of each chapter.

1.1 Research motivations & themes

The aerodynamic benefit provided by *high-aspect-ratio wings* makes them an attractive option for the aircraft designer. The slender planform of such wings reduces the unwanted effects of tip vortices, and thus, when compared to lower aspect ratio designs, a greater lift-to-drag ratio may be achieved at certain flight conditions. Traditionally, high-aspect-ratio wings have predominantly featured in high altitude, long endurance (HALE) aircraft, seeing use in unmanned applications such as military reconnaissance and communication services relay. Recently, however, there has been an increase in the commercial interest in high-aspect-ratio wings and their applicability to the civil aviation industry [1, 2]. Manufacturers are seeking more economically and environmentally viable aircraft, and solutions located outside of typical design envelopes are being investigated. Figure 1.1 shows the Subsonic Ultragreen Aircraft Research (SUGAR) Volt currently being researched by Boeing, together with the Airbus 2050 concept; both of these aircraft feature high-aspect-ratio wings (the former has an aspect ratio of 19.55[1]). Initiatives such as Flightpath 2050[2] have set challenging targets for the future of civil aviation, requiring ambitious step-changes in technology; high-aspect-ratio wings are among a variety of novel concepts currently being researched in the pursuit of greener aircraft.

[1] For comparison, the aspect ratio of an Airbus A320 is 10.3.

[2] https://ec.europa.eu/transport/sites/transport/files/modes/air/doc/flightpath2050.pdf (last accessed on 29th April 2019).

Figure 1.1: Future aircraft concepts that feature high-aspect-ratio wings, from Boeing (left) and Airbus (right).

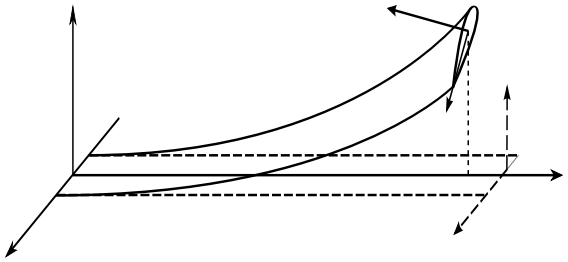

Figure 1.2: Large deformation of a flexible wing, relative to a global coordinate frame.

An inherent and typically undesired characteristic of high-aspect-ratio wings is their *flexibility*. Compared to conventional designs, wings with greater span-to-chord ratios experience greater bending moments and larger deformations under nominal aerodynamic loading. These large deformations are problematic from an *aeroelastics* perspective, as classical toolsets for static and dynamic analysis rely on linear theory and assume wing deformations to be small. When wing deformations are not small, the aeroelastic system becomes *geometrically nonlinear* and, moreover, aerodynamic load vectors become non-negligibly re-orientated relative to the aircraft, acting as a 'follower force' (where lift and drag no longer act solely in the vertical and horizontal directions; see Fig. 1.2). Increased torsional flexibility may also result in outboard wing sections achieving angles of attack large enough for *aerodynamic nonlinearity* (i.e. stall, resulting from flow separation) to be significant. The presence of nonlinearities means that the aeroelastic behaviour of high-aspect-ratio wings cannot be adequately predicted by linear methods, and the use of nonlinear techniques is necessary.

The concept central to this thesis is *aeroelastic flutter* and how it is exhibited by high-aspect-ratio wings. When an aircraft wing exceeds a critically-high airspeed, a self-excited oscillation occurs - caused by a coupling between structural modes and the airflow - which proceeds to grow exponentially. According to linear analysis, such an instability is unbounded; however, this

outcome is not always observed in practice, as nonlinear effects can effectively attenuate the destabilising forces and lead to sustained periodic motions of finite amplitude. Such phenomena are called *limit cycle oscillations* (LCOs), and are a key theme throughout this thesis. While bounded oscillations may appear preferable to the 'linear' flutter outcome, there is evidence in the literature that shows LCOs can also exist *below* the critical flutter airspeed. These undesirable 'subcritical' phenomena cannot be predicted by linear analysis, and thus, if not identified by other means, may compromise the safety of an aircraft flight envelope. Flutter is one of the limiting factors in civil aircraft design; therefore, given the industry trend towards high-aspect-ratio wings, subcritical LCOs (and nonlinear phenomena in general) caused by large flexibility must be better understood and, if possible, captured in the conceptual stages of the engineering lifecycle.

The research in this thesis is conducted within the context of parameter dependancy in smooth, autonomous[3] *nonlinear dynamical systems*, i.e. continuous systems where the states evolve with time (describable using ODEs) and the rate of change is a nonlinear function of the current state. In general, nonlinear systems are less straightforward to analyse than linear systems, as analytical solutions are typically not available, and the possibilities of *closed invariant sets* in state space (e.g. attractors, which describe steady behaviours and prescribe the dynamical flow) can be vastly more complex. Linear systems only permit a single fixed point (i.e. a static equilibrium, where the rate of change is zero) and thus, provided the stability (i.e. the behaviour after a small perturbation) of this is known, the long-term destinations of all dynamical trajectories are easily predicted. In nonlinear systems, coexisting attracting invariant sets are possible, so steady behaviours can be highly dependant on initial conditions. For example, multiple stable equilibria may exist, as could isolated periodic orbits, quasi-periodic orbits (tori) and dense, aperiodic orbits (chaos); the set of initial conditions that flows to a particular attractor is called its *basin of attraction*. Much of the analysis of nonlinear systems exploits the fact that, close to static equilibria, local nonlinearity is usually negligible, and thus nearby dynamics can be approximated using *linearisation*, based on a truncated Taylor series expansion about these points. In truth, all real-life dynamical systems are nonlinear, and any 'linear' system is actually a linearisation about a particular equilibrium. Indeed, engineering systems are typically designed to behave as 'linearly' as possible, so they are amenable to traditional analysis tools; however, this may lead to overly-conservative solutions.

Should the *topology* of the invariant sets in a nonlinear system change when a (time-invariant) parameter is varied, the system is said to have undergone a *bifurcation*. As this parameter boundary is crossed, the dynamical flow in state space qualitatively changes, and thus the behaviour of the system can become markedly different. Identifying bifurcations in parameterised nonlinear systems is crucial, as sometimes the topological changes are drastic and a tiny parameter change results in vastly different dynamics. In the case of aeroelastic systems, a conventional parameter is airspeed, and flutter points coincide with so-called *Hopf bifurcations*, which are characterised

[3]The dynamics of autonomous systems do not depend explicitly on time, and are fully prescribed by the system states; this is in contrast to non-autonomous systems, which may (for example) be subject to periodic forcing.

by the emergence of a periodic solution. Throughout this thesis, *bifurcation diagrams* are used to illustrate the occurrence of bifurcations (and thus where dynamics topologically change), when airspeed is varied, for a variety of different high-aspect-ratio wing configurations.

Numerical continuation describes the family of solution-finding techniques used throughout this thesis. The classical tools available for linear systems, which are fundamentally based on the superposition principle (normal modes, Laplace transforms etc.), are not applicable to nonlinear systems, and other methods must be used. Historically, the nonlinear analysis of flutter has typically comprised: i) static calculations, solving for deformed equilibria at specified airspeeds, ii) stability analysis, based on linearisation about these points, and iii) numerical integration (i.e. time-stepping/simulation) for obtaining LCO behaviour near the identified flutter point. This last part, in particular, is computationally expensive and is not guaranteed to fully capture all possible dynamics within a system. Numerical continuation techniques are an attractive alternative, as they can be used to *directly* obtain equilibria and periodic solutions of dynamical systems, as a parameter is varied, using a path-following procedure based on a predictor-corrector method. Exhaustive integration is thus avoided, and complex bifurcation diagrams can be readily constructed. Continuation techniques are often used in many nonlinear research areas (for example, in the analysis of fighter aircraft flight dynamics), and are increasingly being exploited in aeroelastic contexts. Moreover, while the techniques have been scarcely used in the civil aviation industry, they are well placed to become a more conventional tool for the conceptual design of future passenger aircraft.

1.2 Research aims

The fundamental aims and objectives of this thesis are to

- employ numerical continuation techniques for the investigation of low-order nonlinear aeroelastic models of high-aspect-ratio wings;
- extend the current knowledge regarding the geometric nonlinearity of high-aspect-ratio wings and its effect on dynamical phenomena;
- establish how readily high-aspect-ratio wings exhibit LCOs below the flutter point, and investigate the physical drivers of such behaviour;
- investigate how geometric nonlinearity affects the rigid-body flight dynamics of an aircraft with high-aspect-ratio wings.

Overall, the results from this work are intended to help direct further research, and will provide evidence as to why geometric nonlinearity must be adequately captured early on in the design and analysis of flexible, high-aspect-ratio wings.

1.3 Novel contribution

The novel contribution made by this thesis lies in the extensive application of numerical continuation for investigating the nonlinear dynamics of flexible, high-aspect-ratio wings. Numerical continuation has seldom been used for this purpose; at the time of submission, a single study predating this thesis [3] is found that applies the techniques in this context (this will be discussed in Section 2.4). Notable points of novelty of this thesis include: i) the extensive use of two-parameter continuation for obtaining Hopf and periodic fold bifurcations in a high-aspect-ratio wing, ii) the investigation of Hopf criticality in high-aspect-ratio wings using a combined analytical and physical approach, and iii) the use of continuation with a full aircraft model with flexible, high-aspect-ratio wings. At the time of submission, the journal and conference publications associated with this thesis are as follows:

- Eaton, A. J. *et al.*, "Numerical continuation of limit cycle oscillations and bifurcations in high-aspect-ratio wings," *Aerospace*, vol. 5(3), 78, 2018 [4].
- Eaton A. J. *et al.*, “Flutter of High-Aspect-Ratio Wings using Numerical Continuation”, in *Proceedings of Royal Aeronautical Society 5th Structural Design Conference, Manchester, UK,*, 2016 [5].

The novelty of this work is largely enabled by use of the theory developed by Howcroft *et al.* [6], which allows flexible beam-like structures, such as high-aspect-ratio wings, to be modelled using minimal states, and thus enables the construction of a low-order aeroelastic formulation that is well suited for the use of numerical continuation.

1.4 Thesis breakdown

This thesis is intended to be accessible to a reader whom is familiar with concepts from aeroelasticity and linear dynamics, but does not have expertise in nonlinear dynamics. As such, full mathematical discussions of general nonlinear dynamical theorems are not presented; for in-depth treatment of these, the reader is directed to a number of comprehensive texts, by Kuznetsov [7], Guckenheimer and Holmes [8], and Wiggins [9]. A useful entry-level book, which presents a very accessible discussion of nonlinear phenomena in a variety of different contexts, has been written by Strogatz [10].

A breakdown of the chapters is as follows:

- **Chapter 2** discusses the background concepts that serve as prerequisites to the latter chapters. Terminology used throughout the thesis is defined, e.g. see Section 2.1.2 for the definition of nonlinear flutter. Limit cycle oscillations (LCOs), Hopf and periodic fold bifurcations are discussed. Numerical continuation techniques are overviewed and contextualised

within the research. Finally, the literature most relevant to high-aspect-ratio wings is reviewed.

- **Chapter 3** investigates the criticality, i.e. the supercritical or subcritical nature, of Hopf bifurcations occurring at the flutter point of nonlinear aeroelastic systems. An analytical approach is applied to a simple 2 degree-of-freedom (DoF) binary flutter wing model featuring structural nonlinearity. Physical insights are then related to Hopf criticality, and use of numerical continuation investigates how criticality can be changed by varying structural damping or stiffness. General trends, which relate Hopf criticality to the convergence of the system mode frequencies, are discussed.

- **Chapter 4** is derived from Ref. [4] and investigates a high altitude, long endurance (HALE) wing modelled using the theory of Howcroft *et al.* [6]. Numerical continuation explores the complexity of the dynamics that can exist due to geometric nonlinearity alone, without stall or unsteady aerodynamics. The use of two-parameter continuation is employed to obtain dynamical behaviours over large wing stiffness ranges, via the continuation of Hopf and periodic fold bifurcations. Observations from Chapter 3 are extended.

- **Chapter 5** investigates the nonlinear dynamics of a 'free-free' HALE aircraft based on the high-aspect-ratio wings studied in Chapter 4. Trim solutions of the nominal, flexible aircraft are compared to the equivalent rigid case. Numerical continuation is then used to explore the complete flight dynamics of the flexible aircraft, accounting for the aeroelastic instability of the wings. Particular attention is paid to the rigid-body flight dynamics and the impact of varying the wing torsional stiffness.

- **Chapter 6** provides a short summary of the previous chapters, draws more general conclusions, proposes extensions for further research, and discusses the future outlook for numerical continuation and high-aspect-ratio wings in the civil aviation industry.

CHAPTER 2

BACKGROUND THEORY & LITERATURE

This chapter discusses the background theory and literature relevant to the research. The phenomenon of aeroelastic flutter is discussed within the context of dynamical systems theory, and the technique of numerical continuation is overviewed. Finally, the existing literature that investigates the nonlinear dynamics of high-aspect-ratio wings is reviewed.

2.1 Aeroelasticity & flutter

Flexible structures, when subjected to airflow, can deform. *Aeroelasticity* (a portmanteau of 'aerodynamic' and 'elasticity') describes the physical interaction between aerodynamic loads and the restoring forces resulting from elastic strain [11–14]. Aeroelastic systems are encountered in a wide range of real-life situations, including civil engineering structures [15], helicopter rotors [16], energy harvesting systems [17], and the respiratory mechanisms of snoring [18]. In all such systems, an airflow aerodynamically loads a flexible structure, causing it to elastically deform, which in turn affects the aerodynamic loading, and so on.

Aeroelastic performance is a key factor in the design of an aircraft. The desirability of lightweight airframes, together with the limits of material stiffness, means that the wings of an aircraft are not rigid and their in-flight shape may be different from that seen on the ground. Achieving optimal aerodynamic load distribution, in the cruise condition, is vital for maximising fuel efficiency, and thus accurate predictions of deformation under nominal aerodynamic loading are highly desirable. Critically, correctly determining the airspeed at which the static aerodynamic loads overcome the ultimate load of the wings is essential for the specification of safe flight envelopes.

The fundamental interactions that occur in aeroelastic systems are best illustrated using Roderick Collar's well-known 'loads triangle' (see Fig. 2.1) [19]. *Static aeroelastic equilibria*, which

occur when all loads in a particular system are balanced and there is no motion (for example, consider a steady wing shape at a fixed airspeed) can be calculated solely using aerodynamic and elastic loads, whereas the inclusion of inertial forces can yield complete dynamic behaviours (for example, the time-varying deformation of a wing caused by a gust). In many references, the triangle in Fig. 2.1 is extended to reflect advancements made since Collar's time, capturing interactions with aircraft flight controls and thermal effects ('aero-servo-elasticity' and 'aero-thermo-elasticity' respectively, the latter being particularly important for supersonic and hypersonic aircraft [20]).

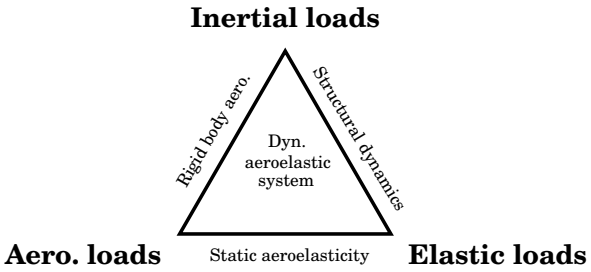

Figure 2.1: Collar's triangle of aeroelastic loads [19]; a dynamical aeroelastic system requires the capture of aerodynamic, elastic and inertial forces.

Aeroelastic effects are typically undesirable in aircraft, as the presence of flexibility can lead to a number of detrimental phenomena that, if not accurately predicted, may significantly compromise safety within the flight envelope. Indeed, aircraft failures caused by aeroelasticity can be traced back to the pioneers of aviation; the 2nd unsuccessful flight of Samuel P. Langley's vehicle is widely attributed to the torsional divergence of the wing [21]. This flight attempt predated the Wright brother's successful attempt in 1903. Other detrimental aeroelastic phenomena include the reduction, or possibly the reversal, of control surface effectiveness and, pertinently to this thesis, flutter, which is discussed separately below. The increasing use of lightweight composites in civil aircraft design may lead to more flexible aerostructures, which means that successful prediction of aeroelastic behaviour looks to be an engineering challenge for the foreseeable future, especially given the industry trend towards high-aspect-ratio wings. There are currently many research efforts investigating solutions that mitigate detrimental effects of flexibility (for example, the use of support structures [22, 23] or hinged wingtips[1] [24]) or seek to exploit them for performance benefit (so-called 'aeroelastic tailoring' [25]). Clearly, design solutions that involve the use of additional mass involve weight penalties, so the implementation of such solutions necessitates cost/benefit studies that consider the aircraft as a whole.

Aeroelastic flutter is a phenomenon that, according to traditional textbooks, describes a particular way an aeroelastic equilibrium can become unstable to small disturbances. More specifically, it pertains to the critical condition where ***a tiny perturbation, to a static equilibrium, leads***

[1] Typically, these are targeted more for gust load alleviation.

to oscillatory[2] ***motion that does not decay***. In aircraft wings, the classical mechanism for this is an interaction between flexible bending and torsional structural modes, which combine with the airflow to create a reinforcing feedback loop (often called *binary* flutter; see Fig. 2.2 (a) for a cross-sectional illustration). At pre-flutter ('subcritical') airspeeds, the energy imparted by a tiny disturbance leaves the system, the oscillations of the wing decay, and the net damping (which comprises damping from both the structure and the airflow) is positive; see Fig. 2.2 (b). At post-flutter ('supercritical') airspeeds (c), energy is extracted from the airflow, oscillations grow exponentially, and the net damping is negative. In reality, tiny perturbations are unavoidable due to the unsteadiness of airflow, so divergent oscillations are always observed in real-life systems once the flutter condition is satisfied. Importantly, the oscillations are *self-excited*, and have no dependency on external forcing.

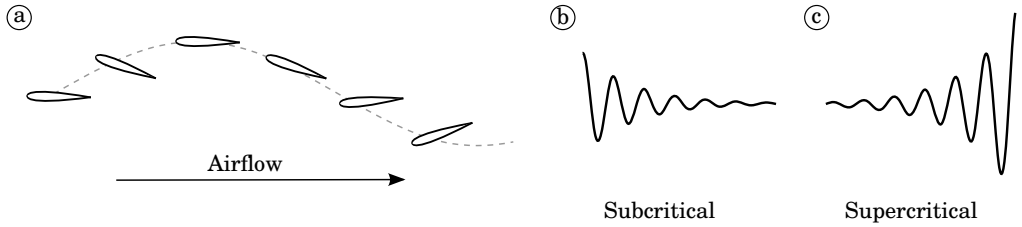

Figure 2.2: Illustrations of (a) a flutter interaction between bending and torsional modes (this example the shows the two motions in-phase) and time histories at (b) subcritical and (c) supercritical airspeeds.

In practice, flutter interactions are not restricted to the flexible modes of wings, and analyses must account for aircraft dynamics as a whole. Indeed, the first major flutter study, which dates back to 1916 in the UK, documented oscillations involving flapping elevators and the twisting of a fuselage; the aircraft in question was a Handley Page 0/400 biplane [13]. Incidentally, while flutter has historically been most closely associated with aerospace applications, the most well-known example is actually the Tacoma Narrows bridge failure, which is often incorrectly attributed to resonance caused by periodic forcing [15, 26].

According to 'conventional', linear flutter analysis (described below in Section 2.1.1), the divergent oscillations that occur at supercritical airspeeds (Fig. 2.2, c) are always unbounded and grow until structural failure. Thus, from the perspective of the civil aviation authorities, flutter is a catastrophic failure mode of a commercial aircraft and is a highly critical design factor. Before aircraft certification is granted, strict safety criteria must be met, via a combination of modelling, ground vibration tests, and flight tests, to demonstrate that flutter oscillations do not occur at any flight condition. Attempts at eliminating flutter, or at least ensuring it occurs at an

[2]This oscillatory characteristic is the reason why flutter is typically described as a 'dynamic' aeroelastic instability in textbooks. In contrast, divergence, which comprises non-oscillatory motion, is referred to as a 'static' instability. The requirement for oscillations indicates the necessary inclusion of inertial loads; thus, flutter involves all three vertices in Collar's triangle shown in Fig. 2.1.

unachievable airspeed, may comprise the separation of wind-off frequencies of structural modes that are susceptible to interaction; in wings, this can be achieved by various means, typically by tailoring the spanwise stiffness or mass distributions. Active control systems that aim to suppress flutter oscillations are the subject of ongoing research efforts [27]; also see the NASA X-56 demonstrator.

The classical *flutter airspeed* of an aeroelastic system is defined as the *lowest airspeed* where the flutter condition is met, i.e. where the oscillatory response to tiny perturbations no longer decays. While this definition provides sufficient basis for the discussion of traditional (i.e. linear) flutter dynamics, it is not adequate in the context of nonlinear flutter dynamics; thus, it is instructive to generalise the phenomenon within the broader setting of dynamical systems theory, and introduce some important concepts using terminology similar to Kuznetsov [7], etc.

Definition 2.1. ***Generalised flutter airspeed in an aeroelastic system.*** *Let $x^t = \phi^t(v)\, x_0$ describe the evolution of a dynamical aeroelastic system, parameterised by $v \in \mathbb{R}^+$ (airspeed), where $\{x_0, x^t\} \in X$ and $t \in \mathbb{R}^+$ is time. Let x^* be a static equilibrium (fixed point) of the system, such that $\phi^t(v)\, x^* = x^*$ for all t, let ϵ be an infinitesimal perturbation, and let $\xi_0 = x^* + \epsilon$.*

Thus, the flutter airspeed v_f is defined such that

- *for $v < v_f$ (subcritical airspeeds), x^* is asymptotically stable for all ξ_0, and*
- *for $v > v_f$ (supercritical airspeeds), this is no longer the case and, moreover, the motion is oscillatory.*

In the above definition, x refers to the *state vector*, which completely describes the state of the aeroelastic system at a given instant of time, and X refers to the *state space* of the system, i.e. the set of all states that describes all possible instances of the system. The equilibrium x^* can be called an *invariant point*, as it is unmoved under the operation of ϕ^t. Moreover, since all trajectories converge to x^* for $v < v_f$, it is an *attractor* at subcritical airspeeds. Let $U \subset X$ define the *basin of attraction* of x^*, i.e. the set of all initial conditions in X that flow to x^* as t evolves.

In this generalised context, the implications of flutter are local, as it concerns infinitesimal perturbations and makes no prescription for dynamics of the system away from the equilibrium. Should other attractors exist in X, the *global* stability characteristics of the system may not be described by the local stability of x^*. Thus, v_f refers to the flutter airspeed of the equilibrium, not the system, and further exploration of the dynamics is necessary to establish the behaviour at any given airspeed. Note that, since the motion is oscillatory, the unstable motion must occur on at least a 2D manifold in X.

Throughout this thesis, dynamical aeroelastic systems are modelled as a series of continuous, autonomous ODEs (*vector fields*). In the following sections, x is assumed to comprise the n generalised coordinates that describe the position and velocity of structural and aerodynamic

states. In all cases, the coordinate frame is chosen such that $x = 0$ describes an undeformed, static system.

2.1.1 Linear systems

A linear aeroelastic dynamical system may be expressed in the general, parameterised first-order form

$$\dot{x} = A(v)\,x, \tag{2.1}$$

where $x \in \mathbb{R}^n$, $A(v)$ is a linear operator and $v \in \mathbb{R}^+$ is airspeed. The classical form for a linear aeroelastic system is often written as $M\ddot{q} + C\dot{q} + Kq = 0$, where m, C and K are the mass, damping and stiffness matrices, respectively. By a change of basis, the general solution to (2.1) for a given initial condition x_0 can be written as

$$x(t) = c_1 v_1 e^{\lambda_1 t} + \cdots + c_n v_n e^{\lambda_n t}, \tag{2.2}$$

where $\lambda_{1\ldots n}$ and $v_{1\ldots n}$ are the eigenvalues and eigenvectors of A, and $c = [v_1 \cdots v_n]^{-1} x_0$. Thus, the flutter airspeed v_f of (2.1) is defined as the lowest airspeed where A possess a complex-conjugate pair of eigenvalues with zero real part (i.e. a pair of *critical eigenvalues*, λ_c). For $v < v_f$, all λ have negative real part, and thus all perturbations asymptotically decay to the origin as $t \to \infty$. At $v = v_f$, there exists a 2D centre subspace or linear manifold E^c embedded in X, described by the linear span of the eigenvectors of λ_c (i.e. the *flutter mode*), to which the system decays and exhibits simple harmonic motion (see Fig. 2.3, a). For $v > v_f$, one pair of complex eigenvalues has positive real part, an unstable subspace E^u now exists, and the origin is unstable (Fig. 2.3, b). Note that the illustrations in Fig. 2.3 are visualisations in 3D space; in reality, a system of size $n \geq 4$ is necessary for the capture of binary flutter. Furthermore, the subspaces corresponding to the stable eigenvalues are not fully shown.

In order to express an aeroelastic system in the linear form (2.1), all inertial, damping and stiffness loads, in both the structure and the aerodynamics, must necessarily vary proportionally to the system states. Thus, (2.1) does not capture any change in the modal properties of the structure, or change in the aerodynamic profile, that could occur *due to the static deformation of the system* as airspeed changes. For this reason, the flutter airspeed is independent of the deformation. Industry flutter analysis, i.e. the analysis used in conventional civil aircraft design [28, 13], is based on these linearity assumptions, as the structural stiffness of conventional wings is sufficiently large such that large static deformation does not occur; the flutter condition can thus be approximated at the undeformed shape of the wing. The various flutter analyses readily available in MSC NASTRAN[3], a widely used finite-element (FE) modelling tool approved by the certification authorities for flutter prediction, are all eigenvalue solvers of some description that assume no dependency between deformation and airspeed [13].

[3] These are the 'P-method', the 'K-method' and the 'P-K method'; see Section 5.4 in Ref. [13] for comparisons.

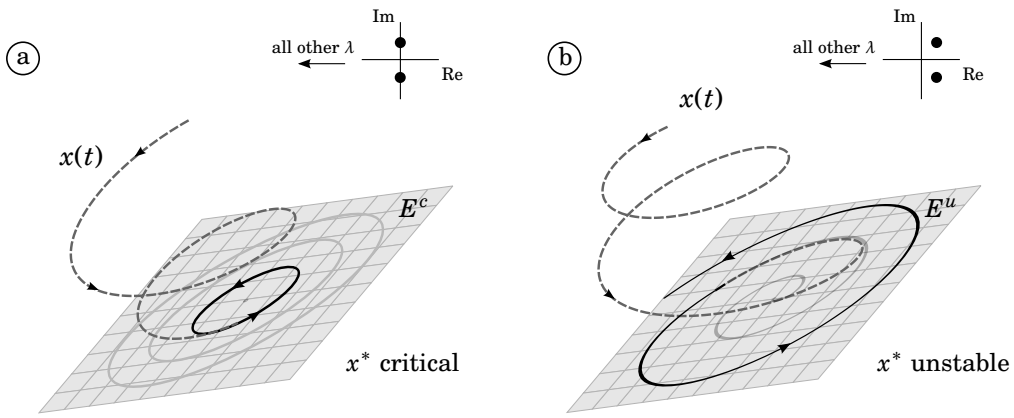

Figure 2.3: Illustration of the 2D subspace (linear manifold) for (a) $v = v_f$ and (b) $v > v_f$ in a linear aeroelastic system.

2.1.2 Nonlinear systems

For aeroelastic systems where the above-mentioned linearity assumptions can no longer be made (e.g. due the presence of large deformations), the governing equations necessarily become nonlinear, and (2.1) can no longer be used to describe the system.

A general nonlinear aeroelastic system, parameterised in terms of airspeed, may be expressed in the first-order form

$$\dot{x} = f(x, v), \tag{2.3}$$

where f is a nonlinear function of x. In this case, to obtain the stability to small perturbations and thus v_f, *linearisation* is performed about the equilibria in the system, which approximates local dynamics to the form of (2.1). This is achieved by the calculation of the $n \times n$ *Jacobian* matrix, which comprises the first-order partial state derivatives (the validity of neglecting higher-order terms is addressed below).

Definition 2.2. ***Nonlinear flutter airspeed*** *refers to the airspeed where perturbations to the linearisation of (2.3),*

$$\dot{\xi} = J(x, v)\big|_{x^*}\, \xi, \tag{2.4}$$

leads to oscillations that do not decay, and thus the Jacobian matrix, which is defined as

$$J = \mathrm{D}f = \begin{pmatrix} \frac{\partial f_1}{\partial x_1} & \cdots & \frac{\partial f_1}{\partial x_n} \\ \vdots & \ddots & \vdots \\ \frac{\partial f_n}{\partial x_1} & \cdots & \frac{\partial f_n}{\partial x_n} \end{pmatrix}, \tag{2.5}$$

has a complex-conjugate pair of eigenvalues with zero real part λ_c.

According to the Hartman-Grobman theorem [9, 29], the dynamics described by (2.4) are topologically equivalent[4] to those of (2.1), near the equilibrium, provided that the equilibrium is *hyperbolic*, i.e. Re $\lambda_{1..n} \neq 0$. Thus, the solutions of (2.4), which take the form of (2.2), are locally equivalent to the solutions of (2.3), provided that the system is not on the precise flutter point (i.e. $v \neq v_f$). In other words, for $v < v_f$ and $v > v_f$, the dynamics predicted by linearisation are qualitatively valid near the equilibrium. The 2D subspaces E^c and E^u, which are now described by the critical eigenvectors of the linearised system, are *tangential* to a centre manifold W^c and an unstable manifold W^u, respectively, in the nonlinear system. At the flutter airspeed $v = v_f$, where the neglected nonlinear terms are critical, W^c is of particular importance for characterising the exact stability of the equilibrium (this is further discussed in Chapter 3).

An important note on terminology is required at this stage. As described above, a *flutter mode* corresponds to an eigensolution, defined by λ_c and v_c, of an aeroelastic system; thus, it is a true mode of either (2.1) or (2.3), in the strictest dynamical theory sense. In aeroelastics contexts, the term 'mode' is typically used more generally to also describe the ways a continuous structure, within an aeroelastic system, deforms. In this thesis, *flutter mode* refers to a true system mode, whereas *structural modes* refers to the constituent deformations that the system mode comprises; this distinction will be important for the discussion in Section 3.3.

The inclusion of nonlinear terms in (2.3) essentially means that any changes in the (structural) modes and aerodynamic characteristics, caused by deformation before flutter, can be captured. Thus, (2.3) can include non-homogeneous terms, independent of x, that result in the existence of non-trivial (i.e. highly deformed) equilibria. Most commonly, a term parameterised by v and α_0 (root angle of attack) is included to produce a net lift and thus increasing static deformation as airspeed increases. In this case, v_f is found by linearising about a new x^* at each airspeed increment. For the case of flexible high-aspect-ratio wings, non-trivial equilibria can have a significant effect on the flutter airspeed (further discussed in Section 2.4), so nonlinear treatment is necessary.

In summary, the flutter airspeed of a nonlinear system (alternatively, a nonlinear flutter airspeed) refers to the flutter airspeed obtained by linearising a system about non-trivial equilibria that may vary with airspeed. Put simply, *nonlinear flutter accounts for the large static deformation and the resulting modal changes* that a nonlinear system (e.g. a flexible, high-aspect-ratio wing) may experience under aerodynamic loading. If the system does not statically deform with airspeed, the flutter airspeed is determined by the linear part of the system; however, as was described in the generalised definition, *the implications of nonlinear flutter are strictly local to the equilibrium*.

[4] There exists an invertible, continuous mapping (i.e. a homeomorphism) between the two vector fields [7].

2.2 Nonlinear aeroelastic dynamics

As discussed in Section 2.1, the oscillations that characterise flutter are the result of a reinforcing feedback loop created by a critical modal interaction. In a linear system (2.1), this interaction is sustained for any deformation of the system, as neither the structural modes nor aerodynamics are affected, and thus the oscillations grow unbounded. The stability of the equilibrium x^* to infinitesimal perturbations thus characterises the response to any size disturbance; therefore, once the flutter airspeed is obtained for a linear system, all behaviour can be qualitatively predicted, for any size of perturbation, depending on the airspeed. This is not true for the nonlinear system (2.3), however, as changes in the structural modes or aerodynamics, caused by deformation, may prevent the critical interaction from sustaining indefinitely. The higher-order terms neglected in the linearisation (2.4) become important once the system is sufficiently far from the equilibrium; when the time-varying deformation extends beyond this local region, the dynamics are not captured.

Expressing the above statements more generally, *in a nonlinear system (e.g. a flexible, high-aspect-ratio wing), the critical modal interactions that cause flutter are dependant on both airspeed and system deformation*.

2.2.1 Limit cycle oscillations (LCOs)

Given the discussion above, it follows that the intermittent existence of critical interactions, during the time-varying deformation of a nonlinear system, can settle to periodic motion with finite amplitude. In such a case, an interaction exists for part of a period in such a way that the energy extracted from the airflow, over one cycle, is equal to energy leaving [30]. This type of periodic solution is called a limit cycle oscillation (LCO) and is a *closed invariant set*, S, in state space, as trajectories that lie on the solution do not leave, i.e. for $x_0 \in S$, $x(t, x_0) \in S$ for all t. Other general terms from dynamical systems theory include *closed orbit* or *isolated orbit*. LCOs are strictly nonlinear phenomena and should not be confused with the periodic orbits of undamped linear systems (e.g. solutions on the centre subspace shown in Fig. 2.3).

Definition 2.3. ***Limit cycle oscillation***[5] ***(LCO)*** *refers to the periodic solution*

$$\dot{x} = f(x, v), \quad x(t+T) = x(t) \tag{2.6}$$

where there are no other periodic solutions nearby. The smallest $T > 0$ that satisfies (2.6) is the period of oscillation.

The nonlinearity that could limit (or indeed, amplify) the amplitude of a particular flutter oscillation may be structural, aerodynamic, inertial, etc. or some combined effect. Should the

[5] Such solutions are simply referred to as 'limit cycles' in general nonlinear dynamics literature; the acronym 'LCO' is commonplace in aerospace applications and is thus used throughout this thesis.

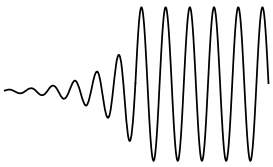

Figure 2.4: Illustration of a limit cycle oscillation (LCO). These finite-amplitude oscillations are strictly nonlinear phenomena.

angle(s) of attack in a system become large enough for flow separation, the resulting limited oscillations are commonly referred to as 'stall LCOs' or 'stall flutter'; such phenomena have been closely associated with flexible helicopter rotors [31]. The effects of structural nonlinearity are related to the changing modal properties and are discussed in more detail in Chapter 3. Regardless of the physical source of the nonlinearity, however, the resultant dynamical phenomenon i.e. a closed orbit, is the same.

Nonlinear oscillations are not restricted to airspeeds beyond the flutter point. Since, in nonlinear systems, critical interactions are a function of *both* airspeed and deformation, LCO phenomena are possible at airspeeds where the static equilibrium is stable. For this to happen, the airspeed is not high enough to cause flutter, but is sufficiently large to cause interactions if the modal properties of the system are suitably altered. Thus, the system can enter a sustained, closed orbit at an airspeed below the flutter airspeed if it is suitably deformed about the (stable) subcritical equilibrium. Subcritical LCOs are highly undesirable in aircraft, as they may occur within the operational flight envelope; in the best case, fatigue effects can compromise the longevity of the structure, and in the worst case, catastrophic failure can occur.

As with static equilibria, LCOs may be stable or unstable to infinitesimal perturbations. In general terms, LCO stability is obtained via the construction of a Poincaré section Σ, of dimension $n-1$, at some point on the orbit in state space (see Fig. 2.5); this section allows the construction of a discrete, 'first-return' map, which describes the evolution at $t+T$ and reduces the invariant set (i.e. the LCO) to an invariant point on Σ. The stability of this point to perturbations corresponds to the stability of the orbit and is indicated by *Floquet multipliers* [7, 10, 29]; should these multipliers all lie within the unit circle, the LCO is stable. If they do not, the point and orbit are unstable and nearby trajectories diverge, as is illustrated by the dashed line in Fig. 2.5. The dynamics on Σ will be revisited in Section 2.2.3 when discussing the bifurcations of periodic orbits.

The mathematical phenomena responsible for closed periodic orbits in nonlinear systems are typically *Hopf bifurcations*, which will be introduced in Section 2.2.2. Generally, the existence of closed orbits in a particular system is non-trivial to prove, although an analytical criterion exists for 2D systems (when $n = 2$), namely the Poincaré-Bendixson theorem [10]. However, as will become evident, LCOs are practically a certainty in nonlinear aeroelastic systems, at least theoretically, should there exist a flutter point.

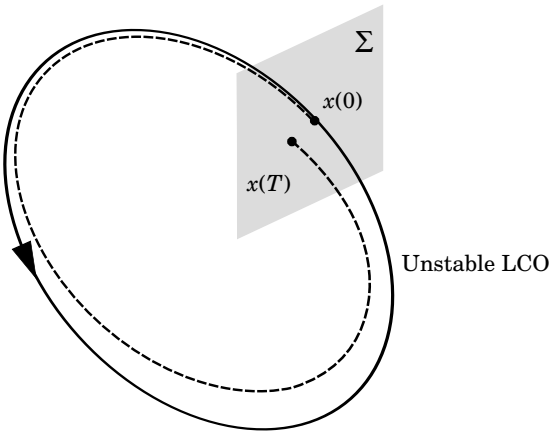

Figure 2.5: Isolated orbit in state space, featuring Poincaré section.

2.2.2 Hopf bifurcations

In the general field of nonlinear dynamics, a *bifurcation* describes any topological change to the invariant sets of system (2.3) caused by parameter variation. A particular class of bifurcation is characterised by the emergence of new solutions due to the parameter perturbation of a *nonhyperbolic equilibrium point*, i.e. cases where linearisation yields critical eigenvalues and the count of $\lambda_c \neq 0$.

As discussed in Section 2.1.2, flutter occurs when λ_c comprises a complex-conjugate pair. According the Andronov-Hopf theorem, should the genericity conditions

1. $\frac{\mathrm{d}}{\mathrm{d}p} \operatorname{Re} \lambda_c \neq 0$ ('transversality' condition)
2. $l_1 \neq 0$ ('non-degeneracy' condition)

both hold, where $p \in \mathbb{R}$ is a smooth parameter, and the quantity l_1 is the 'first Lyapunov coefficient' [7, 32] (further discussed in Chapter 3), then the dynamical system, close to the equilibrium, is topologically equivalent to the *normal form*[6] of the Hopf bifurcation, which is

$$\begin{pmatrix} \dot{u}_1 \\ \dot{u}_2 \end{pmatrix} = \begin{pmatrix} p & -1 \\ 1 & p \end{pmatrix} \begin{pmatrix} u_1 \\ u_2 \end{pmatrix} \pm \left(u_1^2 + u_2^2\right) \begin{pmatrix} u_1 \\ u_2 \end{pmatrix}. \tag{2.7}$$

At $p = 0$, a Hopf bifurcation occurs in (2.7), and there are two distinct scenarios that can exist, depending on the sign of the cubic terms, which is determined by l_1. Should these nonlinear terms be negative, a stable limit cycle exists for $p > 0$ (*supercritical* Hopf), whereas if they are positive, an unstable limit cycle exists for $p < 0$ (*subcritical* Hopf). For completeness, it should be noted that aeroelastic divergence, i.e. the static (non-oscillatory) analogue of flutter, corresponds to occurrence of a *pitchfork* bifurcation, which has a 1D normal form.

[6] The simplest representation of a dynamical phenomenon, where all non-essential nonlinear terms are removed, leaving the so-called 'resonant terms' at the equilibrium.

In nonlinear aeroelastic systems, supercritical and subcritical Hopf bifurcations typically occur at the flutter point as per Fig. 2.6 (b & c), where the linear/degenerate[7] case (a) is also included for comparison. In both nonlinear cases, the static equilibrium loses asymptotic stability, and an LCO solution emanates with finite amplitude. In the supercritical case (b), the LCO solution is stable and exists for $v > v_f$, whereas in the subcritical case (c), the solution is unstable and exists for $v < v_f$. In both cases, near the bifurcation point, LCO amplitude grows $\propto \sqrt{|v_f - v|}$. In the latter, a *periodic fold* bifurcation (further discussed in Section 2.2.3) is also illustrated, resulting in a stable LCO solution of large amplitude.

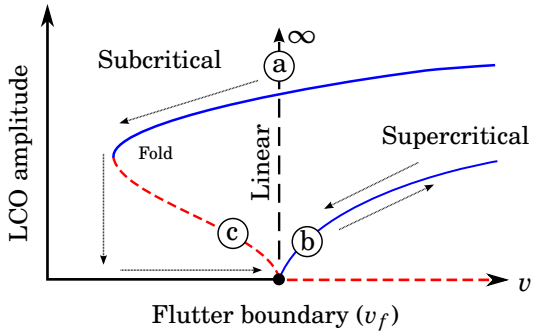

Figure 2.6: Generic flutter point possibilities: (a) linear/degenerate, (b) supercritical, and (c) subcritical. In cases (b & c), a Hopf bifurcation occurs at v_f.

The supercritical Hopf (Fig. 2.6, b) is the most favourable flutter outcome as, in this case, the system smoothly transitions to a stable LCO solution once the critical boundary has been exceeded, and this can be reversed by reducing the airspeed. In the subcritical case (c), the system becomes attracted to the large amplitude solution, and oscillations can only be removed by reducing the airspeed to below the fold airspeed. Thus, a hysteresis loop exists in this case. Additionally, the presence of two attractors in the subcritical region means the system has a dependency on initial conditions below the flutter airspeed. Should a sufficient disturbance occur (e.g. from a gust), a system that is settled on the static equilibrium may enter the basin of attraction of the large amplitude LCO solution.

The detrimental characteristics of the subcritical Hopf means that it is *highly undesirable* in an aeroelastic system. Indeed, the effects are often referred to as 'bad LCO' or 'detrimental nonlinearity' in the literature (e.g. Ref. [33]); it thus follows that accurate prediction of flutter criticality, in a given system, is sought after. This analysis is typically not straightforward, though, as the type of Hopf bifurcation is not captured by the linearisation about the equilibrium. Provided that the system in question is of sufficiently low-order, analytical tools are available (one of these is demonstrated in Chapter 3); typically, however, numerical methods must be used, often involving the simulation of LCO behaviour near the bifurcation point (this is not the case

[7] See Section 3.2 for details.

in this thesis). In physical experiments (e.g. wind tunnel tests), obtaining flutter criticality is not a trivial task, either; if the nonlinearity in the system is weak, the amplitude of the LCO solution grows rapidly, and thus the deformation may quickly exceed the survivable bounds of the test rig. This may be true even if the Hopf is supercritical. Moreover, since the damping around the equilibrium is very small near the bifurcation point, steady behaviours may be tedious to obtain without the aid of some kind of finite disturbance, which may exacerbate the risk of structural failure.

From the above, it is clear that understanding the fundamental drivers of Hopf criticality, in a flutter context, is a key factor in the safe design of flexible, high-aspect-ratio wings. Specifically, understanding the sensitivity of criticality in particular systems to certain physical design parameters (for example, the stiffness distribution of a wing) is of interest, as it may be feasible to 'convert' an undesirable subcritical bifurcation to the desirable supercritical case by design (an example of this, from the literature, is discussed in Section 2.4.4).

It is possible that the flutter point in Fig. 2.6 is not the only Hopf bifurcation in a system. Should the airspeed continue to increase beyond the flutter airspeed, the critical eigenvalues may return to the left half plane, and thus the equilibrium regains stability. (In flutter terminology, this re-stabilising is referred to as a 'hump mode', which is reflective of how the damping plot appears in MSC NASTRAN.) If the Hopf conditions are met, an LCO solution emanates from this secondary bifurcation point, which may comprise an additional branch of solutions, or may join to the LCO solution originating from the flutter point. In this latter case, LCOs no longer exist at the re-stabilised airspeed.

Figure 2.6 is called a *bifurcation diagram* because it illustrates the location of bifurcation points in the combined state-parameter space of a system. The horizontal axis in this type of diagram is the parameter being varied (in this case, airspeed), and the vertical axis is typically some projection of the system states (for example, wing tip displacement or twist), or simply one of the states themselves. Bifurcation diagrams are ubiquitous in the general field of nonlinear dynamics and are used throughout this thesis.

2.2.3 Bifurcations of periodic orbits

The periodic fold that accompanies the subcritical Hopf in Fig. 2.6 (c) is a type of *periodic orbit bifurcation*, i.e. a bifurcation that affects periodic solutions, as opposed to equilibria. In the case of a fold, an unstable and a stable periodic solution collide, resulting in the annihilation of both (at the bifurcation point, a singular half-stable orbit exists). From a basic physics perspective, such phenomena are guaranteed to occur in aeroelastic systems when the flutter point is subcritical; at zero airspeed, there is no energy to extract from airflow, so an LCO cannot exist. The airspeed at which the fold occurs is not easily obtainable using time histories, as the basin of attraction of the stable solution diminishes to zero at the bifurcation point.

The generalised behaviours illustrated in Fig. 2.6 are typically only representative of be-

haviour relatively close to the equilibrium point. In practice, in both supercritical and subcritical Hopf cases, other nonlinearities can cause additional periodic fold bifurcations to occur, at higher amplitudes, which may result in several stable LCOs coexisting at the same airspeed; this will be demonstrated in Chapter 4. The possibility of subsequent periodic folds is an important consideration, as it means that subcritical LCOs, which always exist in the subcritical Hopf case, could also exist when the Hopf is supercritical. For this to happen, the stable solution emanating for $v > v_f$ (Fig. 2.6, b) folds and extends to below v_f before folding again. This possibility means that proof of a supercritical Hopf bifurcation does not rule out subcritical LCOs and thus, in addition to Hopf criticality, analysis of the LCO solutions is also highly important.

The bifurcations that affect periodic orbits can be described by revisiting the discrete map derived from the Poincaré section shown in Fig. 2.5. Nonlinear maps can undergo bifurcations themselves, and while this is a large field in itself, the general theory is not unlike that of vector fields. Similarly, different phenomena occur due to the movement of linearised eigenvalues (or, if the map is a Poincaré section, Floquet multipliers) as a parameter is varied. Three possibilities, which are characterised by eigenvalue crossings across the unit circle, are shown in Fig. 2.7 and discussed below. For detailed mathematical description, see Refs. [7, 9, 29], for example.

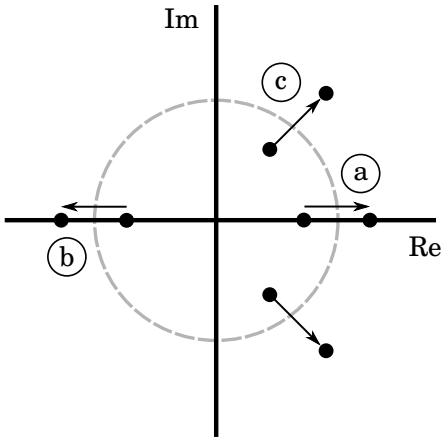

Figure 2.7: Bifurcations of periodic orbits, characterised by the movement of Floquet multipliers: (a) periodic fold, (b) period-doubling and (c) Niemark-Sacker (torus).

If a single, real multiplier passes through +1, as shown by Fig. 2.7 (a), the result is either a periodic fold or a branch point. These results are completely analogous to the fold and pitchfork bifurcations of equilibria; the former is also called a saddle-node or 'flip' bifurcation. On the section Σ, a fold is indicated by the collision of two fixed points. If a multiplier passes through -1 (b), however, a *period doubling* bifurcation occurs; in this case, the original period orbit changes stability, and a solution with a doubled period emanates from the bifurcation point. Unlike the periodic fold, this bifurcation has no static analogue. In this case, two additional points are

created on Σ and the original point changes stability.

If a complex-conjugate pair of multipliers cross the unit circle (c), a *Neimark-Sacker* bifurcation occurs. In this case, the stability of the periodic solution changes and a quasi-periodic solution is created. The term quasi-periodic describes the fact that, while the solution can be broken into periodic components, at least two periods are not commensurable, so the overall motion is never repeated. The invariant set of such a solution has the topology of a torus[8] and is represented by a closed orbit on Σ.

Any new solutions, created by the bifurcations shown in Fig. 2.7, may subsequently undergo bifurcations themselves. Indeed, the 'zero airflow' argument pertaining to the existence of periodic folds (made above) applies to any non-static solution, and thus any solution that extends to low airspeeds must fold back at some point. Also, a series of periodic bifurcations may also rapidly increase the complexity of the dynamics in a short parameter interval. For example, chaotic dynamics, which comprise dense, aperiodic solutions with very strong sensitivity to initial conditions, is often attributed to a 'cascade' of period doubling bifurcations [10]. Chaos is difficult to conclusively prove in high-dimensional systems, although an analytical criterion exists (called the Lyapunov exponent) which is effectively a measure of how rapidly two very close initial conditions diverge as time evolves. A chaotic attractor, which is sometimes called a *strange attractor*, has fractal geometry; the Poincaré section through such an object shows some kind of complex, filled structure. Some examples of chaos in aeroelastic systems are described by Lee *et al.* [34].

All of the bifurcations discussed so far are *local*, in the sense that they relate to a linearisation about some kind of fixed point; either a static equilibrium or a fixed point on a Poincaré section. Another class of bifurcation exists, called *global* bifurcations, which cannot be characterised in this way; examples of these are homoclinic and hetroclinic bifurcations. Phenomena of this type have not been encountered in this thesis and are not discussed further.

2.3 Numerical continuation

Nonlinear dynamical phenomena, such as LCOs, cannot be captured by conventional flutter tools. A complete picture of the parameter-dependant dynamics, i.e. a bifurcation diagram, as shown in Fig. 2.6, in a given nonlinear aeroelastic system must be constructed using wholly nonlinear methods. Perhaps the most obvious approach is to numerically integrate the system (using e.g. Runge-Kutta or Newmark-β), in time, to obtain $x(t)$ at a variety of different airspeeds, in an attempt to identify qualitative changes in the long-term behaviour. However, using time histories is a cumbersome approach in practice, as

- there is no guarantee that $x(t)$ converges to a steady solution during a given simulation,

[8] Neimark-Sacker bifurcations are often referred to as *torus bifurcations* for this reason.

- transient dynamics, which are not the main interest, are a costly means to an end, and
- the possibility of multiple attractors means that the testing of many initial conditions, at each airspeed, may be required before all possible behaviours are obtained.

The above inconveniences are compounded by the fact that, close to the flutter point, the damping in the aeroelastic system is very small. Further to this, unstable solutions (such as the red LCO solution in Fig. 2.6) cannot be explicitly obtained, unless the system is integrated in reversed time.

Numerical continuation, a well-established family of methods widely applied in the field of nonlinear dynamics [35–39], present a general approach that avoids use of 'brute-force' simulations. The basic objective of continuation techniques, when used in this context, is to numerically follow the path of (or 'continue') a particular invariant set (e.g. equilibria or periodic orbits) over the variation of a parameter, given a starting condition, using a *predictor-corrector* method. The exact approach used in a particular setting is specific to the solution to be obtained (see Sections 2.3.1 - 2.3.3 below), but in all cases it can be related to the implicit solutions of the nonlinear system of algebraic equations

$$G(y,\, p) = 0, \tag{2.8}$$

where $y \in \mathbb{R}^n$ and $p \in \mathbb{R}^m$. Here, G is defined such that the solution of (2.8) defines the invariant set of interest. While several predictor-corrector schemes exist, the most common is called *pseudo-arclength* continuation, which is illustrated in Figure 2.8. The basic components of this scheme are as follows. From a known solution point y^j, which satisfies (2.8), a *prediction* $\hat{y}^{j+1}$ of the next point is made using the tangent vector (a), the length of which is called the step-size. From here, a *correction* (b) is performed to find the next solution y^{j+1}, which comprises finding the intersection of an orthogonal surface with the targeted implicit curve; this is achieved by using Newton-Raphson iterations. The rate of convergence then prescribes the step-size of the next prediction, which is the final stage of the step (if convergence fails, the same step is attempted using a smaller step prediction).

A particular continuation analysis is conventionally described in accordance to the value of m, i.e. the number of parameters that are free to vary. For example, the continuation of equilibria and periodic orbits, with respect to airspeed, are *one-parameter* continuations, as $p \in \mathbb{R}$. In this case, the total solution space has dimension $n+1$. The continuation of Hopf points and periodic folds (which are special instances of equilibria and periodic orbits) requires $p \in \mathbb{R}^2$ and are thus called *two-parameter* continuations (here, the solution space has dimension $n+2$). This type of continuation is potentially a very powerful means of the obtaining the regions of dynamical behaviour of a system over large envelopes of design parameters; in aeroelastic applications, the continuation of Hopf points with respect to airspeed and a chosen secondary parameter (for example, stiffness or root angle of attack, etc.) shows the variation of the flutter airspeed with respect to that 2^{nd} parameter. Two-parameter continuation is demonstrated in Chapter 4.

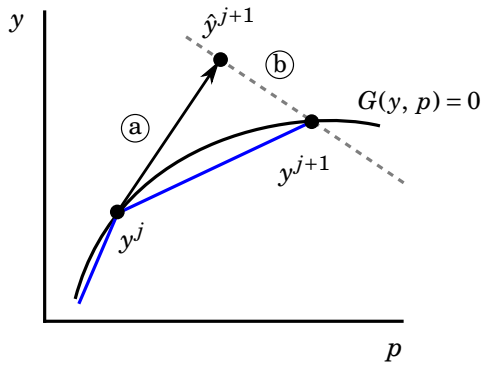

Figure 2.8: Illustration of pseudo-arclength continuation, comprising (a) a predictor step and (b) a corrector step.

The popularity of numerical continuation, in general nonlinear dynamics research contexts, has been intrinsically linked to the success of the software AUTO [40], which was first developed by Eusebius Doedel in the late 1970s. Since these early implementations, which were written in FORTRAN, several software packages emerged, with increased functionality and user accessible, notably AUTO 97 [41], AUTO 2000 [42], MATCONT [43] and DST [44], the last two being implementations in MATLAB /Simulink. Continuation tools have become a powerful influence on the development of dynamical systems theory, and are widely used in many fields of science, as shown in Ref. [38]. In this thesis, Computational Continuation Core (COCO) is used [45], which is a MATLAB-based framework that builds on the functionality of previous software, and is aimed at open-ended application and ongoing development. The source code of COCO is currently freely available[9]. Sections 2.3.1-2.3.3 provide a brief overview of the generic numerical continuations that have been used in this thesis; these are derived from Refs. [7] & [29].

In aerospace engineering, numerical continuation has been prominently exploited in applications concerning nonlinear flight dynamics [46–48] and, more recently, landing gear dynamics (for example, Ref. [49]). In aeroelasticity, an early use can be be found in Ref. [50], where the nonlinear dynamics of a two-dimensional aerofoil are examined. More recent examples can be found in Strganac *et al.* [3], Dimitriadis [51–53], Vio *et al.* [54], and Shukla & Patil [55]. In industry contexts, continuation techniques do not see widespread use, although they may be well-placed to meet future demands of transport aircraft; an overview of the applicability to the conceptual design phase is provided by Sharma *et al.* [56]. The use of numerical continuation for aero-servo-elastic stability and control in helicopter rotor blades at AugustaWestland (now Leonardo Helicopters) is documented in Refs. [57, 58].

It is worth noting that the benefits of continuation techniques are not necessarily exclusive to numerical models. Implementation of the techniques, in an experimental context, is a focus of

[9] https://sourceforge.net/projects/cocotools/ (last accessed on 19th October 2018).

ongoing research (for example, Refs. [59, 60]); in such a setting, in order to safely obtain unstable solutions, non-invasive feedback control must necessarily be implemented to prevent the physical system from diverging.

2.3.1 Equilibria continuation

The most fundamental use of continuation, in a nonlinear aeroelastic context, is to obtain the static equilibria in a system for a range of airspeeds. Consider the parameterised system (2.3); in this instance, the equation

$$f(x, v) = 0 \tag{2.9}$$

describes the smooth locus of static equilibria over the variation of v. Clearly, this curve is only non-trivial if (2.3) contains non-homogeneous terms that are a function of v. While the variable parameter in this case is typically airspeed, the variation of another parameter is sometimes of interest; for example, it could be the magnitude of a vertical tip load, which is applied to deform a wing while airspeed remains constant.

The algebraic system defined by (2.9) can be directly implemented in the form of (2.8) and the stability of each step can be obtained from the Jacobian of (2.3), which is necessarily computed as part of the pseudo-arclength method. Hopf bifurcations (i.e. flutter boundaries), or indeed any other bifurcations of equilibria, can be detected by the construction a test function, $\psi(x, v)$, that is satisfied at the bifurcation condition. In the case of a Hopf, the function

$$\psi_H(x, v) = \prod_{i>j} \left(\lambda_i(x, v) + \lambda_j(x, v)\right) \tag{2.10}$$

is used, which is equal to zero when there exists a complex-conjugate pair of Jacobian eigenvalues with zero real part.

2.3.2 Periodic orbit continuation

The periodic orbits (i.e. LCOs) of the nonlinear system (2.3) can be similarly obtained for the variation of v. In this case, solutions can be written as the boundary problem

$$\frac{\mathrm{d}x}{\mathrm{d}\tau} = T f(x, v), \qquad x(0) = x(1) \tag{2.11}$$

where τ is a time variable rescaled in accordance with period T. Since (2.3) is autonomous, a *phase condition* must be imposed in order to uniquely define a solution. Most commonly, the condition

$$\int_0^1 \left\langle x(t), x_{\mathrm{old}}(t) \right\rangle \mathrm{d}\tau = 0, \tag{2.12}$$

is used, which essentially ensures that the next solution has the smallest phase difference relative to the old (i.e. previous) solution [7]. The unique boundary value problem defined by (2.11) & (2.12) can be solved by a number of discretisation methods; AUTO and COCO both use orthogonal collocation [61], which approximates the orbit as a piecewise polynomial on a mesh, typically with 2-7 collocation points on each interval. The complete discretised boundary value problem can then be implemented in the form of (2.8), similarly with test functions for bifurcations.

2.3.3 Bifurcation point continuation

The principles for equilibria and period orbit continuation can be extended to the continuation of specific bifurcations; here the problem takes the generic form

$$G(y, v) = \begin{pmatrix} f(x, v) \\ \psi(x, v) \end{pmatrix} = 0. \tag{2.13}$$

2.3.4 Practicalities

A number of general comments can be made about the practical considerations of using numerical continuation techniques.

- The attraction of continuation techniques is their ability to obtain invariant sets (and their stability) in a dynamical system without extensive use of numerical integration. They do not capture the basin of attraction of these sets, nor do they capture the characteristics of any transient dynamics. Thus, a complete nonlinear analysis of a particular system should also include simulations at selected test points in state-parameter space.
- Quasi-periodic motions, i.e. the solutions emanating from Neimark-Sacker (torus) bifurcations, cannot be easily obtained.
- Efficient setup of a continuation scheme may sometimes depend on an *a priori* knowledge of the implicit solution curve $G(y, p) = 0$. In practice, upper/lower limits for the variable step size and a maximum number of Newton iterations must be defined such that a balance is struck between speed and accuracy. Clearly, a solution featuring many intricate folds necessitates small steps, although this may mean that more trivial parts of the solution are obtained slowly.
- From a computational standpoint, a significant factor can be the cost of evaluating the function that returns $\dot{x}$, i.e. $f(x, v)$. If this function is expensive, it is beneficial for the user to supply the derivatives (i.e elements of the Jacobian matrix) of the system, with respect to both state and parameter, as otherwise there will be an extensive reliance on finite-differences. The continuation of periodic orbits may be particularly slow in this case, depending on the chosen discretisation parameters (e.g. the number of meshes and collocation points). This is obviously sensitive to the number of states, n.

- By definition, continuation requires an initial solution. This solution is usually obtained from some trivial parameter value (e.g. zero airspeed); from here, equilibria and then LCOs are subsequently obtained. However, it is possible that isolated solutions ('isolas') exist in a system, which are not smoothly connected to any trivial solutions; in practice, these are impossible to detect without some kind of physical insight into the system, or an initial 'brute-force' simulation approach.

2.4 Literature review for high-aspect-ratio wings

As a general field, nonlinear aeroelasticity has been an active and expanding research area in recent decades [33, 62–67]. This can be mainly attributed to a combination of i) the increasing use of more flexible structures in engineering applications, and ii) the rapidly reducing costs of computation. The ubiquity of aeroelastic systems also means that interest in the phenomena often extends beyond aerospace applications (for example, Ref. [17]). The growth of the field is also evidenced by a recent textbook by Dimitriadis [30], a title dedicated to nonlinear aeroelasticity, which appears to be the first of its kind. In traditional aeroelastics textbooks (e.g. Refs. [11–14]), the discussion of nonlinearity is either nonexistent or limited to a few paragraphs; the multidisciplinary nature of aeroelasticity means that rigorous linear treatment is usually sufficient introduction to the subject.

A fundamental aim of many nonlinear studies, regardless of the field, is to determine whether the inclusion of nonlinear terms is even necessary for the sufficient capture of system behaviours. Clearly, should the approximate predictions made by (cheaper) linearised analysis be satisfactory for a given application, fully nonlinear analysis is not necessary. When this is not the case, the objective is to i) determine how many nonlinear terms should be included, and ii) understand how detrimental nonlinear effects can be avoided and if favourable effects can be exploited. In an aeroelastics context, nonlinear studies often (unsurprisingly) focus on stability considerations, i.e. the prediction of flutter and LCOs.

As touched upon in Section 2.3, in the absence of a control system, the nonlinearity in a generic aeroelastic system can be broadly characterised as either *structural* or *aerodynamic*. The most basic example of the latter is flow separation (dynamic stall), which leads to aerodynamic loads that no longer linearly increase with effective angle of attack [31]. Shock waves, resulting from transonic flows, are another physical source of aerodynamic nonlinearity [33].

Structural nonlinearity is often commonly attributed to stiffness characteristics and describes instances where the force-deformation relationships in a structure are no longer linear. The terms 'hardening', 'softening' and 'freeplay' are commonly used to describe the nature of this type of nonlinearity; this last case being characterised by the existence of a 'dead zone', a region where the restoring force remains constant. A common test bed for these nonlinearities, in aeroelastics research, comprises a single aerofoil section, constrained in heave and pitch by cubic springs,

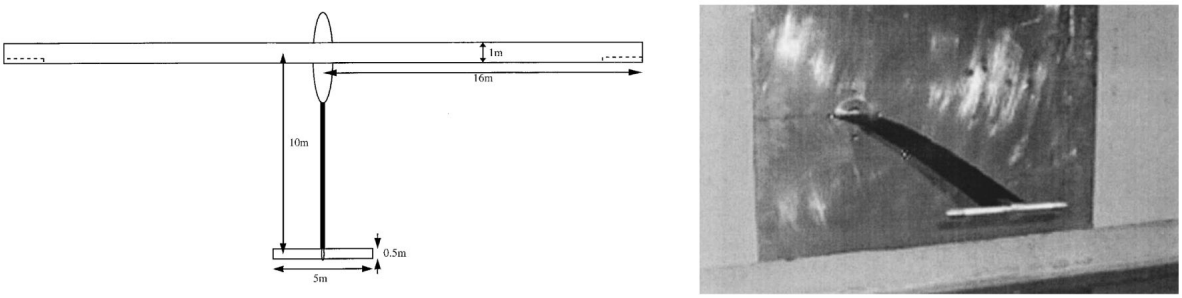

Figure 2.9: High-aspect-ratio wings prominent in the literature, studied by Patil *et al.* [71] (left) and Tang & Dowell [74] (right).

often featuring a control surface. This simple system has demonstrated highly complex behaviour, and is well documented by Lee *et al.* [34]. These local nonlinearities, which are characterised as *concentrated* nonlinearities, often exist in the mechanisms for control surfaces, or in connections to pylons, engines, or external stores etc.

In contrast to the above, the structural nonlinearity inherent in high-aspect-ratio wings is characterised as a *continuous* nonlinearity. Due to their slender nature, the behaviour of high-aspect-ratio wings can be approximated to that of a flexible 1D beam; for this type of structure, it is well established that out-of-plane (flapwise), in-plane (chordwise) and torsional modes can couple nonlinearly as the beam undergoes large deformations, due to a nonlinear relationship between strain and displacement gradient [68]. The nonlinear effect is therefore evident when the continuous wing deforms as a whole and, to reflect this, is often described as a 'geometric' nonlinearity. Aerodynamic nonlinearity due to stalling effects may also exist in slender wings, and is particularly important should the twisting of the wing become very large [69]. Incidentally, the fundamental theories that describe the structural and aerodynamic nonlinearities inherent in high-aspect-ratio wings were both developed in the context of helicopter rotor blades.

The first significant research efforts specifically pertaining to high-aspect-ratio wings predate the current civil industry interest. In the late 1990s and early 2000s, a series of pioneering studies were published by Patil *et al.* [70–73] and Tang & Dowell [74–77], motivated by the interest in high altitude, long endurance (HALE) aircraft, which are very light vehicles designed for unmanned flight. The subject of these initial studies was either a numerical wing derived from a 'Daedalus' aircraft configuration (Fig. 2.9, left) or an experimental wing featuring a tip mass (Fig. 2.9, right). Both of these flexible wings demonstrated nonlinear phenomena and consequently became the subject of several more recent investigations. To this day, the test data in Ref. [74] remains the most important set of wind tunnel results pertaining to nonlinear high-aspect-ratio wings. The findings of these early studies are of particular interest and are further discussed later.

2.4.1 Low-order structural modelling

The numerical treatment of high-aspect-ratio wings, in the above-mentioned studies, comprised the use of nonlinear 1D beam equations, derived from the earlier work of Hodges & Dowell [68] or Hodges [78]. According to the original paper from 1974 [68], the equations of motion of a rectangular wing, without cross-sectional warping, can be written as

$$EI_2 v'''' + (EI_2 - EI_1)\big(\phi(w + w_0)''\big)'' + m\ddot{v} + M\ddot{v}_{x=L} = \frac{\mathrm{d}F_v}{\mathrm{d}x}, \tag{2.14}$$

$$EI_1(w + w_0)'''' + (EI_2 - EI_1)\big(\phi v''\big)'' + m\ddot{w} + M\ddot{w}_{x=L} - Mg\delta(x - L) = \frac{\mathrm{d}F_w}{\mathrm{d}x}, \tag{2.15}$$

$$GJ\phi'' + (EI_2 - EI_1)(w + w_0)''v'' + mK_m^2\ddot{\phi} = \frac{\mathrm{d}M_x}{\mathrm{d}x}, \tag{2.16}$$

where v, w and ϕ are the in-plane, out-of-plane and torsional deformations, EI_1 and EI_2 are the out-of-plane and in-plane bending stiffnesses, and GJ is the torsional stiffness. These equations are not used in this thesis; however, it useful to state them here for future reference, particularly noting that the structural nonlinearity in the formulation is dependant on the term (EI_2 - EI_1). For the full definition of the other symbols, see Appendix A.1. While this formulation appears in a number of studies [74, 76, 75, 79–81], a geometrically exact, intrinsic formulation was subsequently developed by Hodges [78], allowing a more accurate description of large beam deformation [70–73]; this formulation was subsequently further developed, see Ref. [82]. Another beam formulation, developed by Crespo da Silva [83], has also been used for modelling of high-aspect-ratio wings [3, 81]. Recent surveys of HALE aircraft, which describe a number of frameworks for full aircraft modelling, can be found in Refs. [1, 67].

The research in this thesis is similarly conducted using low-order 1D beam models. Specifically, the work in Chapters 4 & 5 uses the novel nonlinear beam formulation developed by Howcroft *et al.* [6]. The reader is directed to Ref. [6] for comprehensive treatment; however, a mathematical summary will be provided in Chapter 4. The fundamental approach of this method is to describe the deformation of a slender wing using a basis of shape functions, which span the full length of the beam, prescribing local sets of Euler angles that are defined in an intrinsic coordinate frame. A kinematic description of a wing is thus achieved without discretising it along its span, which is in contrast to finite-element methods; the approach is thus analogous to the Rayleigh-Ritz technique that is ubiquitous in linear structural modelling (e.g. Ref. [14]). The main attraction of the method of Howcroft *et al.* [6] is that very few structural states are required to describe a given system; favourable computational comparisons with NASTRAN and an FE implementation of Hodges' formulation [78] can be found in Ref. [6]. For a given test example, the Hodges formulation uses 414 states, whereas the present formulation required 15 to satisfy the same convergence criterion. This low number of system states is well-suited for numerical continuation techniques; thus, the use of this formulation is a key enabler for the novelty of this thesis.

2.4.2 Low-order aerodynamic modelling

The works of Patil *et al.* [70–73] and Tang & Dowell [74–77] coupled low-order beam models with a semi-empirical 2D aerodynamic model based on that of ONERA [69], which describes finite-state unsteady aerodynamic loads in the form of ODEs and requires parameters derived from experiment or CFD (for example, Ref. [80]). Other low-order aerodynamics models include those described by Refs. [84] and [85]. The slender planform of high-aspect-ratio wings means that the assumption of strip theory aerodynamics, i.e. which assumes that flow in the spanwise direction is negligible, is a reasonable approximation; indeed, for the HALE wing, 3D effects have been shown to be negligible, even at high static deformations [72].

The aerodynamics in this thesis are implemented using linear, quasi-steady 2D strip theory. The 'quasi-steady' assumption means that the aerodynamic loading on each panel is, at any given instance of time, the same as that on the strip with constant position and velocity [14]; thus, the loads are prescribed entirely by the states describing structural position and velocity, and there is no need for aerodynamic states. The use of quasi-steady aerodynamics is not a limitation of the modelling; in this thesis, it is selected for computational reasons (see Section 6.2 for discussion). The assumption of quasi-steady loads does not prohibit the investigation of geometric nonlinearity, which is the primary aim of this research.

2.4.3 Effect of nonlinearity on flutter airspeed

An immediate point of interest, pertaining to the nonlinearity in high-aspect-ratio wings, concerns the effect on the flutter airspeed (i.e. the oscillatory stability to small perturbations); in other words, understanding the conditions where nonlinear analysis (comprising linearisation about deformed equilibria, see Section 2.1.2), will predict a significantly different boundary to that from purely linear analysis (Section 2.1.1). Ahead of addressing this question with specific findings from the literature, it is useful to highlight the following basic observation. When the nonlinear system (2.1.2) is linearised about the origin (i.e. $x^* = 0$), the flutter result is identical to the linear system (2.1.1), regardless of the nonlinear terms. This is obviously the case when (2.1.2) is homogeneous ($x^* = 0$ is an equilibrium for all v), but will also occur in a non-homogeneous case if $x^* = 0$ coincides with the flutter point. For example, consider a cantilevered, flexible wing that deforms with airspeed; should this wing undergo flutter as it reaches the approximate 'undeformed' shape, the boundary will be very close to the linear prediction (this is observed in Ref. [74]). Thus, the presence of strong nonlinearity, in itself, does not explicitly equate to a large discrepancy in flutter prediction compared to the strictly linear case.

Patil *et al.* [71] presented an investigation into the nonlinear aeroelasticity and flight dynamics of the HALE aircraft (Fig. 2.9, left). The linear (i.e. undeformed) flutter airspeed of the 16m half-wing is calculated and compared to a series of nonlinear (i.e. deformed) cases where gravity and root angle of attack α_0 are non-zero. In all instances, nonlinear flutter occurs at a lower airspeed than the linear prediction of 32.21 m/s (as can be seen in Fig. 2.10, left); a discontinuity

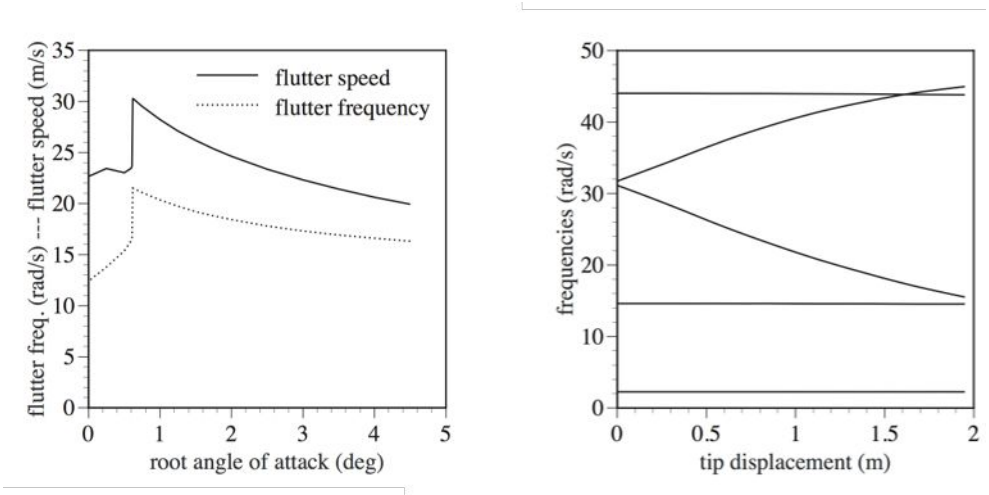

Figure 2.10: From Patil *et al.* [71]: variation of flutter airspeed with α_0 (left) and variation of wind-off structural frequencies with vertical tip displacement (right) of the HALE wing.

is observed at $\alpha_0 = 0.61°$, which is the condition that causes flutter to occur when the wing shape is close to the planar shape. (This result is used as a basis for discussion in Chapter 4.) A vertical tip force is applied to the wind-off, undeformed wing to illustrate how the structural frequencies change with out-of-plane deformation (Fig. 2.10, right). The torsion and in-plane modes (which, critically, gain components from one another as the wing deforms) significantly vary as tip displacement increases, and this is the direct cause for the detrimental flutter results; the original torsion mode lowers to become close to the 2nd out-of-plane bending mode, and thus the critical modal interaction that causes flutter occurs at a lower airspeed.

Another study by the same authors [70] further investigated the HALE wing, but for two variations of in-plane bending stiffness, specified such that the (wind-off) in-plane frequency is placed above/below the torsional frequency respectively. In both cases, the higher-frequency mode increases with deformation and the lower-frequency mode decreases. In both cases, the flutter airspeed is below the linear result (a reduction of almost 50% is seen from the stiffer case). As with the previous study, this is attributed to the critical combination of the torsion/in-plane modes. Results from a 'curved beam' linear analysis show good agreement with the fully nonlinear case, demonstrating that the deformed shape is the dominant factor for flutter. A study by Patil & Hodges [72], which was completed around the same time but published a few years later, demonstrates that the detrimental flutter results in Ref. [70] are also obtained using a higher fidelity 3D aerodynamic model.

A paper published by Tang & Dowell [76] similarly focuses on the HALE wing. Specifically, it investigates whether the physical means by which a deformed equilibrium is created affects the flutter result. Static deformation is produced via four different means: *i*) a tip mass with

inertial and gravity effects, ii) a tip mass with gravity effects only (i.e. a vertical force), iii) a 'manufactured' out-of-plane pre-curvature (similar to the 1st bending mode) and iv) a non-zero α_0. It is shown that the flutter airspeed is not sensitive to cause of deformation; in each of these cases, the boundary is seen to decrease with tip displacement, and the general trend appears consistent. (Note that, since only the tip deflection is shown, it is possible that the full spanwise deformations were different, which could explain any discrepancies.)

Importantly, Tang & Dowell [76] commented on the significance of the ratio between the in-plane and out-of-plane stiffnesses, EI_2/EI_1. When this ratio is set to unity, the nonlinearity in the Hodges & Dowell formulation (2.14-2.16) disappears, and thus, structurally, the system is linear. This observation is used as the basis for estimating the deformation necessary for nonlinearity to be effective, i.e. the approximate tip deformations required for the nonlinear stiffness terms to have similar magnitude to the linear terms. For the 16m HALE wing, where $EI_2/EI_1 = 200$, these are estimated to be 0.7m vertical displacement and 4.6° twist. The experimental wing (Fig. 2.9, right) was then introduced by Tang & Dowell [74]. This wing has length 0.4508m and chord 0.0508m (aspect ratio = 9) and features a slender body attached to the tip, the purpose of which is to sufficiently reduce the torsional frequency so that flutter interactions are achieved at wind tunnel airspeeds. Nonlinear flutter boundaries are predicted/measured for a series of α_0, and in both the experiment and the modelling, the lowest airspeed occurs between α_0 = 1.0°-1.2°, which is where the wing is close to the undeformed (i.e. linear) condition. Thus, the effect of nonlinearity in this wing is to increase the flutter point, which is opposite to case of the HALE wing. The flutter interaction for this wing similarly comprises a torsional/in-plane mode and the 2nd out-of-plane bending mode. For this test wing, $EI_2/EI_1 = 44.05$, which is substantially lower than the HALE wing, thus the effects structural nonlinearity caused by deformation should be weaker.

More recently, a study of the HALE wing by Afonso *et al.* [86] shows that varying torsional stiffness GJ produces interesting results for flutter; for higher GJ, the flutter airspeed increases as the tip displacement increases, while for lower GJ the opposite is true, as the boundary decreases with tip displacement. This difference is attributed to a change in flutter mode. In the same paper, sweep and dihedral effect are shown to not greatly affect the boundary. An additional paper [87] compares the flutter boundaries predicted for deformed equilibria computed by both linear and nonlinear beam methods; there is a discrepancy between the two, which is observed to increase with the aspect ratio of the wing. Here, the linear equilibria results are shown to predict lower boundaries than the nonlinear equilibria.

From the above discussions, it is evident that, while the flutter airspeed of a high-aspect-ratio wing is sensitive to static deformation, the exact effect of nonlinearity (i.e. whether it compromises the boundary or not) is *highly dependant on the flutter characteristics of the particular system*, i.e. the structural modes that critically interact. Should these modes become closer as the wing statically deforms (as is the case for the HALE wing), the effect is detrimental, however this may

not always occur, depending on the stiffness properties and their sensitivity to the geometric nonlinearity. It should be noted, at this stage, that one solution could be to design a high-aspect-ratio wing such that an 'undeformed' shape is achieved in-flight during cruise condition (for example, using a manufactured downwards-curvature or decreased EI_1). While this may enable more accurate flutter prediction, there are a few practical problems with this approach, as ground clearance during taxi, take-off and landing may be not guaranteed, and stability in off-design flight conditions may be detrimentally affected.

2.4.4 Existence of limit cycle oscillations

There is substantial evidence of high-aspect-ratio wings demonstrating LCOs in the literature; in the vast majority of cases, these are obtained using numerical integration (i.e. time histories). However, similarly to Section 2.4.3, it is useful to first make some basic observations before discussing specific results. Revisiting the definition of the Hopf bifurcation (Section 2.2.2), provided the transversality and non-degeneracy conditions are met, a solution of closed orbits will always emanate from the flutter point of an aeroelastic system. Further to this, on physical grounds, a stable solution can exist at some airspeed, regardless of the Hopf criticality[10]. Thus, the existence of LCOs is dependant on i) whether the genericity conditions are met and, if they are, ii) whether the resulting amplitudes are within survivable bounds, if the system is a real-life system.

A brief point can be made about when the non-degeneracy Hopf condition fails (i.e. when $l_1 = 0$). In this case, near the equilibrium, the system is topologically equivalent to the linear system, and thus there is no smooth LCO solution. A simple example of this can be constructed by combining a linear structural model with a piecewise lift function (for example, setting the ratio $EI_2/EI_1 = 1$ in formulation (2.14 - 2.16), and using $C_L = 2\pi\alpha$ for $\alpha < \alpha_{\text{stall}}$ and $C_L = C_L^{\max}$ for $\alpha \geq \alpha_{\text{stall}}$). In the absence of any nonlinearity at the equilibrium, the local behaviour is precisely that of the linear system within the limits of the stall angle, but is bounded beyond this. The LCO solution is discontinuous in this case; an example of this can be found in Ref. [79]. Generally speaking, in any aeroelastic system, if aerodynamics are assumed ~linear at the flutter condition, which is not unreasonable, it follows that the criticality of the Hopf is determined by the effects of structural nonlinearity. Thus, should EI_2/EI_1 be close to unity, the Hopf will be near the degenerate case and LCO amplitude will grow rapidly with airspeed. This generalisation becomes less valid the closer the equilibrium condition gets to stall, which could occur if a given wing is particularly torsionally flexible. Of course, as previously discussed, Hopf criticality does not characterise all of the possible LCO solutions.

Patil *et al.* [73] presented a dedicated study to the existence of LCOs in the HALE wing. Here, the wing is disturbed from an undeformed equilibrium at various airspeeds above and below the linear flutter airspeed, which is the same airspeed as in Ref. [71]. At supercritical airspeeds,

[10] At zero airspeed, an LCO cannot exist, so the unstable solution emanating from a subcritical Hopf bifurcation will often undergo a periodic fold bifurcation (see Section 2.2.3).

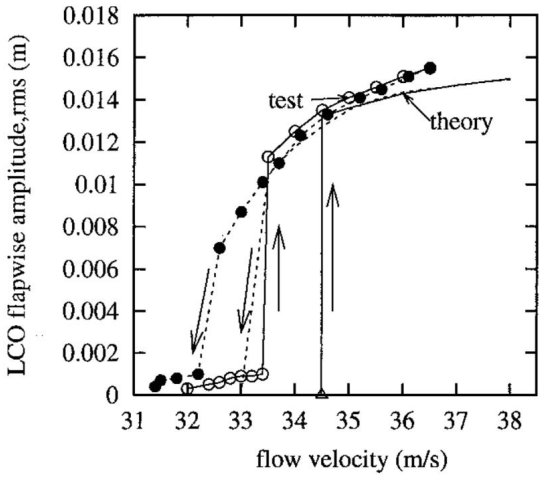

Figure 2.11: LCO hysteresis in an experimental wing (from Tang & Dowell [74]).

small disturbances are shown to grow exponentially, initially, before becoming bounded. In some cases, the time history is complex and has chaos-like characteristics. Importantly, however, larger disturbances (e.g. 2m vertical tip displacement) at subcritical airspeeds are also seen to result in stable LCOs. Moreover, the size of initial disturbance required to produce subcritical LCOs is seen to decrease as airspeed increases. In all cases, the tip twist is seen to exceed $\pm 20°$, indicating that the dynamics are, at least in part, due to aerodynamic nonlinearity. LCOs of the HALE wing are similarly reported in Ref. [76].

Significantly, the wind-tunnel test conducted by Tang & Dowell [74] also revealed subcritical LCOs. When the system is tested at an airspeed just beyond the nonlinear boundary, the wing enters into a large amplitude LCO; when the airspeed is subsequently reduced, the LCO amplitude also decreases but does not disappear at the flutter airspeed (as shown in Fig. 2.11). This hysteresis also appears in the numerical modelling of the test wing, which obtains LCO behaviour using time histories. The hysteresis is shown to disappear when the nonlinear aerodynamics are removed from the model; however, it should be noted that this appears to contradict a separate observation made of the exact same test case [80]. Regardless, the phenomenon is reported to be dependent on *"a delicate balance between stall aerodynamics and the structural nonlinear forces"*. A follow-up study by the same authors [75] describes use of the harmonic balance method to obtain the same LCO solutions.

LCOs of the test wing from Ref. [74] were subsequently the focus of a publication by Stanford & Beran [79]. In this numerical study, the structural equations (2.14-2.16) are used, and the method of multiple scales is used to derive a term, $\beta_{2\mathrm{r}}$, which quantifies the criticality of the Hopf bifurcation at flutter. Four combinations of structure/aerodynamic nonlinearity are subsequently investigated, for variations of EI_2/EI_1: i) nonlinear structure with piecewise linear C_L, ii) nonlinear structure with smooth nonlinear C_L, iii) linear structure with piecewise linear C_L and

iv) linear structure with smooth nonlinear C_L. In case *i*), the Hopf is always subcritical, apart from when $EI_2/EI_1 = 1$; the Hopf is always supercritical for case *iv*). The most insightful result is shown for case *ii*); here, the Hopf is supercritical for low EI_2/EI_1, but becomes subcritical when EI_2/EI_1 exceeds ~35. In this case, when the structural nonlinearity is weak, the smooth stalling effect of the aerodynamics dominates the criticality; however, as the structural nonlinearity increases, the subcritical influence evident in case *i*) starts to dominate. (This suggests that, for the nominal test wing where $EI_2/EI_1 = 44.05$, the Hopf bifurcation is reasonably close to the degenerate case; see Fig. 2.6.) The quantity β_{2r} is subsequently used, together with the flutter airspeed, as the objective in a series of optimisations, where derivatives for both flutter airspeed and β_{2r} are calculated for variable inertia and stiffness (spanwise) distributions. It is shown that flutter airspeed and Hopf criticality are conflicting objectives for this particular wing.

Further numerical investigation of the experimental wing was undertaken by Arena *et al.* [88]; here, a newly-developed beam formulation is coupled with the Beddoes-Leishman aerodynamic model [85], and time histories are used to demonstrate LCOs occurring beyond the flutter airspeed. The dynamic stall model is compared with unsteady and quasi-steady linear aerodynamics; quasi-steady is shown to be the least conservative of the three models. Zhang & Xiang [89] studied a configuration of the HALE wing with anisotropic composite material properties and similarly used time histories to obtain LCOs; here, a response is observed in which the wing tip does not exceed the stall angle and thus the LCO is attributed to structural nonlinearity in this case.

Studies by Kim & Strganac [90] and Strganac *et al.* [3] demonstrate LCOs for different high-aspect-ratio wings. The first of these focusses on the nonlinearity induced by an external store, however the second investigates a slender 'SensorCraft' UAV wing, using the numerical continuation software AUTO to explore the dynamics. An interesting observation is made regarding the parameter β_η, which is equivalent to the stiffness ratio EI_2/EI_1 in the Hodges & Dowell formulation above; the subcriticality of the Hopf bifurcation at the flutter point is found to be dependant on the inclusion of the β_η in the nonlinear beam formulation. When this term is removed, the Hopf is supercritical, and it is concluded that criticality is explicitly linked to a nonlinear stiffness term that couples out-of-plane bending and torsion. More generally, the observation underlines the important role that the stiffness ratio EI_2/EI_1 plays in the dynamics.

2.5 Summary

A summary of the key themes of Chapter 2 is as follows.

- *Aeroelastic flutter* is the condition where a tiny perturbation to a static aeroelastic equilibrium (i.e. a solution where aerodynamic, elastic and inertial loads are all balanced) leads to an oscillation that does not decay. The *flutter mode* is the mode of the aeroelastic system that loses stability; it comprises the interaction of flexible structural modes with the airflow.

- In a nonlinear aeroelastic system, the *flutter point* is defined by the existence of a complex-conjugate pair of eigenvalues, with zero real part, within the linearised system. If a nonlinear system does not deform with airspeed, the flutter airspeed is determined by the linear part of the system. Provided a number of genericity conditions are satisfied, a *Hopf bifurcation* occurs at the flutter point, which prescribes a smooth solution of finite amplitude limit cycle oscillations (LCOs) that exist near the equilibrium.
- The type of the Hopf bifurcation at the flutter point determines whether the LCO solutions emanate above or below the flutter airspeed.
- Evidence in the literature shows that the *geometric nonlinearity* inherent in deformed high-aspect-ratio wings can lead to significantly different flutter results compared to linear (i.e. undeformed wing) predictions. LCOs have been observed in high-aspect-ratio wings (including at undesirable, subcritical airspeeds), which have been closely linked to geometric nonlinearity.
- *Numerical continuation* techniques, which comprise path-following, predictor-corrector methods, can be used obtain the *parameter-dependant* dynamics (i.e. the equilibria and LCOs) of a nonlinear dynamical system, and do not rely on time histories. Numerical continuation techniques have been seldom used for analysing the nonlinear dynamics of high-aspect-ratio wings.

CHAPTER 3

HOPF BIFURCATION CRITICALITY

This chapter discusses how the criticality of a Hopf bifurcation, which occurs at the flutter point of a nonlinear aeroelastic system (e.g. a flexible, high-aspect-ratio wing), can be related to structural nonlinearity. An analytical method is combined with numerical continuation and a physical discussion to demonstrate how, for a 2 DoF nonlinear flutter wing model, the modal properties of the linearised aeroelastic system are linked to Hopf criticality.

3.1 Introduction

The discussions in Chapters 1 & 2 established that, given the industry trend towards flexible, high-aspect-ratio wings, nonlinear dynamical phenomena resulting from geometric nonlinearity should be better understood. Section 2.4 described how, in both numerical and experimental studies of high-aspect-ratio wings, limit cycle oscillations (LCOs) have been found to exist below the classical flutter airspeed. LCO behaviour is typically obtained using numerical integration, i.e. via the generation of time histories; such an approach is cumbersome in practice, as many simulations may be necessary for all possible behaviours to be detected.

As discussed in Section 2.1.2, provided some genericity conditions are satisfied, the flutter point of a nonlinear aeroelastic system (that describes e.g. a flexible, high-aspect-ratio wing with geometric nonlinearity) coincides with a Hopf bifurcation. From this bifurcation point, a smooth solution of LCOs emanates, for either increasing or decreasing airspeeds. The former case is called a *supercritical* Hopf bifurcation, whereas the latter is called a *subcritical* Hopf bifurcation. In the supercritical case, the LCOs are stable to small perturbations, whereas in the subcritical case, they are unstable. While these two bifurcations respectively have clear desirable and undesirable characteristics, particularly when compared to the linear outcome, the underlying physical mechanisms that differentiate them have not been well researched. In

previous studies, the criticality of a Hopf bifurcation in a nonlinear flutter context is usually obtained via purely analytical or numerical means, without focus on the physical characteristics (for example, see Refs. [79, 55]).

The aim of this chapter is to combine theoretical and physical approaches to obtain a better insight into the drivers of Hopf criticality in flexible, high-aspect-ratio wings. This will be achieved by investigating a simple, 2 degree-of-freedom (DoF) binary flutter wing model, with cubic structural nonlinearity, using numerical continuation (see Section 2.3). As with all other work in this thesis, no stall effects are modelled; the aerodynamics close to the equilibrium are thus assumed linear, so the criticality of the Hopf bifurcation is solely prescribed by nonlinearity in the structure.

3.2 Analytical discussion

In generic nonlinear dynamical systems, the criticality of a Hopf bifurcation is directly related to the behaviour very close to the equilibrium. This section provides an overview of this concept, specifically applied to an aeroelastic flutter context, and applies an established analytical criterion to a 2 DoF flexible wing model with parameterised nonlinearity. The results from this example are then compared to one-parameter continuation of LCO solutions of the system, and forms the basis for a physical discussion of the phenomena in Section 3.3.

Consider the general, parameterised nonlinear dynamical system

$$\dot{x} = f(x, v), \tag{3.1}$$

where $x \in \mathbb{R}^n$ and $v \in \mathbb{R}$ is a smooth parameter (e.g. airspeed). Recall, from Chapter 2, that linearisation about a static equilibrium x^* is only valid if said equilibrium is *hyperbolic*, i.e. $\mathrm{Re}\,(\lambda_{1..n}) \neq 0$. Should there exist any critical eigenvalues with zero real part, λ_c, the dynamics predicted by linearisation are not topologically equivalent to those of the nonlinear system and, if all non-critical λ are stabilising, the overall stability of x^* is determined by the nonlinear dynamics of (3.1) restricted to the invariant local *centre manifold*, W^c. At the precise equilibrium, W^c is tangential to the linear manifold E^c, which is prescribed by the critical eigenvector v_c (i.e. the *flutter mode*) of the linearised system (this linear manifold was illustrated in Fig. 2.3).

At the flutter point in a nonlinear aeroelastic system, the critical eigenvalues comprise a complex-conjugate pair (i.e. $\lambda_c = \pm \mathrm{i}\omega_0$), and thus W^c is 2D. Figure 3.1 illustrates the two generic scenarios that can exist at this critical condition, which correspond to supercritical and subcritical Hopf bifurcations respectively. As per the definition of flutter (see Section 2.1.2), all non-critical eigenvalues are stabilising and so all trajectories $x(t)$ near x^* tend to W^c; in the supercritical case (a), a decaying oscillation exists, which very slowly converges to the equilibrium, whereas in the subcritical case (b), a slowly divergent oscillation exists. Therefore, the equilibrium is stable in (a) and unstable in (b).

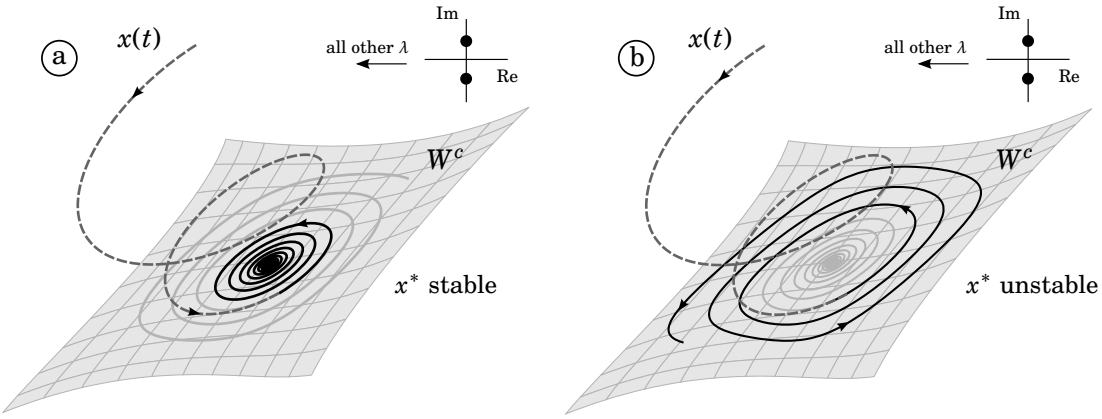

Figure 3.1: Generic illustrations of the 2D centre manifold, at the flutter point, for a (a) supercritical and (b) subcritical Hopf bifurcation. All non-critical eigenvalues are stabilising.

As shown by Kuznetsov [7], the dynamics of the parameterised system (3.1), undergoing a generic Hopf bifurcation, when restricted to the critical centre manifold, are topologically equivalent to the complex normal form

$$\dot{w} = (\mu + \mathrm{i}\omega)\, w + l_1 w |w|^2, \tag{3.2}$$

where $w \in \mathbb{C}$ is a complex variable and $\mu \in \mathbb{R}$ is a smooth parameter. The scalar coefficient of the cubic terms, l_1, is called the *first Lyapunov coefficient* and determines the criticality of the bifurcation; for $l_1 < 0$, the nonlinearity is stabilising, whereas for $l_1 > 0$ it is destabilising. Note that this expression is also topologically equivalent to the Hopf normal form shown in Section 2.2.2.

Adopting the notation where $\langle \circ, \bullet \rangle$ corresponds to the complex dot product $\bar{\circ}^{\mathsf{T}} \bullet$, a generalised, analytical expression for l_1 can be written as

$$l_1 = \frac{1}{2\omega_0} \operatorname{Re}\Big\langle p,\, C(q,q,\bar{q}) - 2B\big(q,\, A^{-1} B(q,\, \bar{q})\big) + B\big(\bar{q},\, (2\mathrm{i}\omega_0 I - A)^{-1} B(q,q)\big)\Big\rangle, \tag{3.3}$$

see [7], where p and q are complex eigenvectors defined by

$$Aq = \mathrm{i}\omega_0 q, \quad A^{\mathsf{T}} p = -\mathrm{i}\omega_0 p, \quad \langle p,\, q \rangle = 1, \tag{3.4}$$

and where B and C are bilinear/trilinear functions of the second and third Jacobian tensors (J_2 & J_3, evaluated at u^*) and are given by

$$B_i(p,q) = \sum_{j,k=1}^{n} \frac{\partial^3 f_i(x,v)}{\partial x_j \partial x_k} p_j q_k, \qquad C_i(p,q,r) = \sum_{j,k,l=1}^{n} \frac{\partial^3 f_i(x,v)}{\partial x_j \partial x_k \partial x_l} p_j q_k r_l. \tag{3.5}$$

where f_i corresponds to the ith row of (3.1). See also Govaerts *et al.* [32]. When $l_1 < 0$, the Hopf is supercritical, whereas when $l_1 > 0$, the Hopf is subcritical. For instances where $l_1 = 0$, the result

is referred to as a *degenerate* or *generalised* Hopf or a Bautin point, and the local behaviour of the system may be dependant on nonlinearities of 5^{th} order and above [32]. As demonstrated in Chapter 4, a 1D locus of Hopf points can be obtained in a given system if two parameters are free to vary (in this example, these were airspeed and stiffness); should a degenerate Hopf ($l_1 = 0$) exist within this set of bifurcation points, this indicates that a change of flutter criticality occurs. The location of this degenerate bifurcation is not only interesting from a design standpoint, but also from a fundamental perspective that seeks to understand the underlying phenomena determining criticality.

The use of formula (3.3) has several benefits over alternative analytical approaches; for example, it can be directly implemented without performing any coordinate transforms on (3.1). Methods that seek to approximate the surface W^c require a change of basis into Jordan form; see [7]. In general, however, the rapid evaluation of l_1 is only feasible for very low-order systems; obtaining J_2 and J_3 for complex systems is typically not straightforward, and the overall calculation may be cumbersome if it is dependant on numerical approximations (e.g. finite-difference derivatives). Thus, more practical methods for predicting Hopf criticality in real-life engineering systems are highly desirable, particularly in the early stages of design where the investigation of vast areas of parameter space is useful. For particular systems, however, use of (3.3) is achievable, as is demonstrated in Section 3.2.1.

3.2.1 2 DoF binary flutter wing (with trivial equilibria)

The analytical criterion described in Section 3.2 is now applied to a simple, 2 degree-of-freedom (DoF) nonlinear model of a flexible wing. This system is based on the two-mode approximation binary flutter wing model used in Wright & Cooper [14] (Chapter 10 of the textbook), which uses a single shape function for each of the out-of-plane bending and torsional deformations. Originally used to demonstrate linear binary flutter, the model is extended in the present study to include nonlinearity in the structural part of the formulation. The nominal wing parameters used here are identical to those in the original text. The 2 DoF flutter binary flutter wing model, including structural nonlinearity, can be expressed as

$$\begin{bmatrix} \ddot{u}_b \\ \ddot{u}_t \end{bmatrix} = -\boldsymbol{A}^{-1}\left(\rho v \boldsymbol{B} + \boldsymbol{D}\right)\begin{bmatrix} \dot{u}_b \\ \dot{u}_t \end{bmatrix} - \boldsymbol{A}^{-1}\left(\rho v^2 \boldsymbol{C} + \boldsymbol{E}\right)\begin{bmatrix} u_b \\ u_t \end{bmatrix} + \begin{bmatrix} \gamma_b u_b^3 \\ \gamma_t u_t^3 \end{bmatrix}, \tag{3.6}$$

where v is airspeed, and

$$\boldsymbol{A} = m\begin{bmatrix} \dfrac{sc}{5} & \dfrac{s}{4}\left(\dfrac{c^2}{2} - cx_f\right) \\ \dfrac{s}{4}\left(\dfrac{c^2}{2} - cx_f\right) & \dfrac{s}{3}\left(\dfrac{c^3}{3} - c^2 x_f + x_f c^2\right) \end{bmatrix}, \qquad \boldsymbol{B} = \begin{bmatrix} \dfrac{cs}{10}a_w & 0 \\ -\dfrac{c^2 s}{8}e a_w & -\dfrac{c^3 s}{24}M_{\dot{\theta}} \end{bmatrix},$$

$$\boldsymbol{C} = \begin{bmatrix} 0 & \frac{cs}{8}a_w \\ 0 & -\frac{c^2 s}{6}ea_w \end{bmatrix}, \qquad \boldsymbol{D} = \begin{bmatrix} d & 0 \\ 0 & d \end{bmatrix}, \qquad \boldsymbol{E} = \begin{bmatrix} \frac{4EI}{s^3} & 0 \\ 0 & -\frac{GJ}{s} \end{bmatrix}.$$

The various symbols shown above are defined in Table 3.1, along with their nominal values. Note that the bending and torsional DoFs are described by a quadratic and a linear assumed shape, respectively (see illustration in Fig. 3.2).

Table 3.1: Nominal 2 DoF binary flutter wing parameters.

Parameters from Ref. [14]	
Wing	
Semi-span (s)	7.5 m
Chord (c)	2 m
Elastic axis (x_f)	$0.48c$
Mass axis (x_f)	$0.5c$
Mass per unit area (m)	200 kg/m^2
Out-of-plane stiffness (EI)	2×10^7 N m^2
Torsional stiffness (GJ)	2×10^6 N m^2
Lift curve slope (a_w)	2π
Pitch damping derivative ($M_{\dot{\theta}}$)	-1.2
Air density (ρ)	1.225 kg/m^3
Additional parameters	
Structural damping factor (d)	0
Bending nonlinearity coefficient (γ_b)	0
Torsion nonlinearity coefficient (γ_t)	0

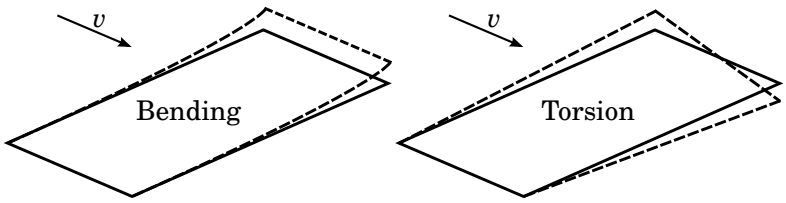

Figure 3.2: 2 DoF binary flutter wing model.

The second order system (3.6) can be expressed as

$$\begin{pmatrix} \dot{u}_b \\ u_t \\ \dot{u}_b \\ \dot{u}_t \end{pmatrix} = \begin{pmatrix} \dot{u}_b \\ \dot{u}_t \\ -\boldsymbol{A}^{-1}\left(\rho v \boldsymbol{B} + \boldsymbol{D}\right)\begin{bmatrix} \dot{u}_b \\ \dot{u}_t \end{bmatrix} - \boldsymbol{A}^{-1}\left(v^2\boldsymbol{C} + \boldsymbol{E}\right)\begin{bmatrix} u_b \\ u_t \end{bmatrix} \end{pmatrix} + \begin{pmatrix} 0 \\ 0 \\ \gamma_b u_b^3 \\ \gamma_t u_t^3 \end{pmatrix}, \tag{3.7}$$

which, after defining $x \in \mathbb{R}^4 = \begin{pmatrix} u_b & u_t & \dot{u}_b & \dot{u}_t \end{pmatrix}^\mathsf{T}$ and parameterising in terms of airspeed, may be written in the general first order form

$$\dot{x} = f(x, v) = A(v)\,x + G(x^3). \tag{3.8}$$

The nonlinear part can be written as

$$G(x^3, \gamma_b, \gamma_t) = \begin{pmatrix} 0 & 0 & \gamma_b\, u_b^3 & \gamma_t\, u_t^3 \end{pmatrix}^\mathsf{T}, \tag{3.9}$$

noting that the parameters $\gamma_b, \gamma_t \in \mathbb{R}$ are the coefficients of the nonlinear terms. These terms comprise uncoupled *cubic stiffness* terms, which may be described as *hardening* ($\gamma_{b,t} < 0$) or *softening* ($\gamma_{b,t} > 0$). As will be shown, there is a direct relationship between these stiffness terms and the criticality of the Hopf bifurcation occurring at the flutter point of the system.

The 2 DoF nonlinear system described by (3.8) is homogeneous, and thus has a trivial (i.e. undeformed) equilibrium, $x^* = 0$, at all airspeeds. Therefore, the location of the flutter point is entirely prescribed by the linear part of the system, $A(v)$, and all Hopf points occur at $x^* = 0$. Given this, and exploiting the fact that the nonlinearity in the system is *cubic only*, the general expression for l_1 (3.3) can be reduced to

$$l_1 = \frac{1}{2\omega_0} \operatorname{Re}\left\langle p, C(q, q, \bar{q}) \right\rangle, \tag{3.10}$$

as all elements of J_2 are equal to zero, which from (3.5), leads to $B = 0$. Furthermore, only two elements of J_3 are nonzero, i.e.

$$\frac{\partial^3 f_3(x,v)}{\partial x_1 \partial x_1 \partial x_1} = 6 \quad \text{and} \quad \frac{\partial^3 f_4(x,v)}{\partial x_2 \partial x_2 \partial x_2} = 6. \tag{3.11}$$

With symbolic manipulation, this allows (3.10) to be reduced to

$$l_1 = \frac{1}{2\omega_0} \operatorname{Re}\left[\gamma_b\, \bar{p}_3\, q_1^2\, \bar{q}_1 + \gamma_t\, \bar{p}_4\, q_2^2\, \bar{q}_2\right], \tag{3.12}$$

which may be expressed in the form

$$l_1 = \frac{1}{2\omega_0} \left(l_b\, \gamma_b + l_t\, \gamma_t\right), \tag{3.13}$$

where

$$\begin{aligned} l_b &= 6\left(q_{1_{\mathrm{Re}}}^3\, p_{3_{\mathrm{Re}}} + q_{1_{\mathrm{Im}}}^3\, p_{3_{\mathrm{Im}}} + q_{1_{\mathrm{Re}}}\, q_{1_{\mathrm{Im}}}^2\, p_{3_{\mathrm{Re}}} + q_{1_{\mathrm{Re}}}^2\, q_{1_{\mathrm{Im}}}\, p_{3_{\mathrm{Im}}}\right), \\ l_t &= 6\left(q_{2_{\mathrm{Re}}}^3\, p_{4_{\mathrm{Re}}} + q_{2_{\mathrm{Im}}}^3\, p_{4_{\mathrm{Im}}} + q_{2_{\mathrm{Re}}}\, q_{2_{\mathrm{Im}}}^2\, p_{4_{\mathrm{Re}}} + q_{2_{\mathrm{Re}}}^2\, q_{2_{\mathrm{Im}}}\, p_{4_{\mathrm{Im}}}\right), \end{aligned} \tag{3.14}$$

where $\circ_{i_{\mathrm{Re}}} = \operatorname{Re}(\circ_i)$ and $\circ_{i_{\mathrm{Im}}} = \operatorname{Im}(\circ_i)$. Given this, the implicit linear curve

$$l_b\, \gamma_b + l_t\, \gamma_t = 0 \tag{3.15}$$

therefore describes the set of generalised Hopf points (i.e. where $l_1 = 0$) for variations in γ_b and γ_t, and thus defines the regions where the bifurcation is supercritical ($l_1 < 0$) and subcritical ($l_1 > 0$).

For the nominal wing parameters (Table 3.1) the flutter airspeed v_f is found to be 82.22 m/s, where (3.4) gives p = [-1.3433 – 1.1262i, 0.6837 + 13.8674i, 0.0358 – 0.0988i, -0.5664 + 0.0491i]$^\mathsf{T}$ and q = [-0.0024 + 0.0173i, 0.0000 + 0.0370i, -0.4221 – 0.0584i, -0.9038 + 0.0000i]$^\mathsf{T}$. Using (3.14), the quantities l_b and l_t at this condition are thus computed as -3.285e-6 and 1.499e-5 respectively. From the different signs of these values, and using (3.15), it is evident that the nonlinearity prescribed by γ_b and γ_t have *opposing* effects on Hopf criticality; for the case where $\gamma_b < 0$ and $\gamma_t = 0$ (bending is *hardening*), $l_1 > 0$ (subcritical), whereas for $\gamma_b > 0$ and $\gamma_t = 0$ (bending is *softening*), $l_1 < 0$ (supercritical). These relationships are reversed when $\gamma_b = 0$ and $\gamma_t \neq 0$. Clearly, l_1 vanishes when $\gamma_b, \gamma_t = 0$, as the system is purely linear.

Figure 3.3 shows the one-parameter numerical continuation of LCO solutions for a number of mixed nonlinear cases, where both $\gamma_b, \gamma_t \neq 0$ and so both cubic terms in (3.9) are active; in each case, the max. & min. of the LCO solutions in u_b are shown. From the direction and stability of the solutions, cases (a) and (b) reveal subcritical and supercritical Hopf bifurcations respectively, as expected. Cases (c) and (d) are specifically placed close to the implicit curve (3.15); the solutions for these cases show that the bifurcations are closer to the degenerate case[1], as expected.

From equation (3.14), it is clear that when γ_b and γ_t are fixed, l_1 is only dependant on p and q, i.e. the normalised critical and adjoint eigenvectors of $A(v)$. Thus, the linear flutter mode v_c (i.e. the aeroelastic mode that loses stability) directly prescribes how the nonlinear terms γ_b, γ_t affect the criticality of the Hopf point of (3.8).

3.2.2 2 DoF binary flutter wing (with nontrivial equilibria)

Briefly, consider a case where an additional general term, independent of x but dependant on v, extends the nonlinear system (3.8) to

$$\dot{x} = A(v)\,x + G(x^3) + H(v, \alpha_0), \tag{3.16}$$

where $\alpha_0 \in \mathbb{R}$ corresponds, for example, to the root angle of attack of the wing. The system is no longer homogenous, and thus provided both v and $\alpha_0 \neq 0$, now has nontrivial equilibria (i.e. the wing now statically deforms with airspeed). Therefore, the nonlinear terms are now exercised within the equilibria solutions, and thus x^* and v_f both vary with $\{\gamma_b, \gamma_t\}$. Due to this, $B \neq 0$ in (3.3), and the complete expression must be used for the calculation of l_1. However, as will become evident in the next section, a change in criticality due to nontrivial equilibria is only expected if the deformation is sufficiently large to cause a significant change in the structural properties of the wing.

[1] A degenerate Hopf would be indicated by a vertical LCO solution.

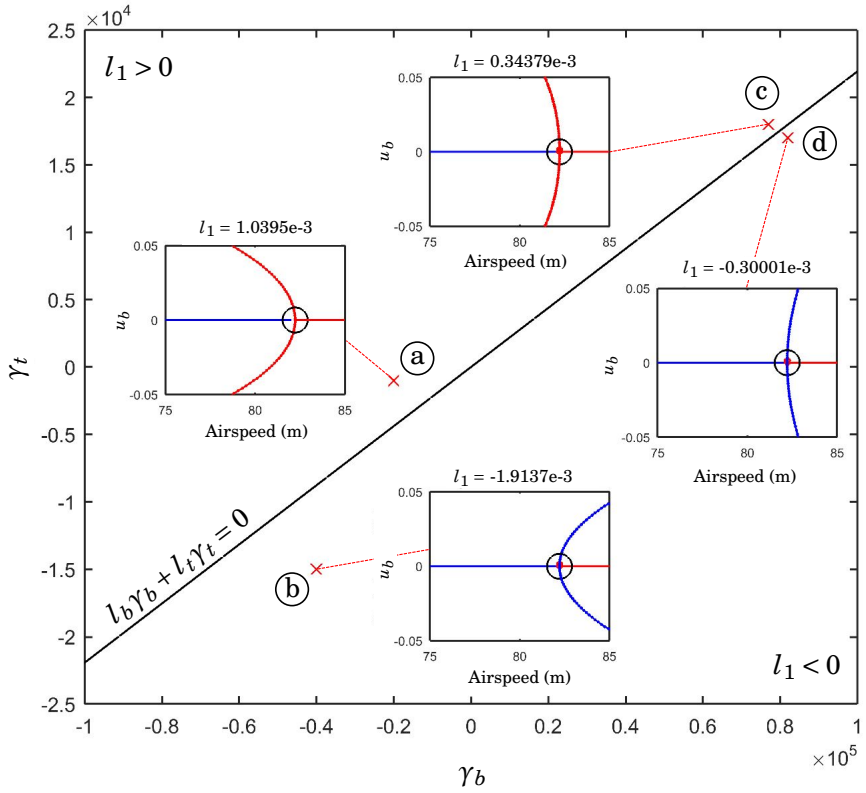

Figure 3.3: One-parameter continuation of LCOs, for varying airspeed, for 2 DoF wing when $\{\gamma_b, \gamma_t\}$ = (a) $\{-0.2e5, -0.1e4\}$, (b) $\{-0.4e5, -1.5e4\}$, (c) $\{0.82e4, -1.7e4\}$ and (d) $\{0.77e4, 1.8e4\}$ (varying cubic coefficients). In all cases, l_b = −3.285e-6 and l_t = 1.499e-5.

3.3 Physical discussion

The opposing effects of γ_b and γ_t on Hopf criticality, shown in Fig. 3.3, can be interpreted using some physical insight of the aeroelastic system. Recall, from Section 2.2.1, that finite amplitude, self-sustained oscillations (i.e. LCOs) are the result of critical modal interactions *intermittently* occurring during the time-varying deformation of a wing [30]. Near the equilibrium, at the flutter condition, provided the local aerodynamics are linear (which is the case for 2 DoF binary flutter wing, but also applies generally if a wing is not stalled), any change to the critical interaction is caused by nonlinearity in the structure.

Consider the case where the flutter point of (3.8) is supercritical. In this instance, the amplitude of the resulting stable LCO solution grows smoothly for $v > v_f$ (e.g. see Fig. 3.3, cases b & d). At the critical airspeed ($v = v_f$), the LCO amplitude is precisely zero and, as illustrated in Fig. 3.1 (a), the equilibrium x^* is *nonlinearly stable* on the centre manifold W^c. Now, for this to occur physically, the critical flutter interaction that, by definition, exists at x^*, *must necessarily*

decrease when the system is perturbed on W^c. In subcritical cases, where x^* is *nonlinearly unstable* at $v = v_f$ (Fig. 3.1, b) the opposite is true, i.e. the interaction *must necessarily* ***increase*** when the system is perturbed on W^c. If the structural nonlinearity has no effect, the flutter interaction is unchanged, and the amplitude of oscillation is constant, as is expected in the linear or degenerate Hopf case.

The bending and torsional DoFs in system (3.8) are coupled by both inertial and aerodynamic terms; this is evident from the full aeroelastic formulation shown in (3.6), which contains off-diagonal terms in matrix $\boldsymbol{A}$. At any given airspeed, the *system* modes of (3.8), which are defined by the eigenbasis v_1, $v_2 \in \mathbb{C}^n$ (i.e. the eigenvectors of A), comprise components of both bending and torsion; let these *constituent* deformations be referred to as the structural 'modes' that are present within the system modes. Define ω_b, $\omega_t \in \mathbb{R}$ as the natural frequencies of the bending and torsional components of the flutter mode v_c, respectively; therefore, at the equilibrium at the flutter point, the frequency difference

$$\delta\omega_c = |r_1\omega_b - r_2\omega_t| \tag{3.17}$$

must be sufficiently 'small' such that a critical flutter interaction, with ratio r_1/r_2, exists between the two structural modes and the airflow. The nonlinear stability of the equilibrium, and thus the criticality of the flutter point, is determined by how this difference varies as the wing deforms on W^c; should it increase, the structural modes become *less* effectively coupled, and the equilibrium is stable (*supercritical* Hopf), whereas if it decreases, the modes become *more* efficiently coupled, and the equilibrium is unstable (*subcritical* Hopf). If the difference is unchanged, the result is a degenerate Hopf. Clearly, the variation of $\delta\omega_c$ is determined by the relative effect of the nonlinearity (which is prescribed by γ_b and γ_t) on the frequencies ω_b and ω_t when the system is perturbed. This variation is obviously dependant on the softening/hardening effect of γ_b and γ_t, but also (importantly) on the relative ordering of ω_b and ω_t, as will soon be discussed.

While the variation of (3.17) cannot be obtained explicitly, an implicit indication can be found using the two *system* modes of (3.8) at the flutter point. Figure 3.4 shows the variation of the system modes of (3.8), for increasing airspeed, where the flutter airspeed is indicated by the vertical dashed line at 82.22 m/s. The colouring of the modes in Fig. 3.4 is derived from the mode shapes (i.e. the eigenvectors v_1, v_2 converted to $\mathbb{R}^n$), where red = bending and green = torsion. Since (3.8) is homogeneous, the variations shown in Fig. 3.4 are entirely prescribed by the linear part of the system, and are not affected by γ_b or γ_t. Figure 3.4 (left) shows that, at the flutter point, the modes are bending-dominated and torsion-dominated, respectively, and have frequencies of 2.89 Hz and 3.88 Hz (the latter being the flutter mode); thus, $\omega_t > \omega_b$ in this instance.

First, consider the two generic nonlinear scenarios where only a single cubic term is nonzero, i.e. the cases where $\{\gamma_b \neq 0, \gamma_t = 0\}$ or $\{\gamma_b = 0, \gamma_t \neq 0\}$. For the latter case $\{\gamma_b = 0, \gamma_t \neq 0\}$ (nonlinear *torsion*), the active cubic term u_t^3 clearly has a greater effect on ω_t relative to ω_b. Now, since $\omega_t > \omega_b$ at this flutter condition, the frequency difference $\delta\omega_c$ therefore increases as ω_t increases,

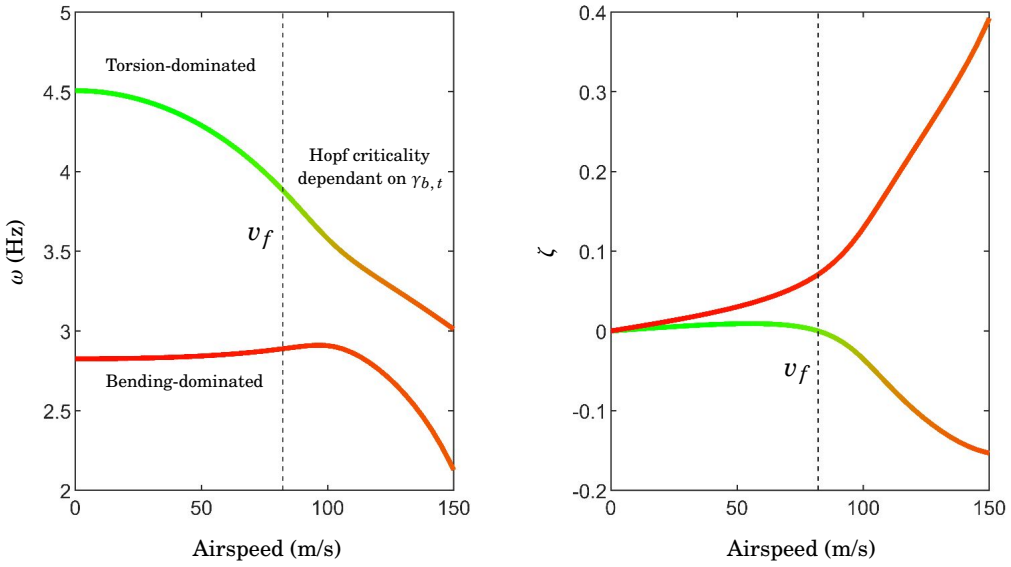

Figure 3.4: Variation of system modes, for varying airspeed, for 2 DoF wing (coloured according to mode shape, where red = bending, green = torsion). Vertical dashed line indicates flutter airspeed.

and decreases as ω_t decreases. Thus, if $\gamma_t < 0$ (hardening), $\delta\omega_c$ increases, whereas if $\gamma_t > 0$ (softening), $\delta\omega_c$ decreases; these correspond to supercritical and subcritical Hopf bifurcations, respectively. For the other scenario, where $\{\gamma_b \neq 0, \gamma_t = 0\}$ (nonlinear *bending*), the opposite relationships are now true; the active u_b^3 term more greatly affects ω_b (the lower frequency), and thus $\delta\omega_c$ decreases when ω_b increases, and vice versa.

The basic relationships described above are in agreement with the numerical calculations of l_b and l_t in Section 3.2.1, which showed that hardening-bending or softening-torsion led to a subcritical Hopf, and softening-bending or hardening-torsion led to a supercritical Hopf. For the more general case, where both cubic terms u_b^3, u_t^3 are active, i.e. $\{\gamma_b \neq 0, \gamma_t \neq 0\}$, the criticality is more dependant on the composition of the flutter mode. Given that v_c is torsion-dominated in this case (Fig. 3.4, right), and recalling that the centre manifold W^c is tangential to the linear manifold of v_c, the criticality has a greater sensitivity to u_t^3 than to u_b^3, so γ_t is more dominant than γ_b. This is evident from Fig. 3.3, and because $l_t > l_b$, which from (3.13) means that l_t has greater influence on the the Lyapunov coefficient, l_1.

The general applicability of using the system modes for an indication of Hopf criticality can be demonstrated using a simple time history at a non-critical airspeed (i.e. where $v \neq v_f$). Figure 3.5 shows an example response for the case {-1e5, 1e5} for v = 90 m/s; note that the Hopf is subcritical in this case (Fig. 3.3). Here, u_t is compared with the time-varying $\delta\omega$, which is defined as the frequency difference between the system modes, $|\omega_1 - \omega_2|$. In the initial part of the response (a), the phasing is such that the maxima of $\delta\omega$ coincide with $u_t = 0$, and the minima

of $\delta\omega$ coincide with the maxima/minima of u_t. Thus, the interaction is increasing as the wing deforms, further destabilising the motion, which is as expected for a subcritical case. In part (b), the relative phasing is seen to change (due to a change in sign of $\omega_1 - \omega_2$), and thus in part (c) the system is settled into an LCO, where now the minima of $\delta\omega$ (approximately) coincide with the maxima/minima of u_t and the maxima of $\delta\omega$ coincide with $u_\mathrm{t} = 0$. Thus, the interaction of the structural modes is now reducing as the wing deforms.

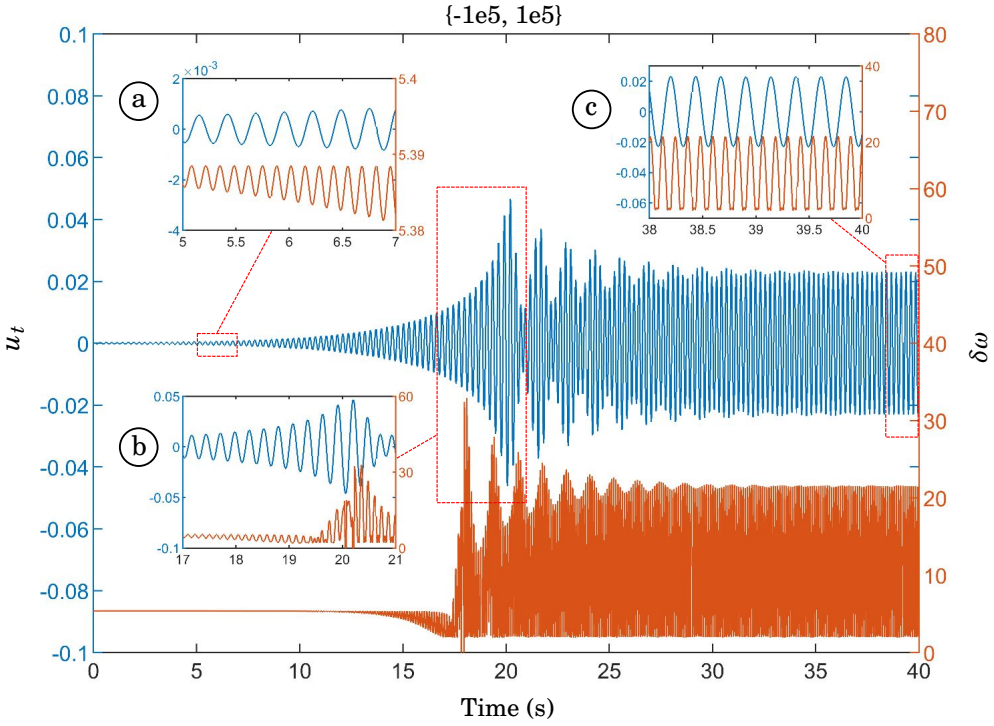

Figure 3.5: Time history for $\{\gamma_b, \gamma_t\}$ = {-1e5, 1e5} (subcritical Hopf), v = 90 m/s, comparing u_t and $\delta\omega$.

Given the discussions above, a pertinent question is to ask how the Hopf criticality of the 2 DoF wing (3.8) can be *changed*, for fixed γ_b and γ_t, when a physical parameter of the wing is varied. From (3.17), it is clear that any parameter that affects the relative ordering of the structural mode frequencies, at the flutter condition, will cause such a change; this could result from two general possibilities: i) the mode frequencies themselves vary, or ii) the solutions maintain similar frequencies, but 'exchange' bending/torsional composition. In both cases, the mode frequencies become effectively reordered; therefore, the structural nonlinearity will prescribe a different Hopf criticality compared to the nominal case. Revisiting Fig. 3.4, it is clear that in the nominal system (3.8), the modes do not cross over as airspeed increases, but do undergo a significant change in composition; at ~125 m/s, for example, the torsion-dominated mode is clearly now dominated by bending, and the bending-dominated mode has gained a larger torsion component. Thus, should

the flutter point occur at this higher airspeed, and γ_b & γ_t are fixed, the new Hopf bifurcation may have different criticality to the Hopf that occurs at 82.22 m/s. In Section 3.3.1, it will be shown that this is indeed the case.

The convergence of mode frequencies as airspeed increases, shown for the 2 DoF wing (Fig. 3.4, left), is typical of an aeroelastic system that undergoes flutter, particularly if the critical structural mode interaction comprises a 1:1 ratio. A 1:1 interaction requires the modes to be sufficiently close in frequency; thus, given that wind-off modes are often purposely separated by design, the convergence of two modes, with airspeed, is necessary for the interaction to occur. Figure 3.6 shows an illustration of two generalised convergence trends that may exist, which could both result in a different bifurcation criticality, should the Hopf occur *before* or *after* the convergence. In case (a), the modes do not cross, but the *compositions* of the modes sufficiently change, and in case (b), the modes do not change composition, but instead they *cross over* and change order. Assuming the same solution loses stability in both cases, the Hopf bifurcation occurring at $\hat{v}_f$ will generally have different criticality to that occurring at v_f; examples of this will be shown throughout the rest of this chapter. If the nonlinear system in question is statically deforming with airspeed (i.e. the case of non-trivial equilibria), additional indicators of Hopf criticality can be found in frequency plots; this will be revisited in Section 4.7.

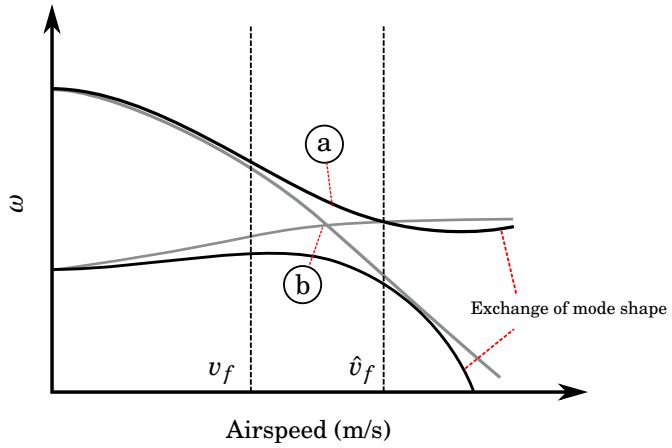

Figure 3.6: Generic illustration of the mode convergence that could cause change in Hopf criticality; solid line (a) shows two modes exchanging mode compositions without crossing, grey line (b) shows two modes crossing whilst maintaining original mode compositions.

3.3.1 Variation of structural damping

To demonstrate how the Hopf criticality in the nominal 2 DoF wing can be changed, for fixed nonlinearity, (3.8) is parameterised to include a *nonzero structural damping* term. The purpose of this parameter is to enable the flutter point of (3.8) to be moved to a higher airspeed, without

greatly affecting the overall frequencies and compositions shown in Fig. 3.4; thus, it allows the boundary to be placed beyond the mode convergence, to where a change in Hopf criticality is expected per the illustration in Fig. 3.6. Re-parameterising (3.8) to include a structural damping term, it may be rewritten as

$$\dot{x} = A(v,\, d)\, x + G(x^3), \tag{3.18}$$

where $d \in \mathbb{R}$; see (3.6). Note that the nonlinear part of the system is unchanged. Figure 3.7 shows the variation of mode frequencies and damping for (3.18), for increasing airspeed, for d = 2.5e3. Compared to the modes of the original system (Fig. 3.4), where $d = 0$, the overall frequencies and mode compositions are negligibly affected; however, the presence of structural damping has increased the flutter airspeed to 145.21 m/s, where the flutter mode now has a significant bending component (see Fig. 3.7, right). Thus, varying d suitably changes the airspeed of v_f, without significantly affecting the modes of the linearised system.

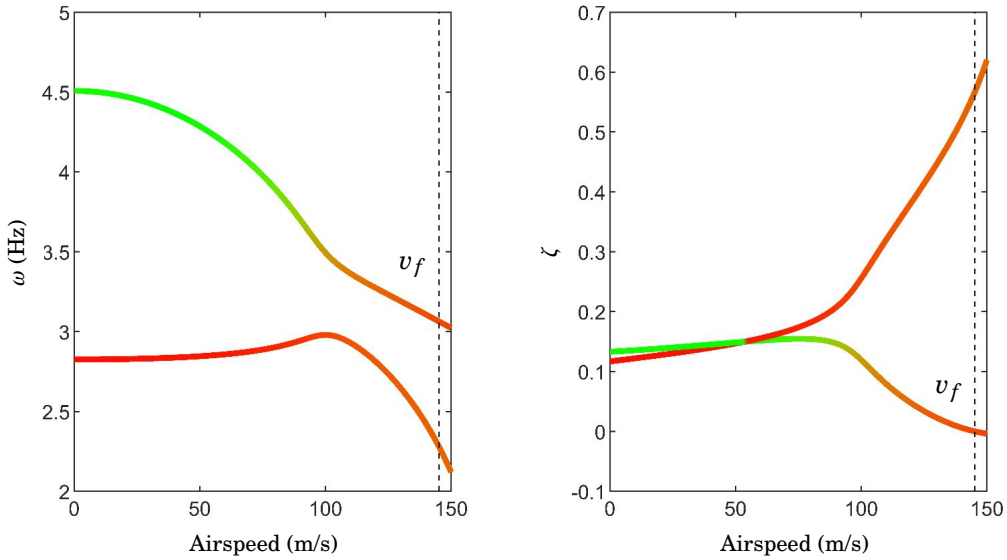

Figure 3.7: Variation of system modes, for varying airspeed, for 2 DoF wing when d = 2.5e3 (increased from nominal).

Figure 3.8 shows the one-parameter continuation of LCO solutions, for the nonlinear case $\{\gamma_b, \gamma_t\}$ = {0, 1e3} (softening-torsion), for d = 0, 1e3, 2e3 and 2.5e3. Inspecting these solutions, it is clear that, for this case, the subcritical Hopf bifurcation (which was the nominal outcome for softening-torsion nonlinearity) becomes supercritical as damping increases, and the degenerate case occurs at a value between d = 2e3 and 2.5e3 (in the airspeed region 127.3 - 145.2 m/s). Since the nonlinearity is unchanged, this change of Hopf criticality is due to the varying modes alone.

Figure 3.9 shows the two-parameter continuation of Hopf bifurcations, for varying d and airspeed, for the separate cases $\{\gamma_b, \gamma_t\}$ = (a) {-1e3, 0} (hardening-bending), (b) {1e5, 0} (softening-

bending), (c) {0, -1e5} (hardening-torsion), and (d) {0, 1e3} (softening-bending). The locus of bifurcations is identical in all instances, since $x^* = 0$, and show that the flutter airspeed monotonically increases with d, as expected from Fig. 3.8. In each example, the secondary vertical axis shows the variation of the Lyapunov coefficient l_1, which is obtained using a numerical implementation of expression (3.12) at each continuation step. In every case, the sign of l_1 changes as d increases, indicating that the Hopf criticality changes, for every type of nonlinearity. For the nonlinear bending cases {-1e3, 0} and {1e5, 0}, the change occurs at d = 1942.38 (125.6 m/s), whereas for the torsion cases {0, -1e5} and {0, 1e3}, it occurs at d = 2381.91 (139.4 m/s). This discrepancy is expected, given that the critical eigenvector v_c gains an increasing bending component as d increases (the variation of $\delta\omega_c$ on W^c is thus more sensitive to changes in γ_b).

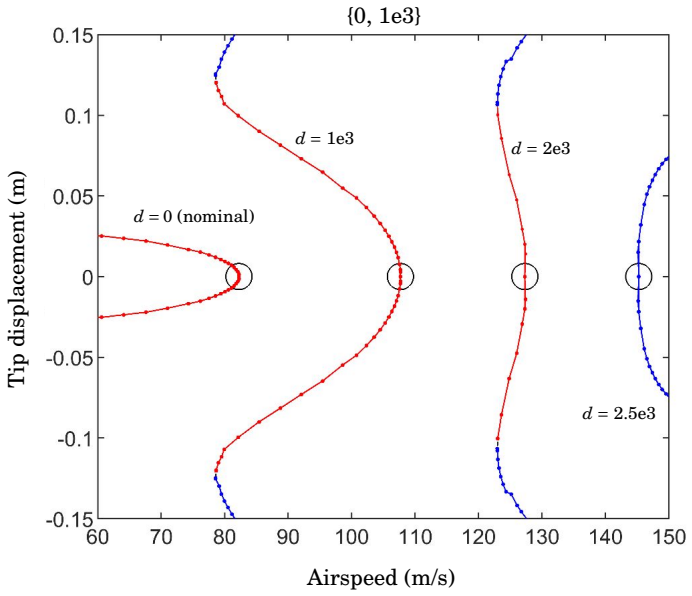

Figure 3.8: One-parameter continuation of LCOs, for varying airspeed, for 2 DoF when d = 0, 1e3, 2e3 and 2.5e3, where $\{\gamma_b, \gamma_t\}$ = {0, 1e3} (softening-torsion).

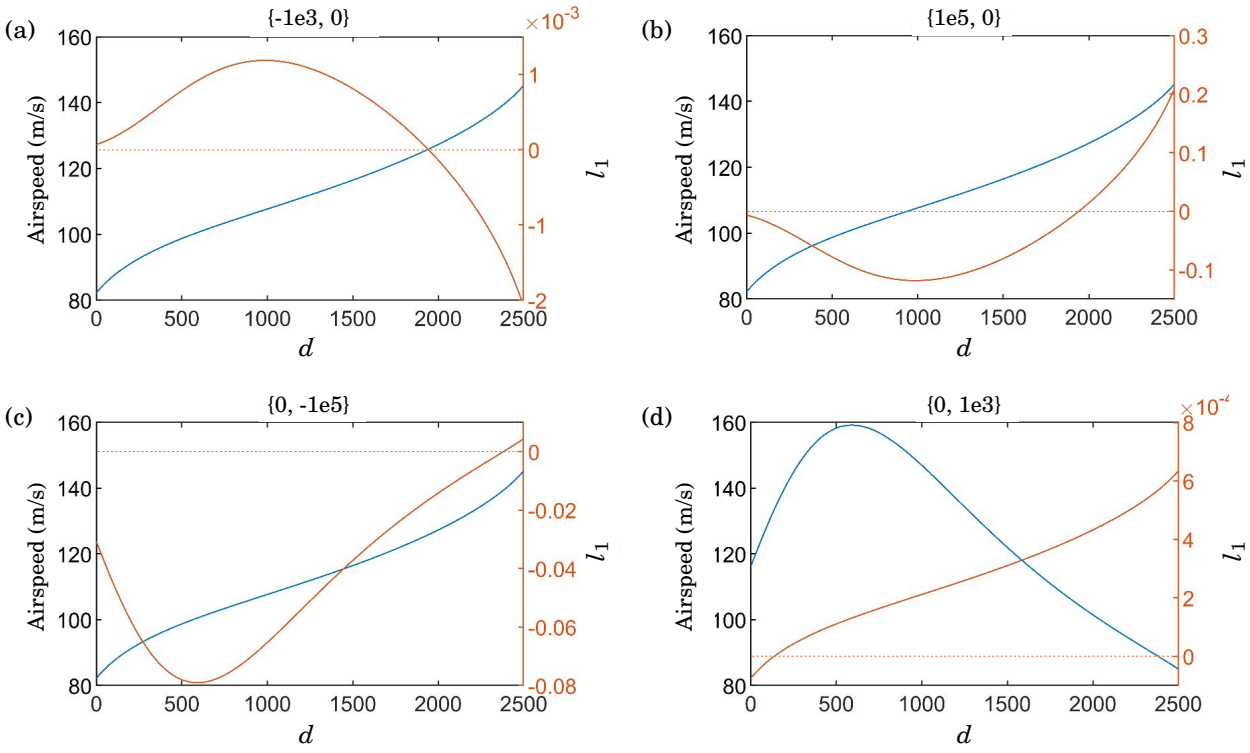

Figure 3.9: Two-parameter continuation of Hopf bifurcations, for varying d and airspeed, for 2 DoF wing ($l_1 > 0$ = subcritical, $l_1 < 0$ = supercritical).

.

3.3.2 Variation of structural stiffness

Another means of affecting Hopf criticality of the 2 DoF wing (3.8) is to parametrise the system in terms of bending and torsional structural stiffness. Unlike the structural damping parameter used in the previous section, these stiffness parameters are intrinsically related to the structural characteristics of the wing; their variation will more fundamentally affect the modes of the system, which in turn affects the flutter airspeed. However, as will be shown, the general phenomena relating to Hopf criticality are still found, and can be observed by varying either bending or torsional stiffness. Re-parameterising system (3.18) to include these terms, it may be written as

$$\dot{x} = A(v, d, EI, GJ)\, x + G(x^3), \tag{3.19}$$

where $EI, GJ \in \mathbb{R}$ are the bending and torsional stiffness parameters, respectively, with nominal values of 2e7 Nm^2 and 2e6 Nm^2 (Table 3.1). The structural damping parameter from Section 3.3.1 is now fixed at $d = 0$.

Figure 3.10 shows the LCO solutions for the increasing bending stiffness cases EI = 2e7, 4e7 and 5e7, for the nonlinear case {0, 1e5} (softening-torsion); here, GJ is fixed at its nominal value. The flutter airspeed can be seen to decrease as stiffness increases, and the nominal subcritical

Hopf is supercritical at EI = 5e7. Figure 3.11 shows the solutions for the decreasing torsional stiffness cases GJ = 2e6, 1e6 and 0.8e7, for {1e3, 0} (softening-bending), where EI is now fixed. The flutter airspeed similarly decreases and the nominal supercritical Hopf is subcritical at GJ = 0.8e6.

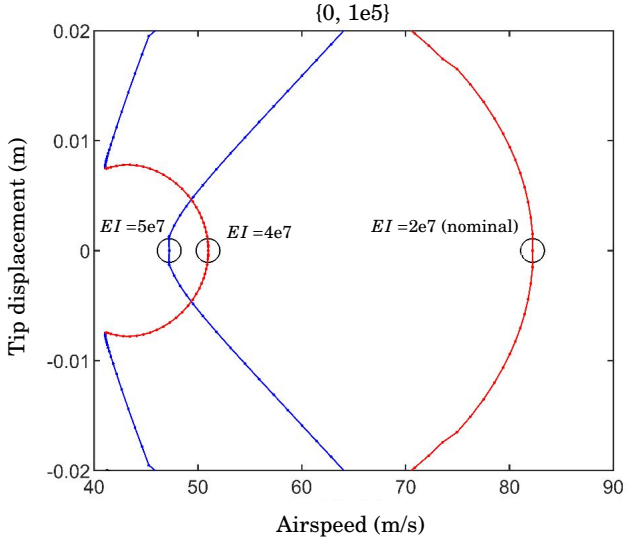

Figure 3.10: One-parameter continuation of LCOs, for varying airspeed, for 2 DoF wing when EI = 2e7, 4e7, and 5e7, where $\{\gamma_b, \gamma_t\}$ = {0, 1e5} (softening-torsion).

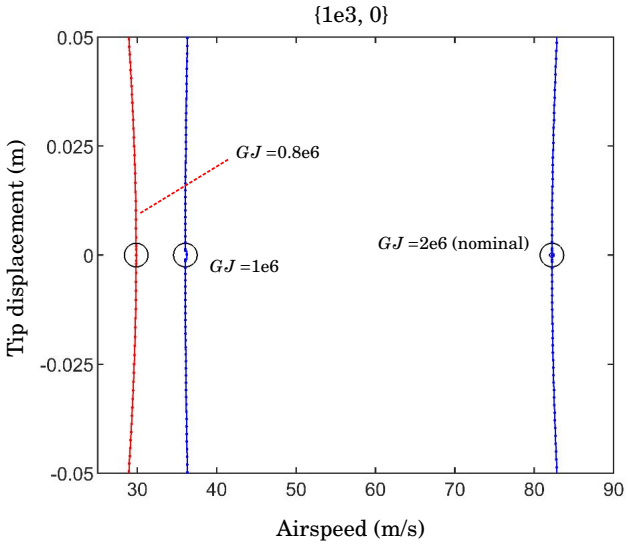

Figure 3.11: One-parameter continuation of LCOs, for varying airspeed, for 2 DoF wing when GJ = 2e6, 1e6, and 0.8e6, where $\{\gamma_b, \gamma_t\}$ = {1e3, 0} (softening-bending).

The frequencies of the modes corresponding to the cases shown in Figs. 3.10 & 3.11 are shown

in Fig. 3.12 and Fig. 3.13, respectively, where the vertical line indicates flutter. In the first case (Fig. 3.12), increasing EI increases the frequency of the lower mode (as expected), and thus moves it closer to the torsion-dominated upper mode. The compositions of the modes also change; the torsion mode gains an increasing bending component, and vice versa. At EI = 5e7, the original bending mode is almost entirely torsion-dominated. A similar outcome is observed when, instead, GJ is decreased (Fig. 3.13); here, the torsion mode is shifted down towards the bending mode, although both undergo a similar change in their composition. As can be seen from the last panels in both Figs. 3.12 & 3.13, the change in Hopf criticality coincides with when the two modes are practically intersecting at flutter.

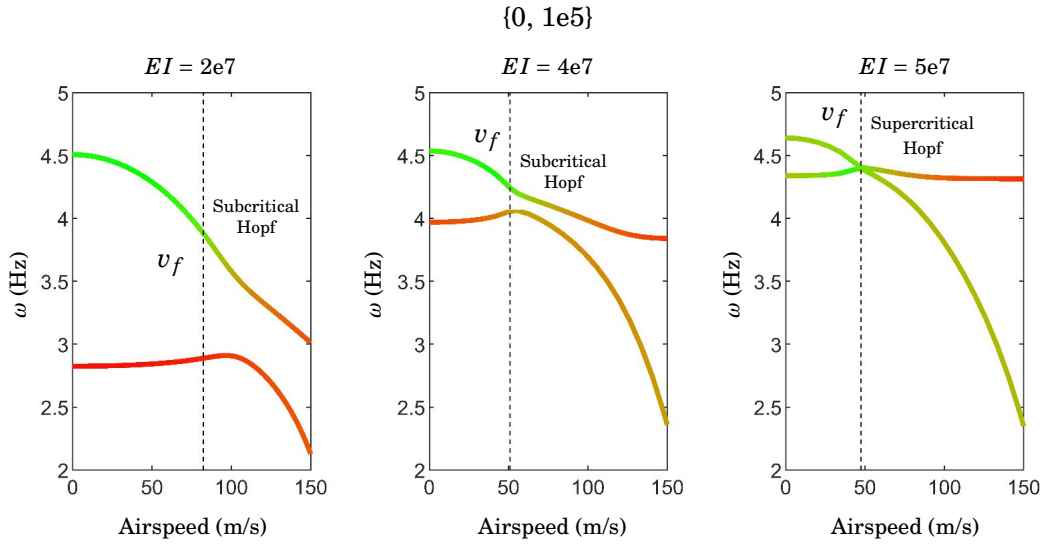

Figure 3.12: Variation of mode frequencies, for varying airspeed, for 2 DoF wing when EI = 2e7, 4e7, and 5e7, where $\{\gamma_b, \gamma_t\}$ = {0, 1e5} (softening-torsion).

Figure 3.14 shows the two-parameter continuation of Hopf points for varying EI and GJ, respectively, for the case $\{\gamma_b, \gamma_t\}$ = (a, e) {-1e5, 0}, (b, f) {1e3, 0}, (c, g) {0, 1e5} and (d, h) {0, -1e3}. As in Figs. 3.12 & 3.13, bending stiffness EI is increased from the nominal value, whereas torsional stiffness GJ is decreased; in all cases, varying the stiffness parameter therefore causes the modes to move closer together, and initially reduces the flutter airspeed. For every case, the sign of l_1 changes, which means that for every combination of softening/hardening nonlinearity and stiffness parameter, a change of Hopf criticality occurs due to the modes becoming closer.

The softening-torsion example of $\{\gamma_b, \gamma_t\}$ = {0, 1e5} and EI = 4e7 (the middle panel of Fig. 3.12), for which Fig. 3.10 revealed a subcritical Hopf, is now investigated with nonzero structural damping, to discover whether the criticality changes as indicated by the modes. Figure 3.15 shows the frequencies and LCO solutions for d = 1e3; the flutter point now occurs at a higher airspeed where the mode compositions have changed, and the Hopf is now supercritical, as expected.

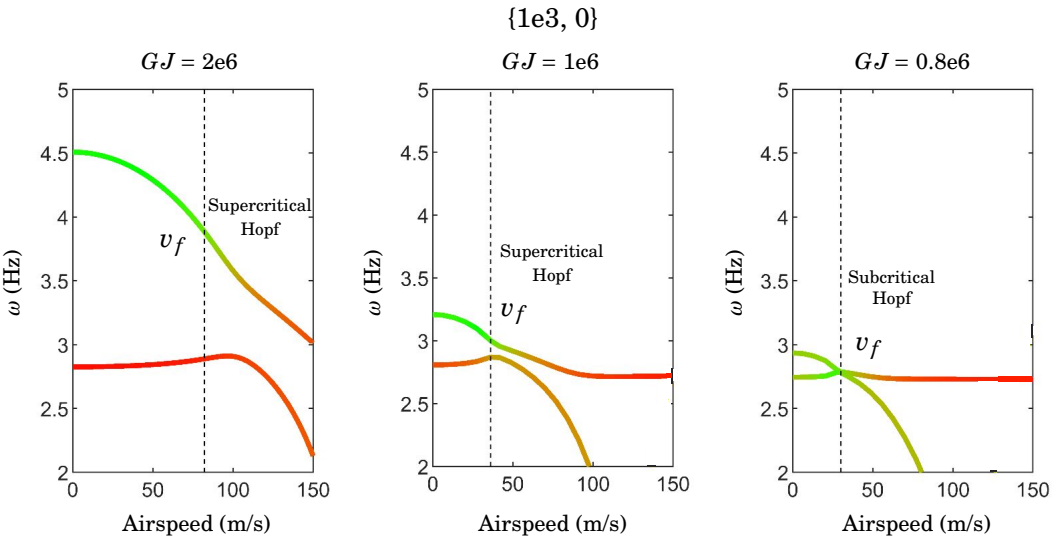

Figure 3.13: Variation of mode frequencies, for varying airspeed, for 2 DoF wing when GJ = 2e6, 1e6, and 0.8e6, where $\{\gamma_b, \gamma_t\}$ = {1e3, 0} (softening-bending).

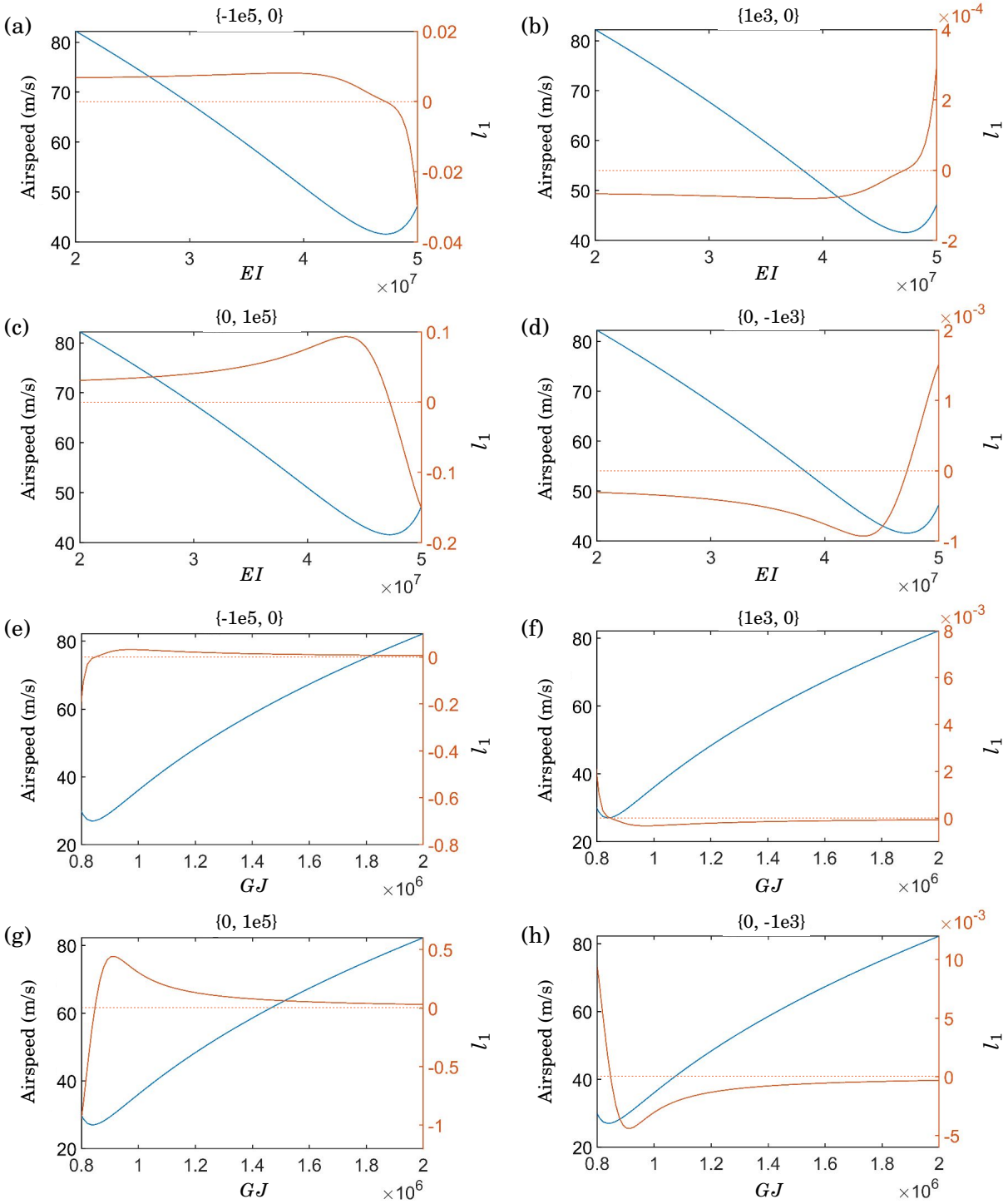

Figure 3.14: Two-parameter continuation of Hopf bifurcations, for varying stiffness and airspeed, for 2 DoF wing ($l_1 > 0$ = subcritical, $l_1 < 0$ = supercritical).

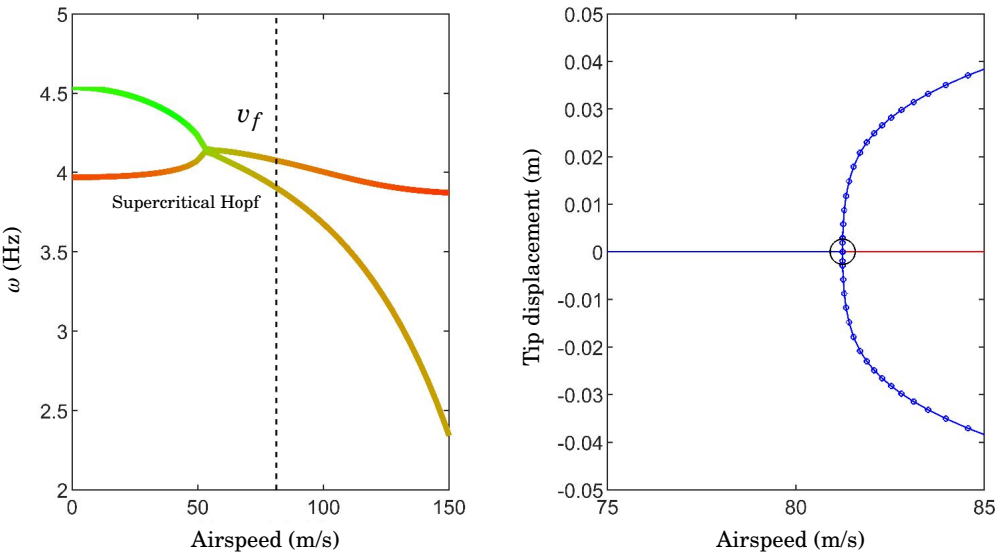

Figure 3.15: One-parameter continuation of LCOs, for varying airspeed, for 2 DoF wing when EI = 4e7, $\{\gamma_b, \gamma_t\}$ = {0, 1e5} and d = 1e3.

3.4 Conclusions

This chapter has combined analytical and physical approaches to investigate the underlying phenomena that govern nonlinear Hopf criticality in flexible, high-aspect-ratio wings. Using a simple, 2 degree-of-freedom (DoF) nonlinear binary flutter wing model, it was shown that the properties of the linearised system, specifically the convergence of the varying mode frequencies, can be related to the criticality (i.e. the supercritical or subcritical nature) of the Hopf bifurcation at the flutter airspeed. Given this insight, it was shown that the criticality of the flutter point could readily be changed, via the variation of either structural damping or stiffness parameters; the same observations were made, regardless of the parameter being varied, or the type of softening/hardening nonlinearity. The nonlinearity in this model was easily characterised in terms of cubic stiffness prescribed by the parameters; in more complex aeroelastic systems, which better approximate real-life wings, the nonlinear effects cannot be expressed as explicitly, and many more structural modes are captured. However, since classical binary flutter (i.e. a critical interaction of two structural modes) is the most typical physical route through which flutter occurs, it is possible that the basic observations from the 2 DoF wing may be observable regardless of the complexity of the model. While nonlinear techniques must be used to fully obtain the dynamics of high-aspect-ratio wings with geometric nonlinearity, this chapter has shown how the modes of the linearised system can provide a useful indication - potentially a ‘rule of thumb’ - of the nonlinear behaviour near the flutter point.

CHAPTER 4

NONLINEAR DYNAMICS OF A HIGH-ASPECT-RATIO WING

This chapter examines the nonlinear dynamics of a flexible, high-aspect-ratio wing. One-parameter continuation is used to obtain equilibria and limit cycle oscillations (LCOs), and complex dynamical phenomena are found to exist in the nominal system. Two-parameter continuation of Hopf and periodic fold bifurcations reveals how the nominal dynamics change as the wing stiffness is varied. Critically, it is shown that subcritical LCOs exist due to geometric nonlinearity alone. The criticality of the Hopf bifurcation is then changed by varying the damping and stiffness of the wing. Results and discussions in this chapter are partly derived from Ref. [4].

4.1 Introduction

The focus of Chapter 3 concerned the criticality of Hopf bifurcations occurring in a simple, 2 DoF nonlinear model of a flexible wing. Whilst knowledge of Hopf criticality provides valuable insight into wing behaviours near the bifurcation point, models that better represent real-life wings may exhibit more complex dynamics away from the equilibrium. The presence of many structural modes in more realistic models means that multiple flutter interactions are possible as the wing deforms; thus, in addition to Hopf criticality, the limit cycle oscillation (LCO) solutions must be investigated for additional bifurcations.

In this chapter, an aeroelastic formulation derived from the theory of Howcroft *et al.* [6] is used to model the nonlinear dynamics of a flexible, high-aspect-ratio wing. The method of Howcroft *et al.* comprises a reduced-order approach, which uses a basis of shape functions to define sets of Euler angles that describe the deformation of a 1D beam using minimal system states (further discussed in Section 4.2). Large deformations of the beam-like wing are thus captured, and the re-orientation of aerodynamic load vectors, which occurs as the wing deforms, are also accounted for.

In order to examine the *geometric nonlinearity* of the high-aspect-ratio wing alone, the beam formulation of Ref. [6] is combined with quasi-steady, linear, strip theory aerodynamics. The wing in question is the high altitude, long endurance (HALE) wing previously studied by Patil *et al.* [71–73], which was first discussed in Section 2.4. The HALE wing has a half-span of 16m, with an aspect ratio of 16; Fig. 4.1 shows a view of the wing in a global inertia frame, in an arbitrary deformed equilibrium condition. One-parameter continuation will be used to directly obtain equilibria and LCOs, for varying airspeed; the two-parameter continuation of bifurcations (i.e. Hopf points and periodic folds) will then be used to reveal the sensitivity of these dynamics to variations in out-of-plane, in-plane and torsional stiffness, and a 'wash out' stiffness coupling parameter. As an extension to the discussion in Chapter 3, the criticality of the Hopf bifurcation occurring at the flutter airspeed is then investigated.

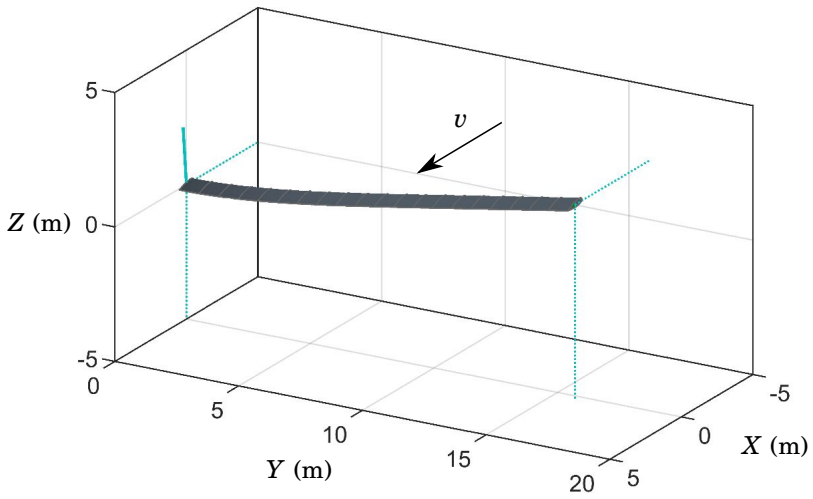

Figure 4.1: Visualisation of HALE wing in a global inertial frame.

4.2 Aeroelastic formulation

The aeroelastic formulation used in this chapter is based on the beam theory of Howcroft *et al.* [6]; the reader is directed to this paper for rigorous derivation and for comparisons against other low-order modelling approaches. Also, see Howcroft *et al.* [91, 92]. The following mathematical summary is derived from Ref. [6]; however, some terms are simplified due to the absence of shear, extensional effects or pre-curvature of the wing.

The formulation is based on a geometrically exact kinematic description of a 1D beam. Let $\Gamma_{[G]}(s)$ denote a reference line of length L, in coordinate frame $[G]$, where $s \in [0, L]$ is a curvilinear spanwise coordinate, and define $\bar{r}_A$ as shown in Fig. 4.2. Let the vectors $e_x(s)$, $e_y(s)$ and $e_z(s)$ define the intrinsic/local coordinate frame $[I]$ at a given spanwise location s, where e_y is tangent

to the local spanwise direction and e_x and e_z align with the cross sectional axis of the beam, as shown in Fig. 4.2. Thus, the beam reference can be expressed as

$$\Gamma_{[G]}(s) = \bar{r}_A + R_{G,A} \int_0^L e_{y[G]}(s)\, \mathrm{d}s, \tag{4.1}$$

where $R_{G,A}$ is defined as an arbitrary 3×3 matrix that rotates the coordinate system at the wing root, $[A]$, relative to $[G]$. In the present study, coordinate systems $[G]$ and $[A]$ share the same origin, so the vector $\bar{r}_A$ is 0.

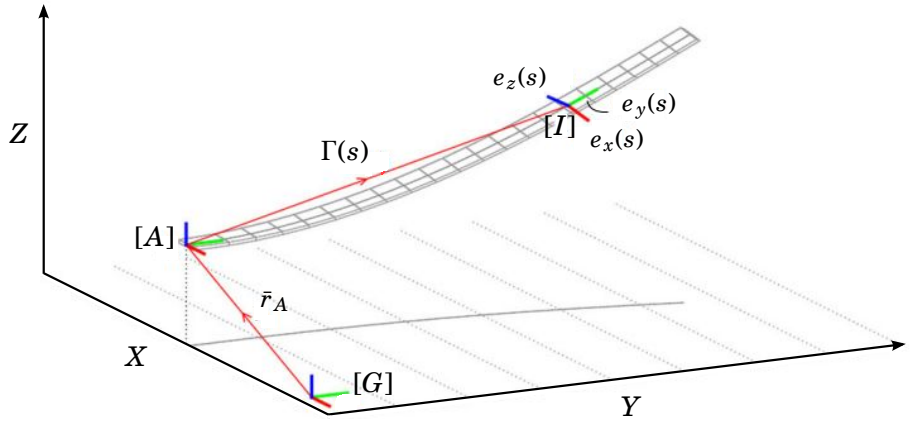

Figure 4.2: Kinematic description of a flexible, high-aspect-ratio wing, showing local coordinate frame at one spanwise discretisation point [6].

The intrinsic system $[I]$ is defined along the beam via a *3-1-2 Euler angle* parameterisation, which is related to $[A]$ by the mapping

$$\begin{aligned} \mathbf{e}_{[A]} &= \left(e_{x[A]} \,|\, e_{y[A]} \,|\, e_{z[A]} \right) \\ &= \begin{pmatrix} \cos(\psi)\cos(\phi) + \sin(\theta)\sin(\psi)\sin(\phi) & \cos(\theta)\sin(\psi) & \cos(\psi)\sin(\phi) - \sin(\theta)\sin(\psi)\cos(\phi) \\ -\sin(\psi)\cos(\phi) + \sin(\theta)\cos(\psi)\sin(\phi) & \cos(\theta)\cos(\psi) & -\sin(\psi)\sin(\phi) - \sin(\theta)\cos(\psi)\cos(\phi) \\ -\cos(\theta)\sin(\phi) & \sin(\theta) & \cos(\theta)\cos(\phi) \end{pmatrix}. \end{aligned} \tag{4.2}$$

The virtual work contributions from internal strain (δW_K), structural damping (δW_C), applied forces (δW_F), applied moments (δW_M), translational inertia ($\delta W_{T(\text{trans.})}$) and rotational inertia ($\delta W_{T(\text{rot.})}$) can be written as the integrals

$$\delta W_K = \int_0^L F_{K[I]} \cdot \delta\kappa_{[I]}\, \mathrm{d}s, \tag{4.3}$$

$$\delta W_C = \int_0^L F_{C[I]}\left(\dot{\kappa}_{[I]}\right) \cdot \delta\kappa_{[I]}\, \mathrm{d}s, \tag{4.4}$$

$$\delta W_F = \int_0^L F_{[A]} \cdot \delta r_{F[A]}\, \mathrm{d}s, \tag{4.5}$$

$$\delta W_M = \int_0^L M_{[A]} \cdot \delta \vartheta_{[A]} \, \mathrm{d}s, \tag{4.6}$$

$$\delta W_{T(\text{trans.})} = \int_0^L -\frac{\mathrm{d}}{\mathrm{d}t}\left(m\dot{r}_{m[A]}\right) \cdot \delta r_{m[A]} \, \mathrm{d}s, \tag{4.7}$$

$$\delta W_{T(\text{rot.})} = \int_0^L -\frac{\mathrm{d}}{\mathrm{d}t}\left(\mathbf{e}_{[A]} I_{\vartheta[I]} \mathbf{e}_{[A]}^T \dot{\vartheta}_{[A]}\right) \delta \vartheta_{[A]} \, \mathrm{d}s. \tag{4.8}$$

In contributions (4.3) and (4.4), the variation of curvature along the beam $\delta\kappa_{[I]}$ is given by

$$\delta\kappa_{[I]}(s) = \left(\delta\kappa_x, \delta\kappa_y, \delta\kappa_z\right)^T = \left(\delta\left[e'_{y[A]} \cdot e_{z[A]}\right], \delta\left[e'_{z[A]} \cdot e_{x[A]}\right] s, \delta\left[e'_{x[A]} \cdot e_{y[A]}\right]^T\right), \tag{4.9}$$

where $(\circ)'$ denotes differentiation with respect to s. Linear structural stiffness and damping relationships are assumed, so $F_{K[I]} = -\overline{K}\kappa$ and $F_{C[I]} = -\overline{C}\dot{\kappa}$. In the absence of shear effects, the stiffness matrix can be expressed as

$$\overline{K} = \begin{pmatrix} EI_{\text{out}} & 0 & 0 \\ 0 & GJ & 0 \\ 0 & 0 & EI_{\text{in}} \end{pmatrix}, \tag{4.10}$$

where EI_{out}, GJ and EI_{in} are the out-of-plane bending, torsional and in-plane bending stiffnesses, respectively. In this study, the structural damping is proportional to stiffness, so $\overline{C} = d\overline{K}$.

The applied forces $F_{[A]}$ and moments $M_{[A]}$ in (4.5) and (4.6) are prescribed by the gravitational and aerodynamic loads on the wing. In the present work, linear, quasi-steady 2D strip theory aerodynamics are implemented and loads are computed based on the effective angle of attack, at a spanwise distribution of strips, using the strip orientation and local velocity vector. The apparent flow vector at a given strip is defined by

$$\overline{v}_{\text{flow}} = \overline{v}_\infty - \frac{\mathrm{d}}{\mathrm{d}t}\Gamma_{a[G]}, \tag{4.11}$$

where $\bar{v}_\infty$ is the global free stream velocity vector (magnitude equal to airspeed v), and Γ_a is the position vector[1] of the strip at a chosen aerodynamic control point (e.g. 3/4 chord). The apparent flow vector $\overline{v}_{\text{flow}}$ is effectively the flow seen by the panel in the global coordinate system. The effective angle of attack of an arbitrary strip is given by

$$\alpha_{\text{eff.}} = \tan^{-1}\left(\frac{\overline{v}_z}{\overline{v}_x}\right), \tag{4.12}$$

where $\overline{v}_z$ and $\overline{v}_x$ are the components of $\overline{v}_{\text{flow}}$ (4.11) mapped onto the intrinsic system $[I]$ defined by e_x, e_y and e_z (see Fig. 4.2). The aerodynamic load vectors per span can be expressed as

$$F_{[G]\text{aero.}}(s) = \frac{1}{2}\rho v^2 a \, C_L(\alpha_{\text{eff}}) \, e_z(s), \qquad M_{[G]\text{aero.}}(s) = \frac{1}{2}\rho v^2 a e_c \, C_L(\alpha_{\text{eff}}) \, e_z(s) \tag{4.13}$$

[1] Note that the Z direction is positive upwards.

where ρ is air density, v is airspeed, a is the strip area and e_c is the offset from the beam axis. Aerofoil sections comprise NACA0012 profiles, and in each case, $C_L(\alpha_{\text{eff}})$ is linear with gradient 2π. In this study, loads are computed at a discrete set of 20 spanwise stations located along the wing. In the absence of stall, large twist angles are permitted, however these would not occur in practice. The term $\delta r_{F[A]}$ in (4.5) describes the variation caused by the applied force, accounting for offsets, and is given by

$$\delta r_{F[A]} = \delta\Gamma_{[A]} + e_{x[A]} + e_{z[A]} \tag{4.14}$$

The variational rotation along the beam in (4.6) and (4.8) is given by

$$\delta\vartheta_{[A]}(s) = \frac{1}{2}\left(e_{x[A]} \times \delta e_{x[A]} + e_{y[A]} \times \delta e_{y[A]} + e_{z[A]} \times \delta e_{z[A]}\right). \tag{4.15}$$

In (4.7), r_m denotes the mass reference line of the beam which, in the present study, is coincident with the beam axis, so $r_m = \Gamma$. In (4.8), $I_{\theta[A]}$ is the 3×3 mass moment of inertia matrix about $\Gamma_{[A]}$.

In order to assemble the equations of motion of the wing, a basis set of kinematic shape functions, $B(s)$, are first selected and combined with a set of time-varying generalised coordinates, $q(t)$. The shapes $B(s)$ describe the spanwise variation of the 3-1-2 Euler angles and so define the 3D deformation of the beam; combining with $q(t)$ therefore describes the spanwise and *time-varying* deformation. The variation of the Euler angles are thus expressed by

$$\phi(s,\,t) = \sum B_\phi(s)\,q_\phi(t),\;\; \psi(s,\,t) = \sum B_\psi(s)\,q_\psi(t),\;\; \text{and}\;\; \theta(s,\,t) = \sum B_\theta(s)\,q_\theta(t), \tag{4.16}$$

which may be written as

$$\zeta(s,\,t) = \sum B(s)\,q(t). \tag{4.17}$$

In this work, scaled Chebyshev polynomials of the first kind are used for $B(s)$ (see Ref. [91] for a comparison of various different shape functions); see Fig. 4.3. The subsets $B_\phi(s)$, $B_\psi(s)$, and $B_\theta(s)$ are allocated 5, 3 and 4 functions respectively in this study.

The beam reference line Γ is therefore a *nonlinear* function of both the kinematic shape functions $B(s)$ and generalised coordinates $q(t)$. The spanwise twist of the beam, ϑ, can be similarly expressed; hence,

$$\Gamma_{[A]}(s,\,t) = \Gamma_{[A]}\big(B(s),\,q(t)\big) \;\;\text{and}\;\; \vartheta_{[A]}(s,\,t) = \vartheta_{[A]}\big(B(s),\,q(t)\big). \tag{4.18}$$

According to d'Alembert's principle, considering the virtual work performed with respect to the state vector $q \in \mathbb{R}^i$ yields the system of equations

$$\frac{\partial W_T}{\partial q} + \frac{\partial W_C}{\partial q} + \frac{\partial W_K}{\partial q} + \frac{\partial W_F}{\partial q} + \frac{\partial W_M}{\partial q} \;=\; \sum_i \frac{\partial W_i}{\partial q}\big(q(t),\,\dot{q}(t),\,\ddot{q}(t),\,B(s),\,B'(s)\big) = \;0 \tag{4.19}$$

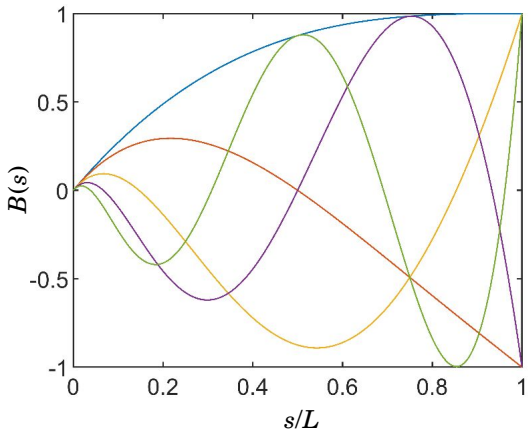

Figure 4.3: Scaled Chebyshev polynomials used as kinematic shape function set.

where i is the total number of shape functions used; in the present work, $q \in \mathbb{R}^{12}$. Combining with the virtual work terms in (4.3) - (4.8), system (4.19) becomes

$$\int_0^L \left(F_{[A]} \cdot \frac{\partial \Gamma_{[A]}}{\partial q} + M_{[A]} \cdot \frac{\partial \vartheta_{[A]}}{\partial q} - (\overline{K}\kappa) \cdot \frac{\partial \kappa_{[I]}}{\partial q} - (\overline{C}\dot{\kappa}) \cdot \frac{\partial \kappa_{[I]}}{\partial q} \right. \\ \left. - \frac{\mathrm{d}}{\mathrm{d}t}\left(m\dot{\Gamma}_{[A]}\right) \cdot \frac{\partial \Gamma_{[A]}}{\partial q} - \frac{\mathrm{d}}{\mathrm{d}t}\left(\mathbf{e}_{[A]} I_{\vartheta[I]} \mathbf{e}_{[A]}^T \dot{\vartheta}_{[A]}\right) \cdot \frac{\partial \vartheta_{[A]}}{\partial q} \right) \mathrm{d}s \;=\; 0. \tag{4.20}$$

Rearranging the kinetic virtual work terms that depend on $\ddot{q}$, as described in Ref. [6], leads to final equations of motion that take the generalised 2$^{\text{nd}}$ order form

$$\boldsymbol{M}\ddot{q} = -\boldsymbol{w} + \int_0^L \left(F_{[A]} \cdot \frac{\partial \Gamma_{[A]}}{\partial q} + M_{[A]} \cdot \frac{\partial \vartheta_{[A]}}{\partial q} - (\overline{K}\kappa) \cdot \frac{\partial \kappa_{[I]}}{\partial q} - (\overline{C}\dot{\kappa}) \cdot \frac{\partial \kappa_{[I]}}{\partial q} \right) \mathrm{d}s, \tag{4.21}$$

where expressions for $\boldsymbol{M}$ and $\boldsymbol{w}$ are provided in Appendix A.2. Alternatively, (4.21) may be expressed as

$$\underbrace{\boldsymbol{M}\left(q(t),\, B'(s)\right)}_{12\times 1} \ddot{q} = \underbrace{\boldsymbol{g}\left(q(t),\, \dot{q}(t),\, B(s),\, B'(s)\right)}_{12\times 1}. \tag{4.22}$$

In first-order form, the equations of motion can be written as

$$\frac{\mathrm{d}}{\mathrm{d}t}\begin{pmatrix} q \\ \dot{q} \end{pmatrix} = \underbrace{\begin{pmatrix} \dot{q} \\ \boldsymbol{M}^{-1}\boldsymbol{g} \end{pmatrix}}_{24\times 1}. \tag{4.23}$$

Since the choice of $B(s)$ in this formulation is arbitrary, the integral terms within $\boldsymbol{M}$ and $\boldsymbol{g}$ are computed numerically and are not expressed analytically; in the present work, computation is performed at 201 discrete spanwise points along the wing.

4.3 Nominal wing configuration

The nonlinear dynamics of the HALE wing described by (4.23) can be described by the parameterised, first-order form

$$\dot{x} = f(x, v), \tag{4.24}$$

where $x \in \mathbb{R}^{24} = [q_1 ... q_{12}, \dot{q}_1 ... \dot{q}_{12}]^T$ and $v \in \mathbb{R}$ is airspeed.

Table 4.1 shows the parameters of the nominal wing. A fixed, non-zero root angle of attack α_0 is chosen, ensuring static deformation with airspeed, and gravitational loads are included. Since the aerodynamics used in this study are both linear and quasi-steady, to allow the examination of geometric nonlinearity, aeroelastic results are not targeted to quantitatively match the time histories shown in Ref. [73], which account for unsteady and stall effects [93, 94]. The structural model, however, can be readily verified via the comparison of structural natural frequencies, for increasing static tip displacement at zero airspeed and with zero gravity. Fig. 4.4 shows the frequencies obtained by applying increasing vertical tip loads and linearising system (4.24) about each static solution. It can be seen that the frequencies of the coupled in-plane bending and torsional modes (Fig. 4.4, pts. b & c) change significantly with deflection; recall, from Section 2.4, that the variation of these modes was the cause of the reduced-airspeed flutter results in the study by Patil *et al.* [73]. Frequencies from Refs. [71, 73] are shown in black; the small, quantitative discrepancies between these and frequencies of the present model are attributed to the use of a coarse finite-element mesh in the previous studies. A +11.8% error against an alternate Rayleigh-Ritz method is stated in Ref. [71] for the 3$^{\text{rd}}$ out-of-plane bending frequency at zero deflection. The undeformed frequencies obtained in the present work, however, are in good agreement with analytical calculations using exact beam theory. Table 4.2 shows a comparison of the first five undeformed modes (see Appendix A.3 for formulae used for exact values).

Table 4.1: Nominal HALE wing parameters from Ref. [71].

Original parameters	
Wing	
Semi-span	16 m
Chord	1 m
Mass per unit length	0.75 kg/m
Out-of-plane stiffness (EI_{out})	2×10^4 N m^2
In-plane stiffness (EI_{in})	4×10^6 N m^2
Torsional stiffness (GJ)	1×10^4 N m^2
Moment of inertia	0.1 kg m^2
Spanwise elastic axis	0.5 chord
Centre of gravity	0.5 chord
Flight condition	
Altitude	20 km
Air density	0.0889 kg/m^3
Additional parameters	
Aerofoil	NACA0012
Root angle of attack	5°
Structural damping factor (d)	1×10^{-3}
Stiffness coupling factor (K)	0

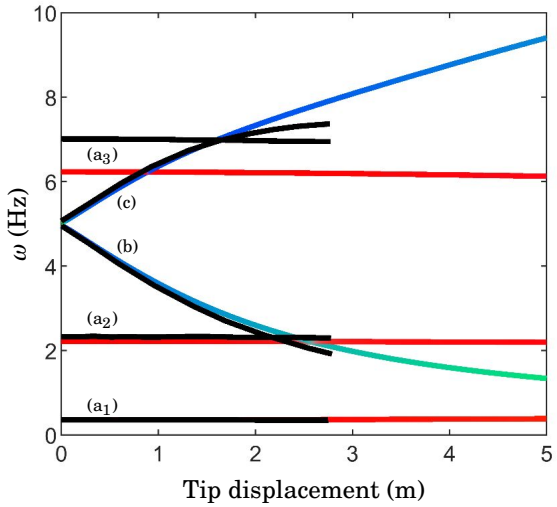

Figure 4.4: Variation of HALE wing natural frequencies with static tip deflection: (a) out-of-plane, (b) torsion/in-plane and (c) in-plane/torsion (black from Refs. [71, 73]).

Table 4.2: Comparison of undeformed HALE mode frequencies.

Mode	ω (Hz)			
	Ref. [71]	Exact	Present	Error
1st out-of-plane bending	0.358	0.357	0.357	0.00%
2nd out-of-plane bending	2.325	2.237	2.225	-0.54%
1st torsion	4.957	4.941	4.941	0.00%
1st in-plane bending	5.051	5.048	5.042	-0.12%
3rd out-of-plane bending	7.005	6.312	6.234	-1.24%

4.4 Nominal wing bifurcation results

The dynamics of the nominal wing configuration (defined per Table 4.1) are first obtained. Numerical integration of (4.24) is initially used to find a number of steady deflected wing shapes (i.e. static aeroelastic equilibria) at increasing subcritical airspeeds; see Fig. 4.5. Figure 4.6 shows the response of the wing when a gradual airspeed ramp (22.5 m/s - 24 m/s) is applied and reveals the emergence of an LCO. The growth of this LCO amplitude is rapid, indicating the presence of a subcritical Hopf bifurcation (see Fig. 2.6 for a generic illustration of this type of nonlinear flutter outcome).

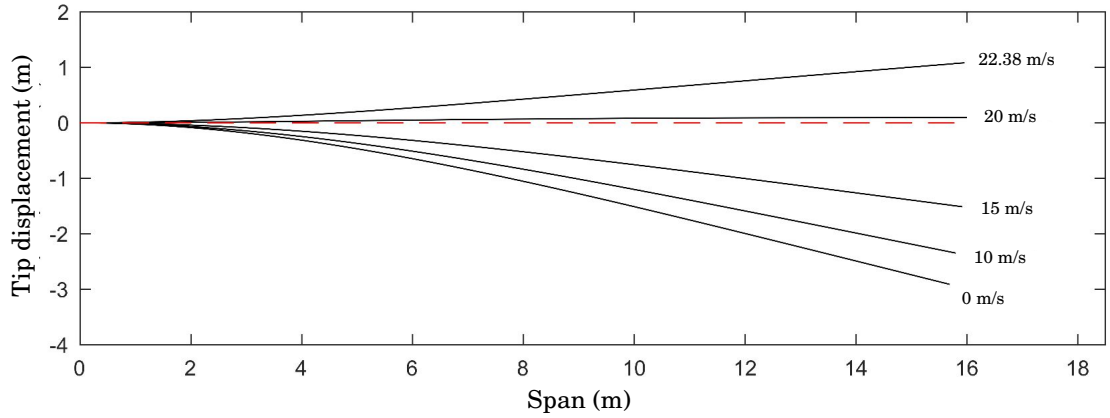

Figure 4.5: Deflected equilibria of the HALE wing, for various airspeeds before flutter.

Starting from one of the static solutions shown in Fig. 4.5, one-parameter numerical continuation is now used. Figure 4.7 shows the continuation of equilibria and LCOs of (4.24) as airspeed varies, and plots solutions in terms of vertical tip displacement (upper panel) and tip twist (lower panel). In both cases, the minimum and maximum of the LCOs are shown. For low airspeeds, a single branch of stable equilibria exists, the magnitude of which increases steadily as airspeed increases (the variation of tip displacement can be related to Fig. 4.5). This equilibria solution undergoes a Hopf bifurcation and becomes unstable at 22.38 m/s; at this point, which is labelled

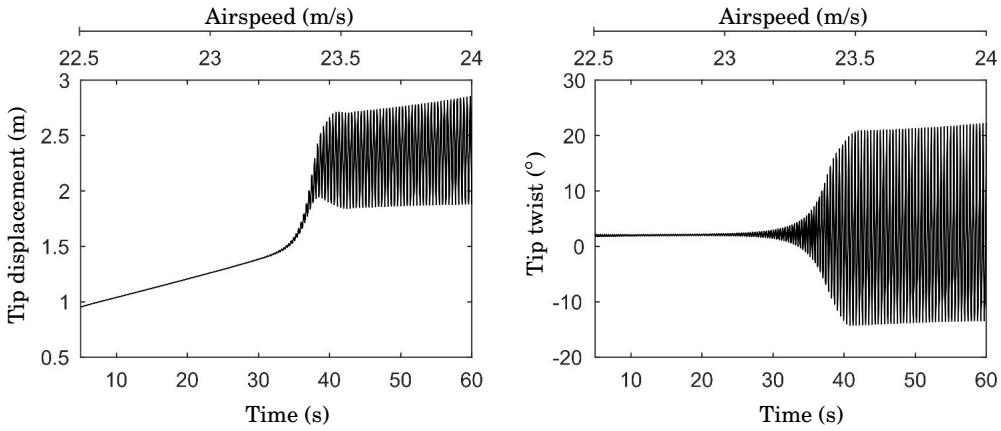

Figure 4.6: Time histories, showing response of the HALE wing to a gradual airspeed ramp (22.5 m/s - 24 m/s).

v_f to indicate the nonlinear flutter airspeed, the tip displacement is 1.08m and the tip twist is 2.01° (total angle of attack is 6.98°). The flutter frequency is 3.37 Hz. The Hopf bifurcation is subcritical, as is demonstrated by the emergent unstable LCO. The unstable LCO solution undergoes a number of periodic folds, at increasing amplitudes, alternating between unstable and stable solutions, before undergoing a final fold at approximately 25.56 m/s. The resulting unstable solution subsequently leaves the near-equilibria region and is not plotted beyond this point (it is found that these LCOs comprise very large wing deformations). The LCOs at points (a), (b) and (c) will be discussed later. Figure 4.8 shows the variation of frequencies and damping, for increasing airspeed, for the nominal wing; these are obtaining via linearisation of the nonlinear system (4.24) at each of the equilibrium solutions shown in Fig. 4.7. The inclusion of in-plane bending is reflected in the colouring of the modes, which is defined by: red = out-of-plane bending, green = torsion, blue = in-plane bending. Since the wing is modelled with a nonzero angle of attack that permits static deformation as a function of airspeed, the variation of the aeroelastic modes in Fig. 4.8 is due to a *combination* of varying aerodynamic stiffness/damping and geometric nonlinearity (in Section 3.3, in the absence of static deformation, frequency variation was due to aerodynamic loads alone). Due to this, indications of how the frequencies vary with *deformation* are contained within Fig. 4.8; this idea will be revisited in Section 4.7. From the damping in Fig. 4.8 it can be seen that the mode that loses stability is a mode comprising strongly-coupled torsional/in-plane motion, which is in agreement with Patil *et al.* [73]. Note that the out-of-plane bending mode with lowest frequency in Fig. 4.8 is found to separate into two distinct real modes at 18.4 m/s.

Figure 4.9 illustrates the time histories from Fig. 4.6 superimposed onto the corresponding continuation solution in Fig. 4.7. It can be seen that the time histories closely match the continuation result, although the system is slow to to enter into the LCO once the flutter airspeed is exceeded and the equilibrium is unstable.

The continuation solutions in Fig. 4.7 show that subcritical LCOs are present near the

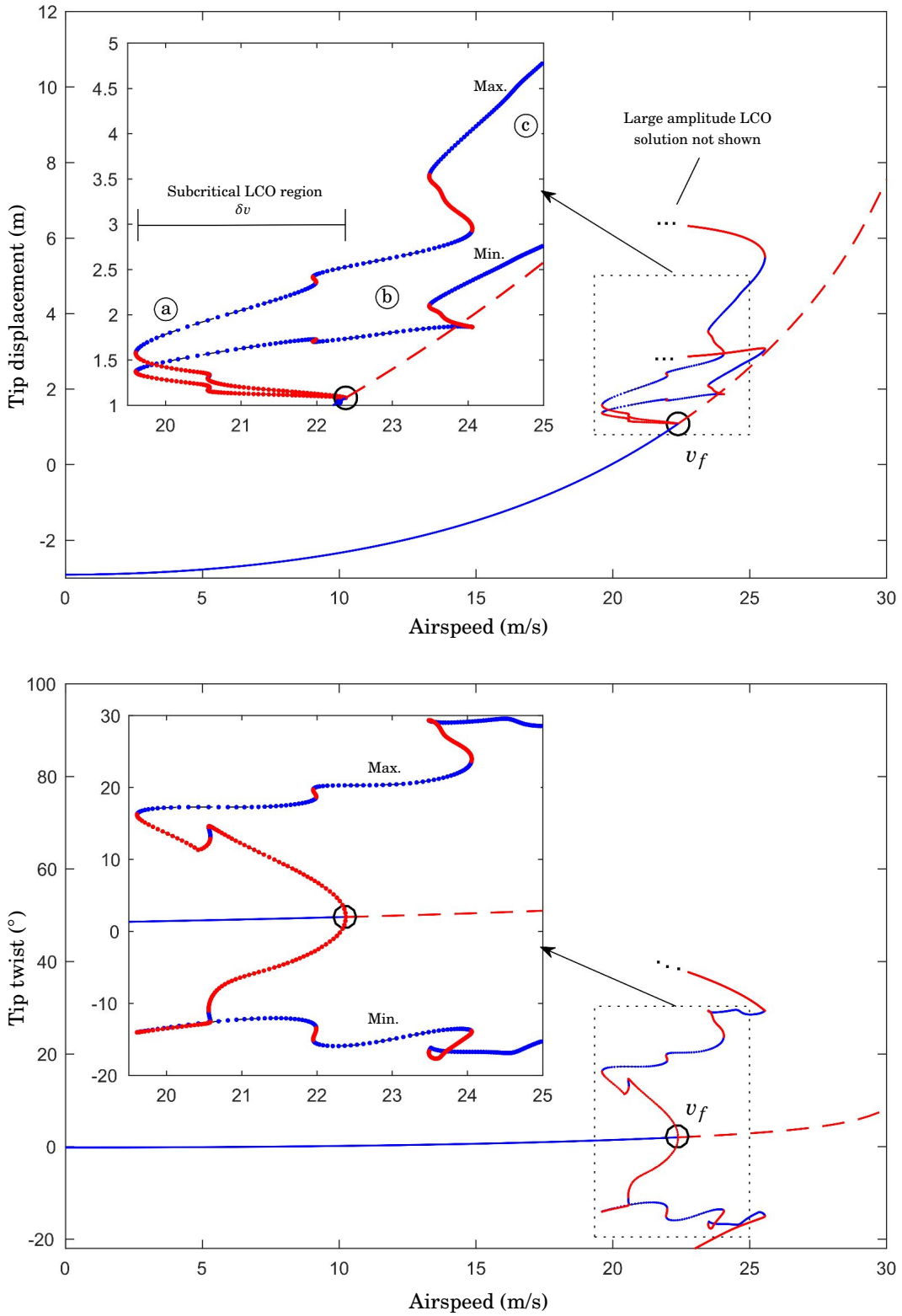

Figure 4.7: One-parameter continuation of equilibria and LCOs, for varying airspeed, for the HALE wing. LCOs at (a), (b) and (c) are shown in Fig. 4.11.

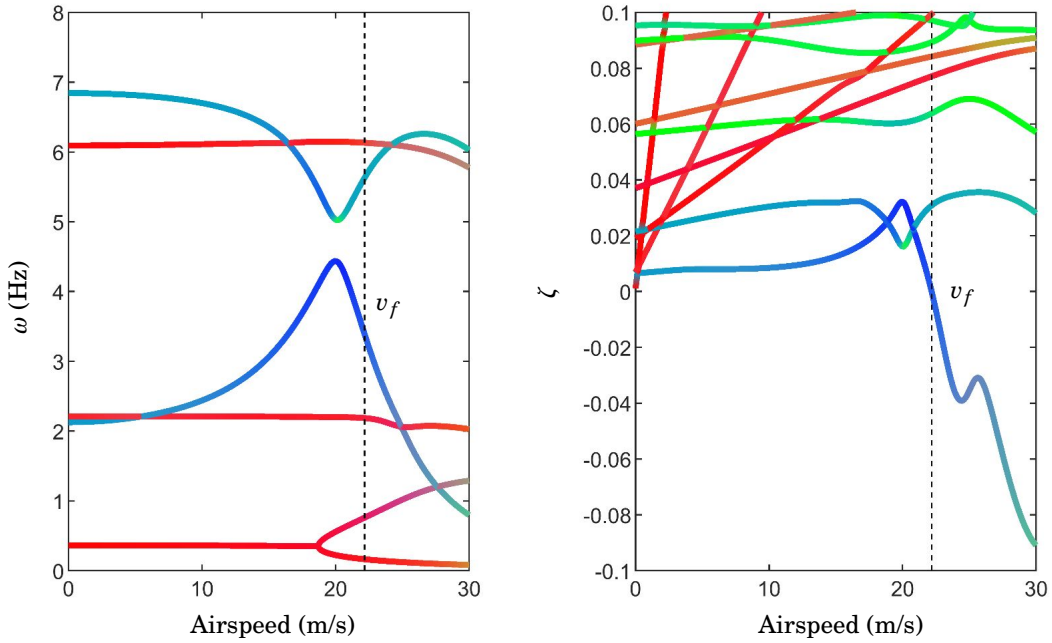

Figure 4.8: Variation of mode frequencies and damping, for varying airspeed, for nominal HALE wing (red = out-of-plane bending, green = torsion and blue = in-plane bending).

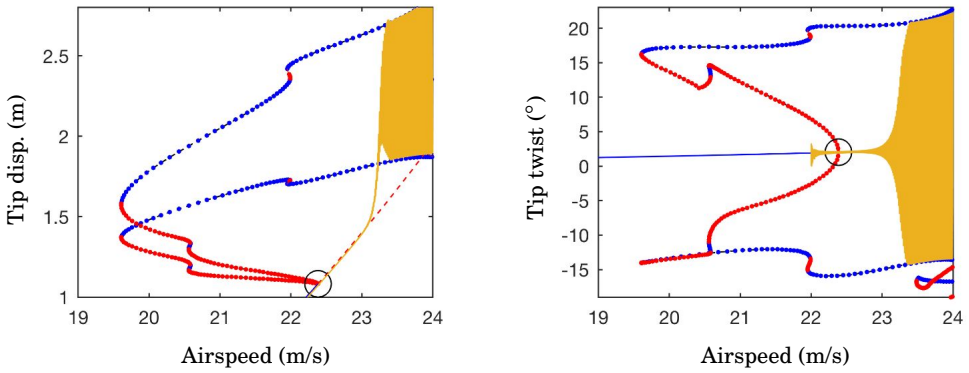

Figure 4.9: Time histories from Fig. 4.6 superimposed onto the continuation solution in Fig. 4.7.

equilibria for airspeeds as low as 19.61 m/s; thus, the subcritical LCO region δv (which can be defined as the airspeed interval between the Hopf and the lowest-airspeed fold, see Fig. 4.7), is equal to 2.77 m/s. A useful metric is the ratio $\delta v/v_f$, which quantifies the subcritical LCO region relative to the nonlinear flutter airspeed; in this case, this ratio is 0.124. Figure 4.10 shows the wing response when a *decreasing* airspeed ramp is applied to the final state of the time history shown in Fig. 4.6. In this reversed case, the LCO is sustained below v_f, and thus the hysteresis

in the system is evident.

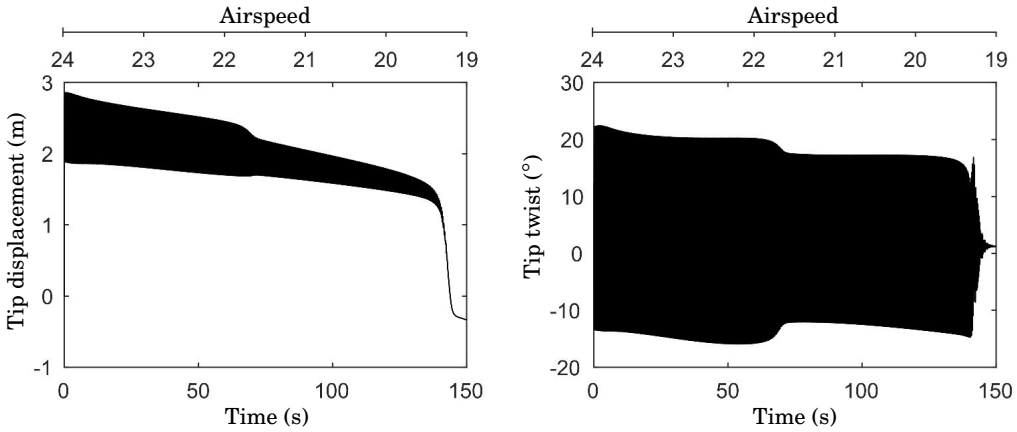

Figure 4.10: Time histories, showing response of the HALE wing to a decreasing airspeed ramp (24 m/s - 19 m/s).

The characteristics of the individual LCOs located at the selected points on Fig. 4.7 are now shown. Figure 4.11 shows a time history, frequency decomposition and spanwise deformation for each of the solutions at (a) 20 m/s, (b) 23 m/s, and (c) 25 m/s. For each case, the spanwise deformation is shown for the instances where the tip displacement and twist are at the maximum, minimum and mid value of the oscillation. The LCOs at 20 m/s and 23 m/s show evidence of the 2^{nd} out-of-plane bending mode of the wing, whereas the larger LCO at 25 m/s shows a presence of the 1^{st} bending mode. In all three cases, the first torsion mode is present; thus, the physical characteristics of the LCOs can be related to Fig. 4.4, which shows that the 1^{st} torsional frequency approaches the 2^{nd} and then 1^{st} bending mode as tip displacement increases.

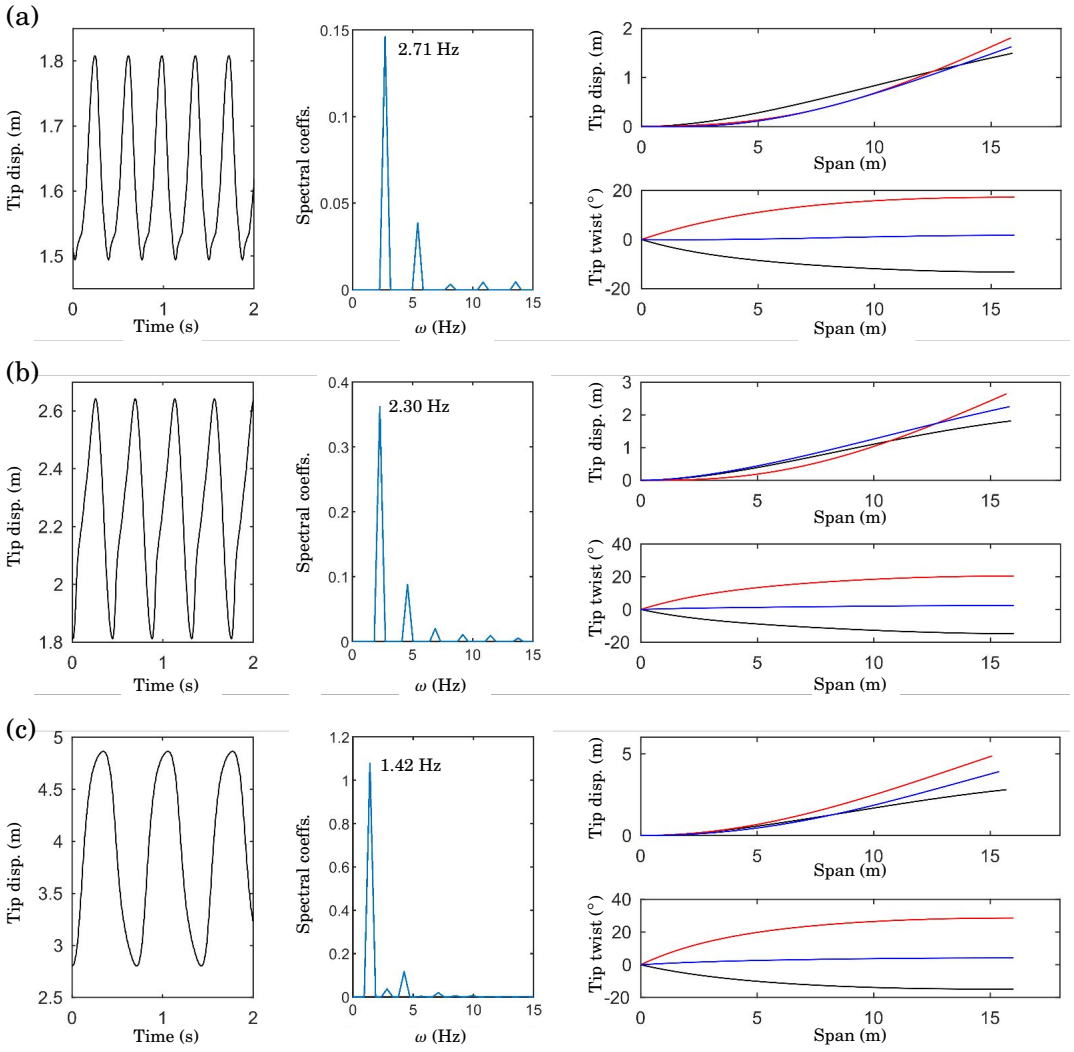

Figure 4.11: Time histories, frequencies, and spanwise deformation* for the LCOs of the HALE wing located at points (a), (b), and (c) on Fig. 4.7. *Red = max. tip deformation, black = min. tip deformation, and blue = mid. tip deformation.

4.5 Variation of stiffness

The effect of varying the stiffness of the HALE wing is now demonstrated, using two-parameter continuation (see Section 2.3.3). Re-parameterising the nominal system (4.24) to include stiffness parameters, it may be written as

$$\dot{x} = f(x, v, EI_{\text{out}}, EI_{\text{in}}, GJ), \tag{4.25}$$

where $EI_{\text{out}}, EI_{\text{in}}, GJ \in \mathbb{R}$ are the out-of-plane, in-plane bending and torsional stiffness parameters, respectively. The Hopf bifurcation shown in Fig. 4.7 is first continued with respect to both EI_{out} and airspeed, and thus the locus of v_f for varying stiffness is directly obtained; see Fig. 4.12, where one-parameter continuations of equilibria are also shown for (a) 35% and (b)

100% EI_{out}. It can be seen that neither decreasing nor increasing EI_{out} significantly affects the airspeed of the main Hopf solution branch, however an additional low-airspeed branch (c) exists within the system for stiffnesses below ~45%; these additional Hopf points are shown in inset (a).

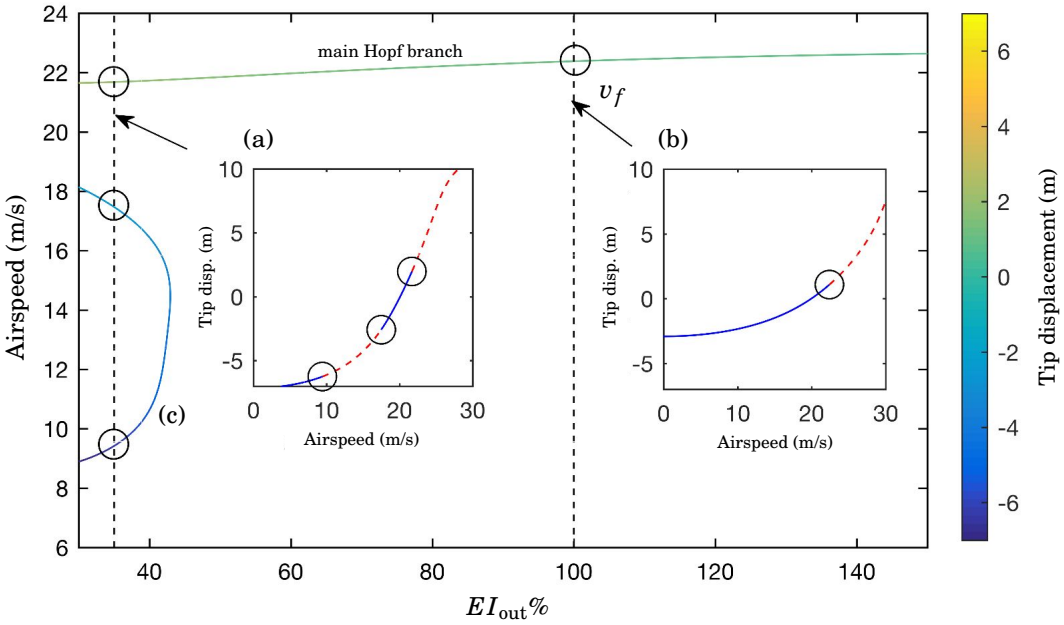

Figure 4.12: Two-parameter continuation of Hopf bifurcations, for varying out-of-plane stiffness and airspeed, for the HALE wing. One-parameter equilibria continuations are shown for (a) EI_{out} = 35% and (b) EI_{out} = 100% nominal. A low-airspeed branch exists at (c).

Figure 4.13 shows the variation of frequency and damping for EI_{out} = 35% and shows that the mode that loses stability at the higher-speed Hopf bifurcation also causes the low-speed instability. It is found that removing gravity from the system removes the low-speed phenomena, indicating that for low EI_{out}, the large downwards out-of-plane deformation (due to self-weight) enables a destabilising flutter interaction to occur at a much lower airspeed; indeed, this is evident in Fig. 4.13, which shows that the frequency of the torsion/in-plane mode is close to that of the 2$^{\text{nd}}$ bending mode at low airspeeds. This result is similar to observations made in Ref. [71], where low-speed instability regions were predicted for cases with low α_0; in such instances, deformation is similarly dominated by self-weight, but as the result of reduced aerodynamic loading. One-parameter continuation of equilibria and LCOs, at 35% EI_{out} (shown in Fig. 4.14, left), reveals that the LCOs emanating from these low-speed Hopf points are small amplitude, and disappear as airspeed increases. Continuation of the LCOs emanating from the third Hopf point (Fig. 4.14, right) reveals a very complex structure of solutions, similar to that shown in Fig. 4.7, although in this case the periodic folds are greater in quantity, and mostly occur at airspeeds below the Hopf bifurcation; the final fold at large amplitude is not plotted, but is found to occur

at 22.4 m/s. This means that, compared to the nominal wing (EI_{out} = 100%), a greater number of subcritical LCOs exist in the system; however, $\delta v/v_f$ = 0.129, which is similar.

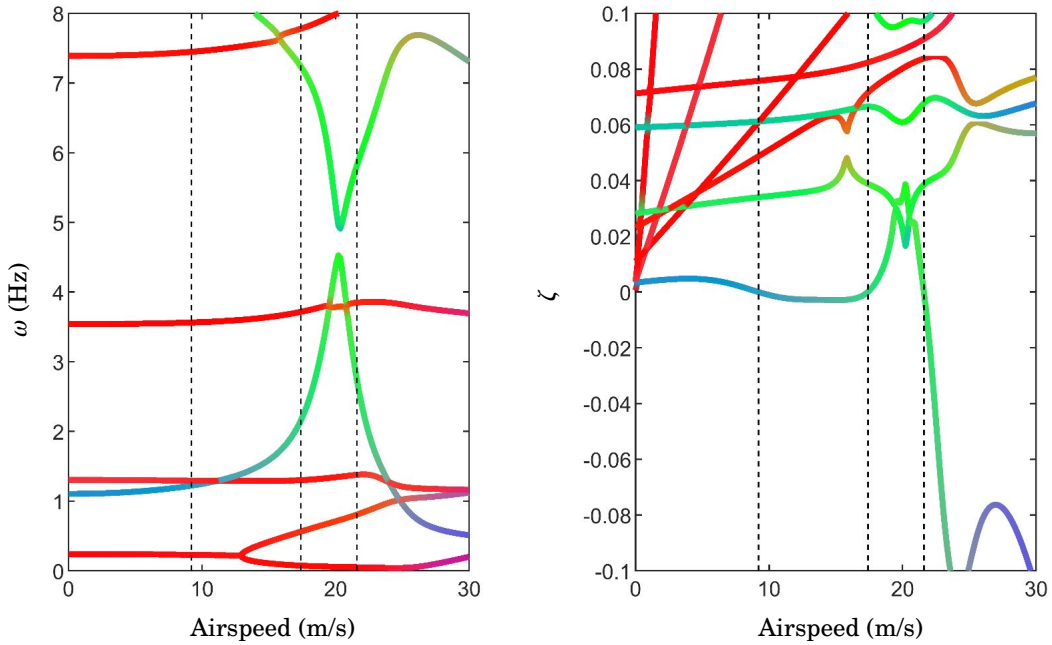

Figure 4.13: Variation of mode frequencies and damping, for varying airspeed, for HALE wing when EI_{out} = 35%. The vertical dashed lines correspond to the Hopf points shown in inset (a) in Fig. 4.12.

In addition to the continuation of Hopf bifurcations (Fig. 4.12), two-parameter continuation can also be used to obtain periodic folds. This is a very effective means of building a global picture of the system dynamics, as the variation of the complex LCO structures can be inferred from these solutions. Identifying subcritical LCOs is easily achieved by inspection, via comparison of the loci of folds and the loci of Hopf points; for any given stiffness, a subcritical LCO solution exists if a fold occurs at an airspeed lower than that of the Hopf point.

Figure 4.15 shows the continuation of the periodic folds shown in Fig. 4.7, and Fig. 4.14 (right), combined with the main Hopf bifurcation branch from Fig. 4.12. (The inset shows how the intersections on the vertical plane EI_{out} = 100% relate to the periodic folds shown in Fig. 4.7.) The shaded area between the Hopf branch and the lowest-airspeed folds illustrates the region where LCOs exist at subcritical airspeeds. It can be seen that subcritical LCOs exist at all stiffness values, although the quantity of these solutions increases greatly for lower EI_{out}. A wider range of vertical tip displacements is also achieved at lower stiffness, which is expected given that EI_{out} is reduced. Stiffening the wing can be seen to yield marginal benefit; increasing EI_{out} to ~118% achieves the smallest relative subcritical region (here, $\delta v/v_f$ = 0.096), although

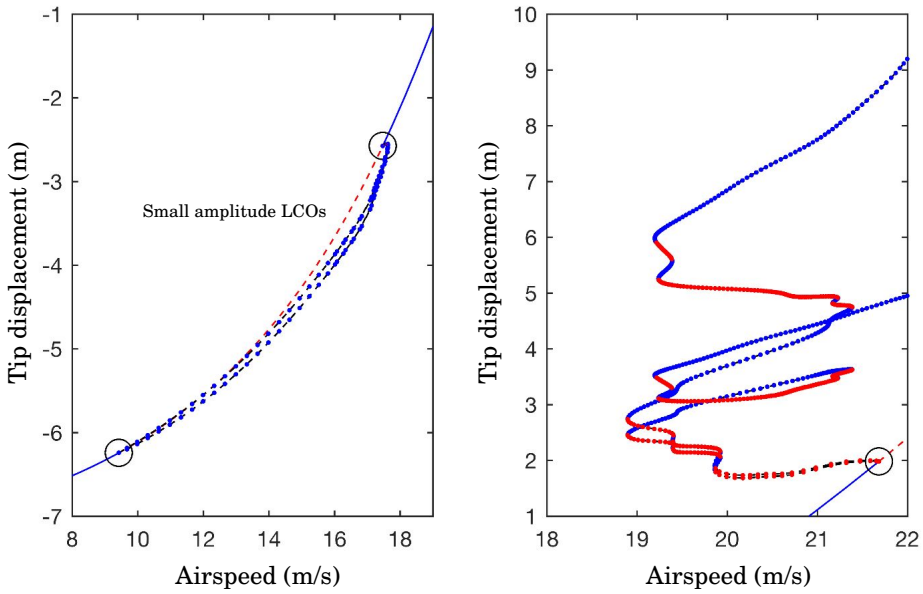

Figure 4.14: One-parameter continuation of equilibria and LCOs, for varying airspeed, for the HALE wing where EI_{out} = 35% nominal.

this is still comparable to that seen for the nominal wing. In all cases, the Hopf bifurcation is found to be subcritical.

Figure 4.16 shows the continuation of Hopf points and periodic folds for the variation of in-plane bending stiffness, EI_{in}. As with the variation of EI_{out}, the Hopf branch is marginally affected, although in this case no other solutions are found within the parameter range. The minimum value of $\delta v/v_f$, which is 0.11, is found at the upper boundary of the range; it can be seen that this ratio rapidly increases as EI_{in} reduces below ~50%. The periodic folds become generally more separated, in airspeed, as stiffness is reduced, although there is little variation in tip displacement and twist along the solutions.

Figure 4.17 shows the continuation of Hopf points and periodic folds for the variation of torsional stiffness, GJ. (Note that additional Hopf solutions are found in the system for low stiffness values, although in all instances, these occur at very large tip deflections and are therefore not shown in the figure.) From Fig. 4.17, it can be seen that varying GJ has a significant effect on the main Hopf branch; the flutter airspeed increases to 24.6 m/s (+9.9% compared to the nominal system) when GJ is increased to 150%. For decreasing stiffness, v_f steadily decreases, before reaching a critical value where the solution drops rapidly and levels out. The periodic folds become more densely concentrated, both in airspeed and tip displacement, although some twist values become very high. For GJ values between ~32% and ~52%, all LCOs exist at airspeeds greater than the Hopf bifurcation, which itself is found to be supercritical at stiffnesses below ~54%; this change of Hopf criticality is indicated by the emergence of a new branch of fold solutions at point (a) (this will be further discussed in Section 4.7). When stiffness increases, a

number of subcritical LCOs disappear from the system, although the remaining solutions follow a trend similar to that of the Hopf branch. There is a single subcritical LCO for values of GJ above ~105%.

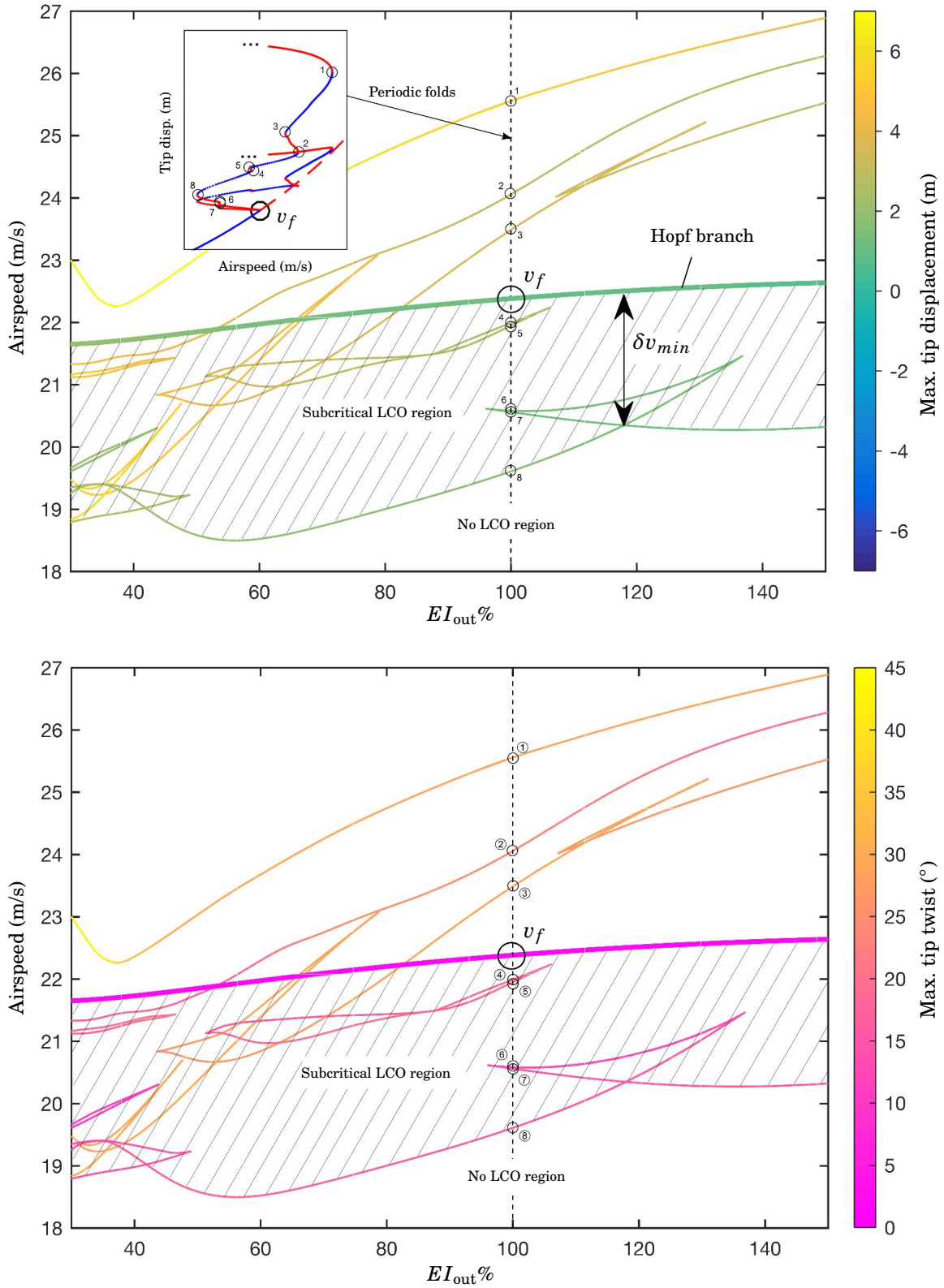

Figure 4.15: Two-parameter continuation of Hopf points and periodic folds, for varying airspeed and out-of-plane stiffness, for the HALE wing.

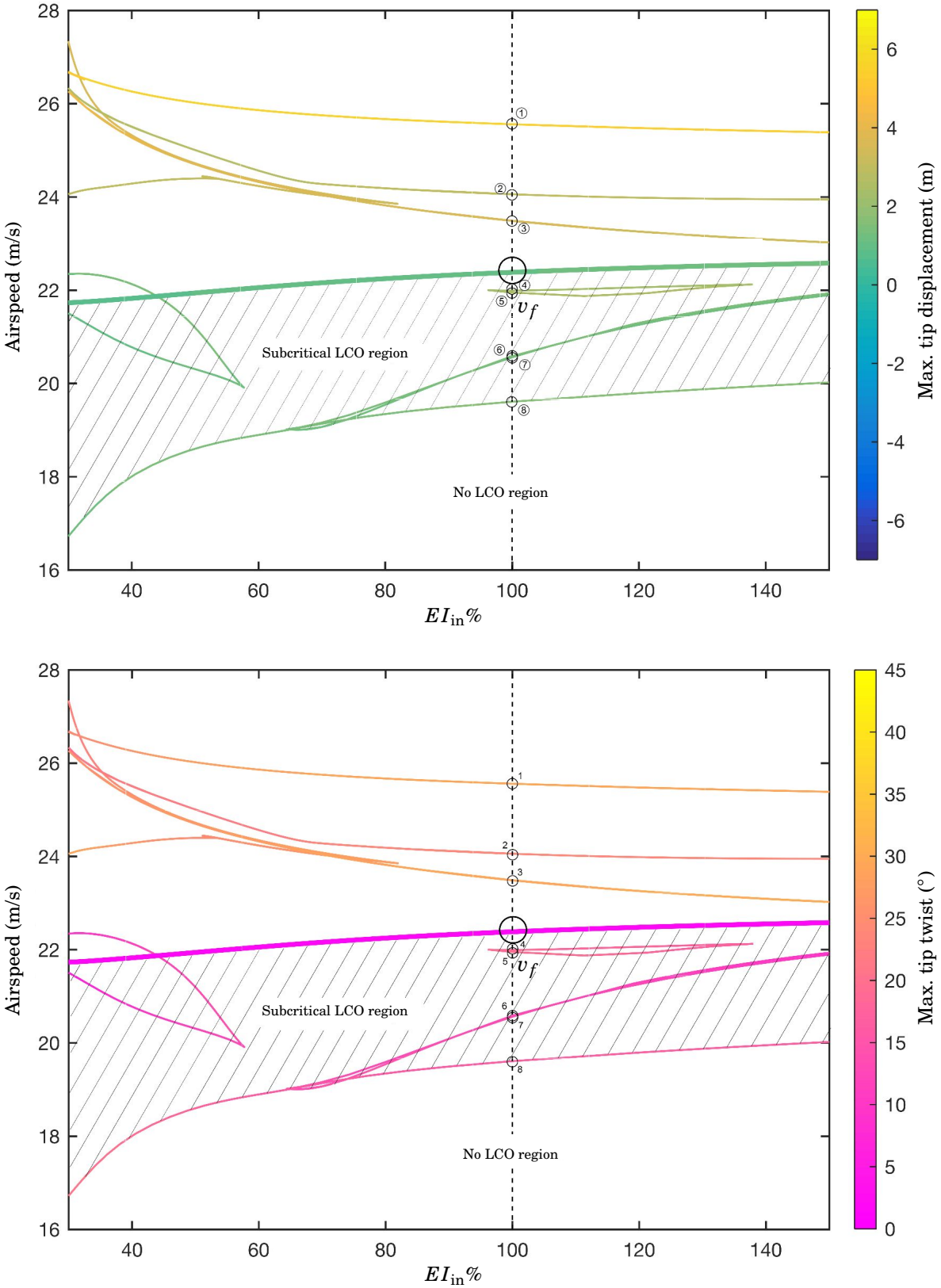

Figure 4.16: Two-parameter continuation of Hopf points and periodic folds, for varying airspeed and in-plane stiffness, for the HALE wing.

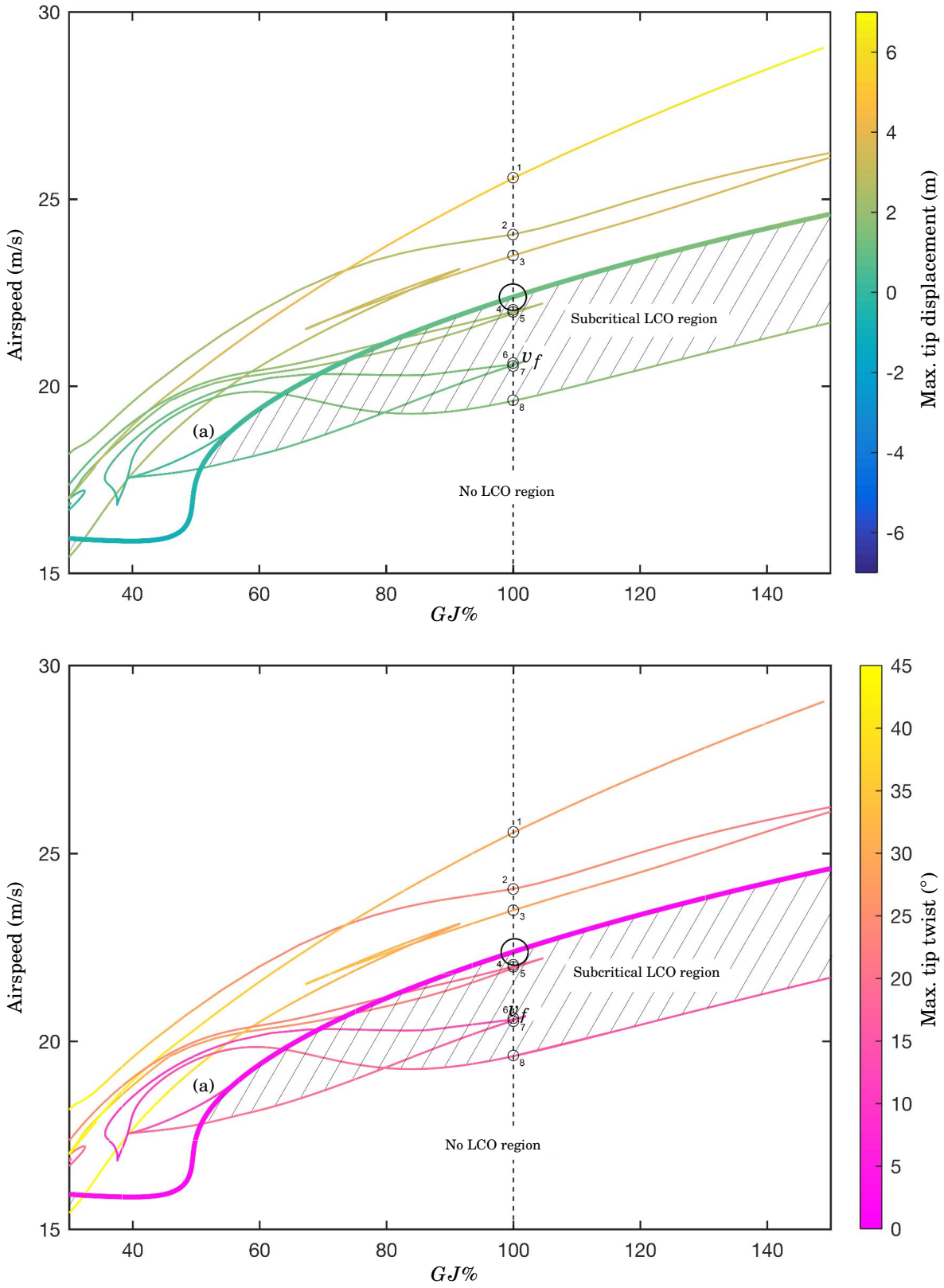

Figure 4.17: Two-parameter continuation of Hopf points and periodic folds, for varying airspeed and torsional stiffness, for the HALE wing.

4.6 Variation of stiffness coupling

A stiffness coupling factor, K^*, is now applied between EI_{out} and GJ. This factor is implemented in the off-diagonal elements of the 3×3 stiffness matrix of the 1D beam, and is expressed as a % of the nominal value of EI_{out} shown in Table 4.1. The use of such a term is intended to approximate aeroelastic tailoring techniques that involve the use of directional stiffness properties to provide performance benefit (e.g. gust loads alleviation or flutter suppression; e.g. Ref. [25]). Re-parameterising the nominal system (4.24) to include this factor, it may be expressed as

$$\dot{x} = f(x, v, K^*) \tag{4.26}$$

where $K^* \in \mathbb{R}$ is the stiffness coupling parameter, implemented as

$$\overline{K} = \begin{pmatrix} EI_{\text{out}} & K^* & 0 \\ K^* & GJ & 0 \\ 0 & 0 & EI_{\text{in}} \end{pmatrix}. \tag{4.27}$$

Figure 4.18 shows the continuation of Hopf points and periodic folds, for varying airspeed and K^*, where $K^* = 0$ is the nominal wing. In this study, $K^* > 0$ corresponds to the case where GJ *increases* with out-of-plane deformation, providing a 'wash-out' effect. Negative values of K^* are not investigated, as these would (detrimentally) increase the twisting of the wing. It can be seen, from Fig. 4.18, that the Hopf branch increases in airspeed as coupling increases; for example, at 30% the flutter airspeed has increased to 26.19 m/s. Subcritical LCOs exist in the system for all values, however the region between the lowest-airspeed folds and the Hopf points decreases significantly. At 30%, a single subcritical LCO exists, and the subcritical region is reduced (here, $\delta v/v_f = 0.037$).

Periodic folds occurring beyond the flutter airspeed are seen to rapidly increase in airspeed when coupling is increased. Use of one-parameter continuation shows that the overall LCO solution structure undergoes a significant topological change between 10% and 15%; see Fig. 4.19. During this parameter interval, the LCO solution re-attaches to the equilibrium solution, via a second Hopf bifurcation, before a third Hopf point subsequently occurs.

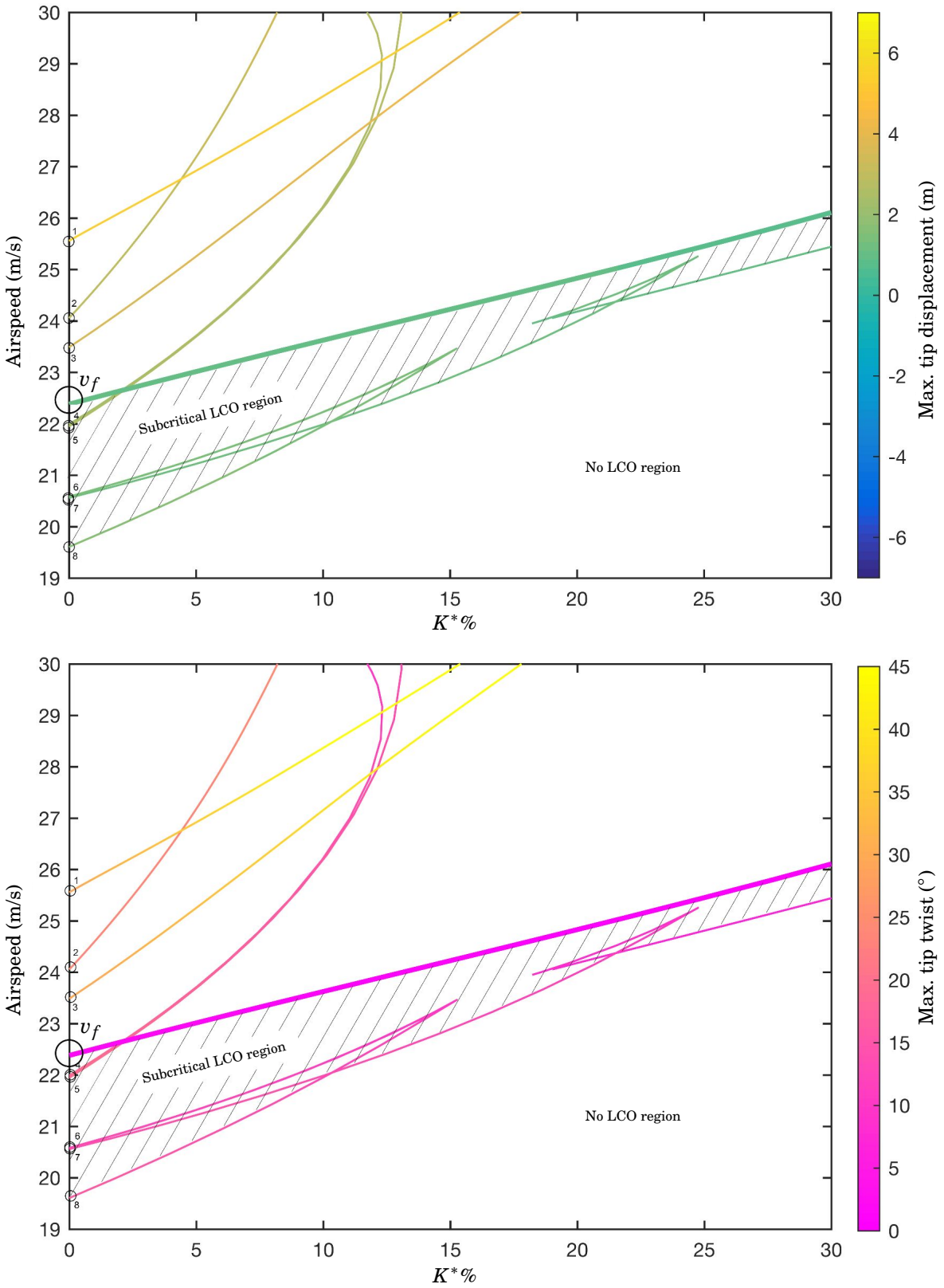

Figure 4.18: Two-parameter continuation of Hopf points and periodic folds, for varying airspeed and stiffness coupling, for the HALE wing.

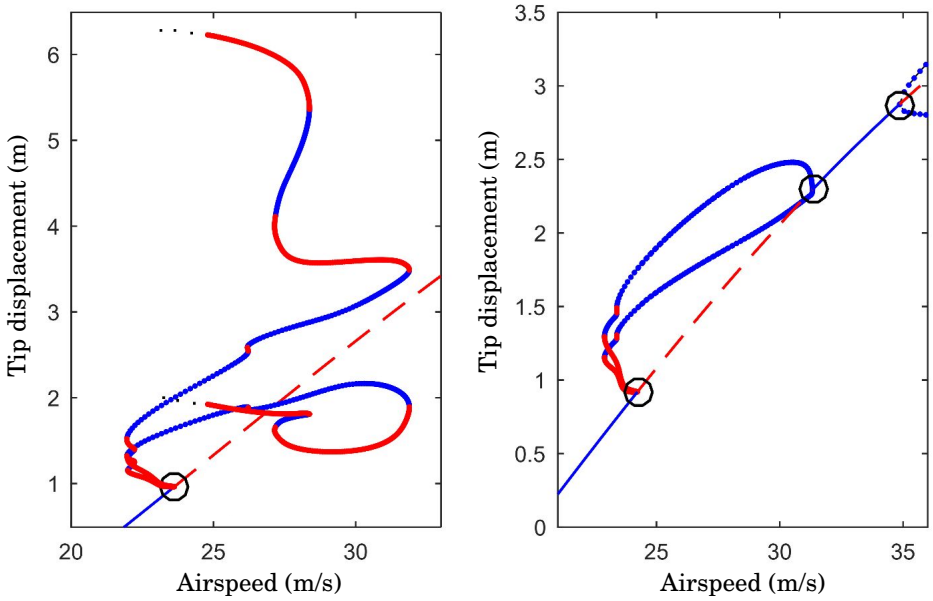

Figure 4.19: One-parameter continuation of equilibria and LCOs, for varying airspeed, for the HALE wing when $K^* = 10\%$ (left) and 15% (right).

4.7 Hopf bifurcation criticality

It was shown in Fig. 4.7 that, in the present work, the flutter point of the nominal HALE wing is a subcritical Hopf bifurcation. It will be shown in this section that, as was observed with the 2 DoF flutter wing in Chapter 3, Hopf criticality in the HALE wing can be changed by varying damping and stiffness parameters; moreover, as was found in Section 3.3, these changes similarly coincide with changes to the modes of the linearised system at flutter. Given the size of the dynamical system used to model the HALE wing, the quantity l_1 (see Section 3.2) is not rapidly computable; instead, Hopf criticality is obtained by inspecting the one-parameter continuation of LCO solutions emanating from the bifurcation point.

First, the structural damping of the wing is varied. It was shown in Section 3.3.1 that the variation of structural damping effectively allows a flutter point to be placed at an airspeed where the modes of the linearised system are different. The nominal damping factor[2] applied to the HALE wing is d = 1e-3; Fig. 4.20 compares the LCO solutions of the nominal wing to the cases where d is increased to 5.5e-3 and 20e-3, respectively. When d = 5.5e-3, the Hopf is close to the degenerate case, whereas when d = 20e-3, the Hopf is supercritical; thus, the criticality has changed with increased damping. The modes for d = 5.5e-3 and d = 20e-3 are shown in Figs. 4.21 & 4.22, respectively; the degenerate Hopf occurs when the in-plane/torsion (i.e. flutter) mode and the 2$^{\text{nd}}$ bending mode have similar frequency, whereas the supercritical Hopf occurs when the in-plane/torsion mode has lower frequency than the 2$^{\text{nd}}$ bending mode. Recall that in the nominal case (subcritical Hopf) shown in Fig. 4.8, the in-plane/torsion frequency was greater than the 2$^{\text{nd}}$ bending frequency at flutter.

The variation of the out-of-plane and in-plane bending stiffnesses is also found to change Hopf criticality; the necessary variations are found to exceed the stiffness ranges previously explored in Figs. 4.15 & 4.16. The one-parameter continuation of LCOs for *increasing* EI_{out} and *decreasing* EI_{in} are shown in Figs. 4.23 & 4.24, respectively; the Hopf is supercritical at EI_{out} = 310% and EI_{in} = 10%, and (approximate) degenerate Hopfs are found at EI_{out} = 308% and EI_{in} = 13.6%.

Figures 4.25 & 4.26 show the modes for EI_{out} = 308% and EI_{out} = 310% and show that, compared to the nominal wing (Fig. 4.8), all modes with large out-of-plane component have increased in frequency. Similarly to the damping observations, the degenerate Hopf occurs when the in-plane/torsion and 2$^{\text{nd}}$ bending modes have similar frequency at flutter, and the supercritical Hopf occurs when the in-plane/torsion mode is below the 2$^{\text{nd}}$ bending mode at flutter. The modes for EI_{in} = 13.6% and EI_{in} = 10% are shown in Figs. 4.27 & 4.28 and show that, while the supercritical Hopf is similarly caused by the reordering of the in-plane/torsion and 2$^{\text{nd}}$ bending modes, the degenerate case is less precisely aligned to the when the two frequencies are similar.

With regards to the torsional stiffness, the two-parameter continuation of Hopf and periodic fold bifurcations in Fig. 4.17 already revealed a new branch of folds at point (a), and thus a change in Hopf criticality, when GJ is reduced below ~53%. Fig. 4.29 shows the one-parameter of

[2]The total structural damping is given by d multiplied by the stiffness distribution; see Section 4.2.

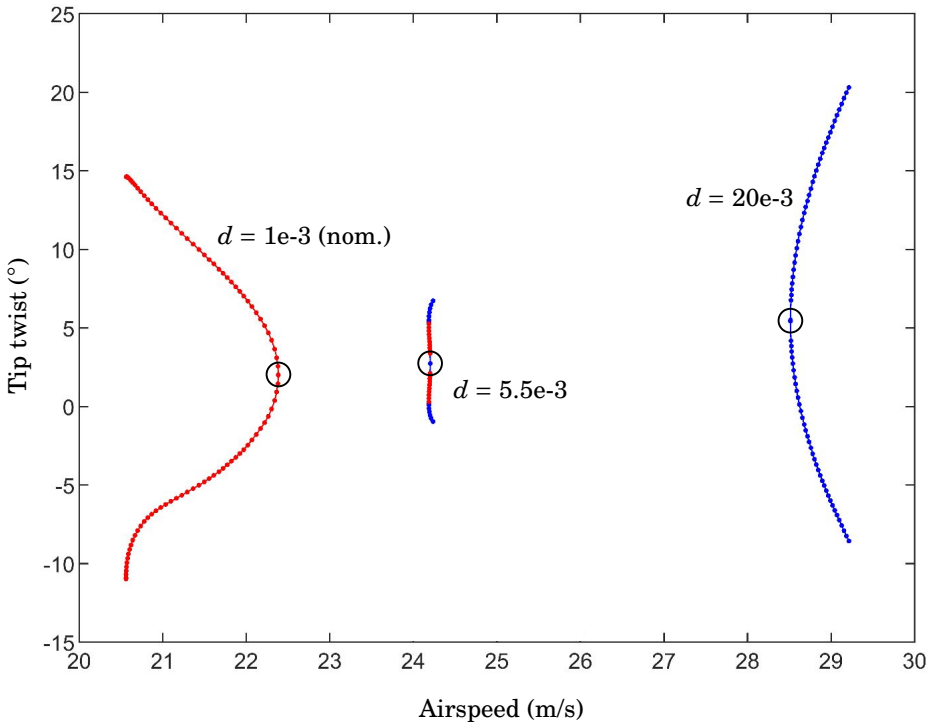

Figure 4.20: One-parameter continuation of LCO solutions, for varying airspeed, for HALE wing when d = 1e-3, 5.5e-3 and 20e-3.

LCOs for $GJ = 53\%$ and $GJ = 40\%$ and shows that the Hopf is close to the degenerate case at 53% and strongly supercritical at 40%.

Figures 4.30 & 4.31 show the modes for $GJ = 53\%$ and $GJ = 40\%$ and show that, unlike the previous examples, the change of Hopf criticality does not coincide with the reordering of the torsion/in-plane and 2^{nd} bending mode frequencies. The physical justification of this difference can be explained as follows. As was noted in Section 4.3, equilibria solutions of the HALE wing non-trivial and so contain structural nonlinearity; therefore, since the wing is statically deforming with airspeed, the variation of equilibria frequencies with *airspeed* contains information of how the structural frequencies vary with *deformation*. Essentially, in Figs. 4.30 & 4.31, the *gradient* of the frequencies with respect to airspeed may provide indication of how the frequencies vary when the wing deforms about the equilibrium condition. Thus, should there be a change in the sign of the frequency gradient at flutter, this could coincide with a change in Hopf criticality. In the nominal HALE wing, which exhibited a subcritical Hopf, the gradient of the in-plane/torsion mode at flutter is negative (see Fig. 4.8); Fig. 4.30 shows that for the supercritical Hopf at $GJ = 40\%$, the gradient of the torsion/in-plane mode has become positive. Moreover, Fig. 4.31 shows that the approximate degenerate Hopf at $GJ = 53\%$ coincides with when the torsion/in-plane frequency gradient is approximately zero.

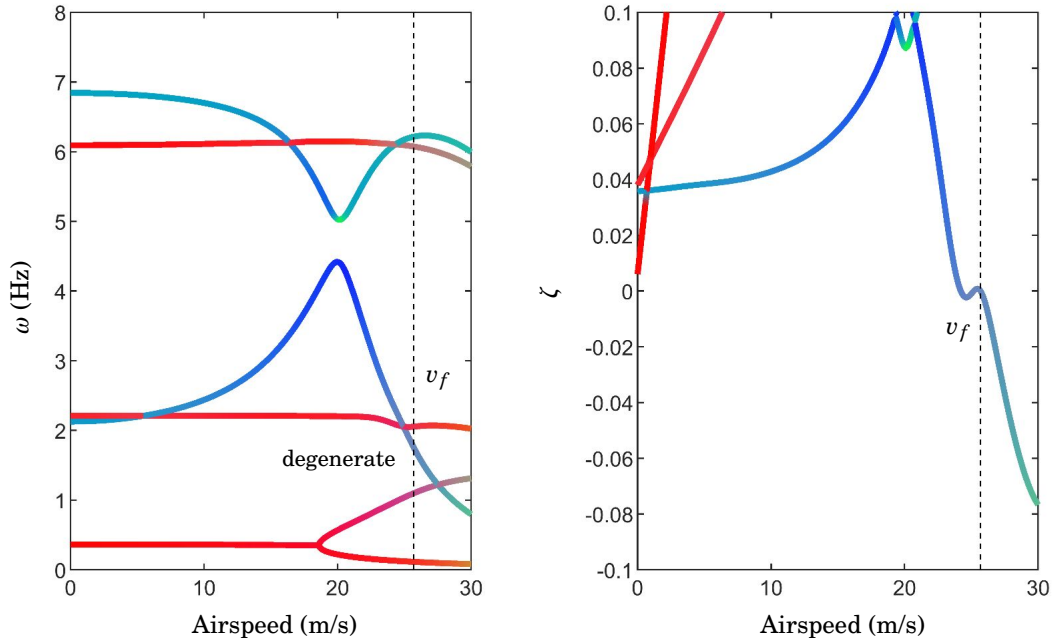

Figure 4.21: Variation of mode frequencies and damping, for varying airspeed, for HALE wing when d = 5.5e-3.

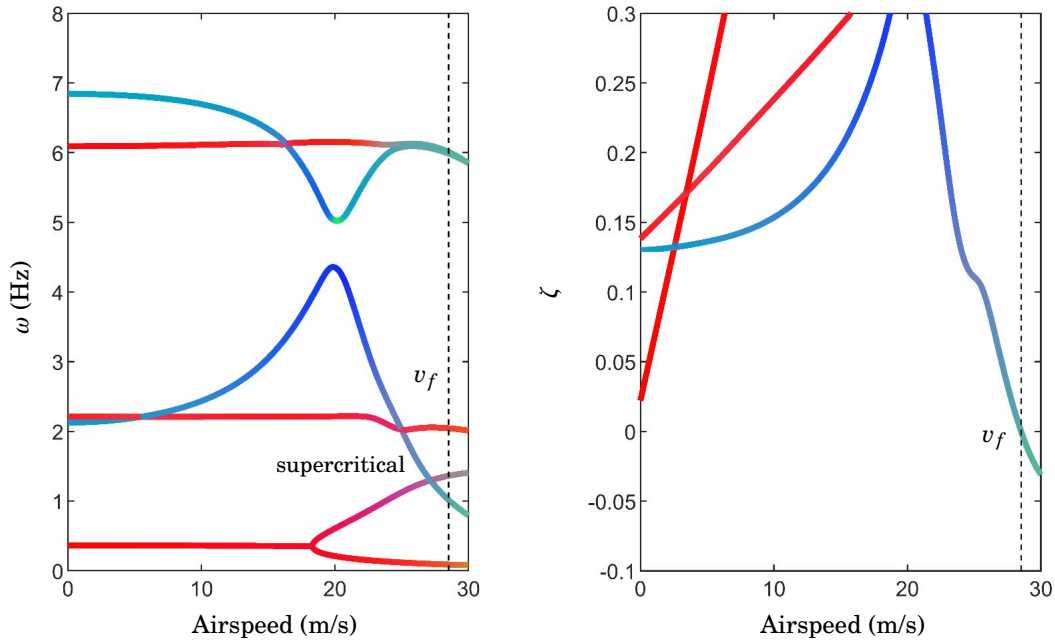

Figure 4.22: Variation of mode frequencies and damping, for varying airspeed, for HALE wing when d = 20e-3.

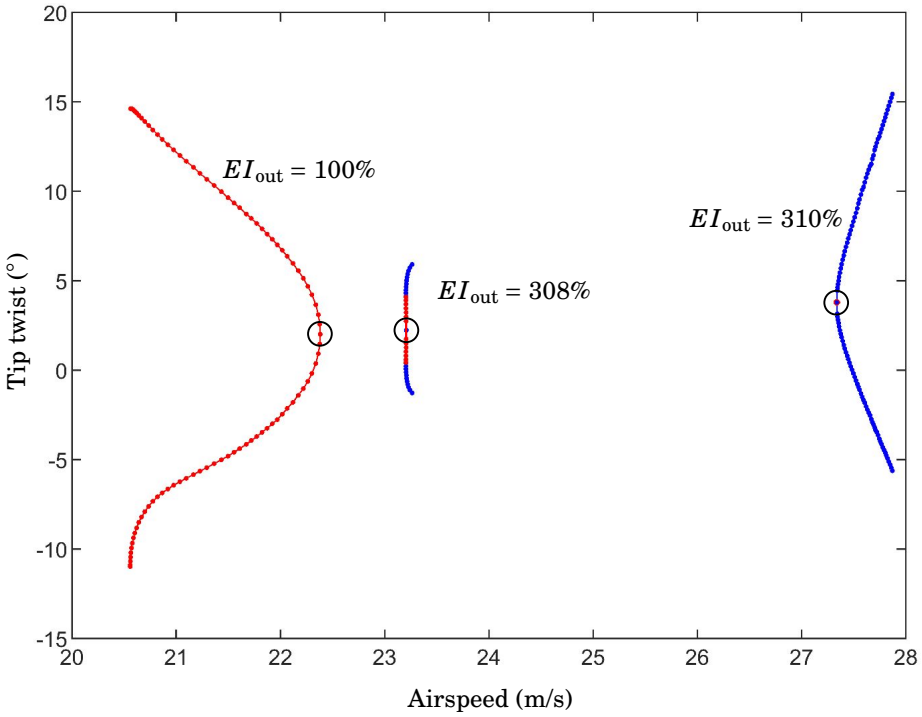

Figure 4.23: One-parameter continuation of LCO solutions, for varying airspeed, for HALE wing when EI_{out} = 100%, 300% and 310%.

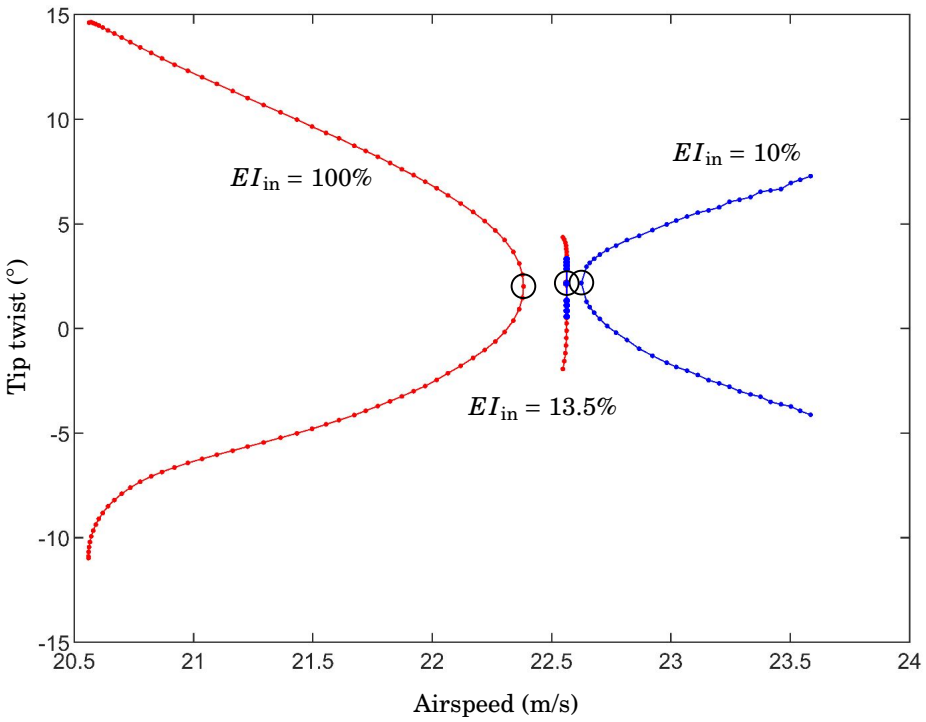

Figure 4.24: One-parameter continuation of LCO solutions, for varying airspeed, for HALE wing when EI_{in} = 100%, 13.5% and 10%.

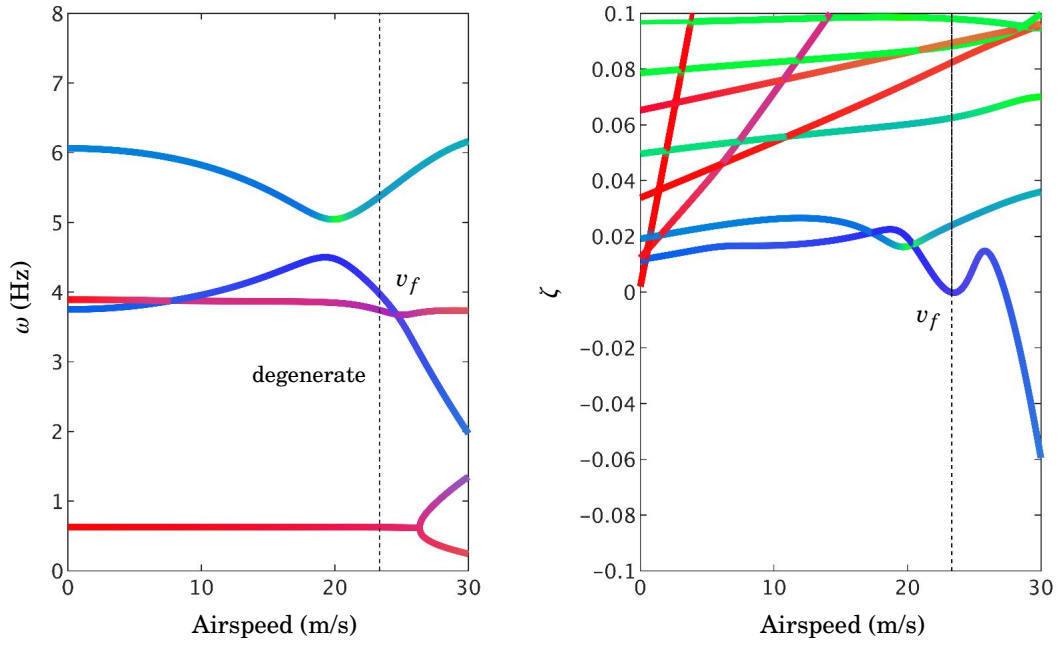

Figure 4.25: Variation of mode frequencies and damping, for varying airspeed, for HALE wing when $EI_{\text{out}} = 308\%$.

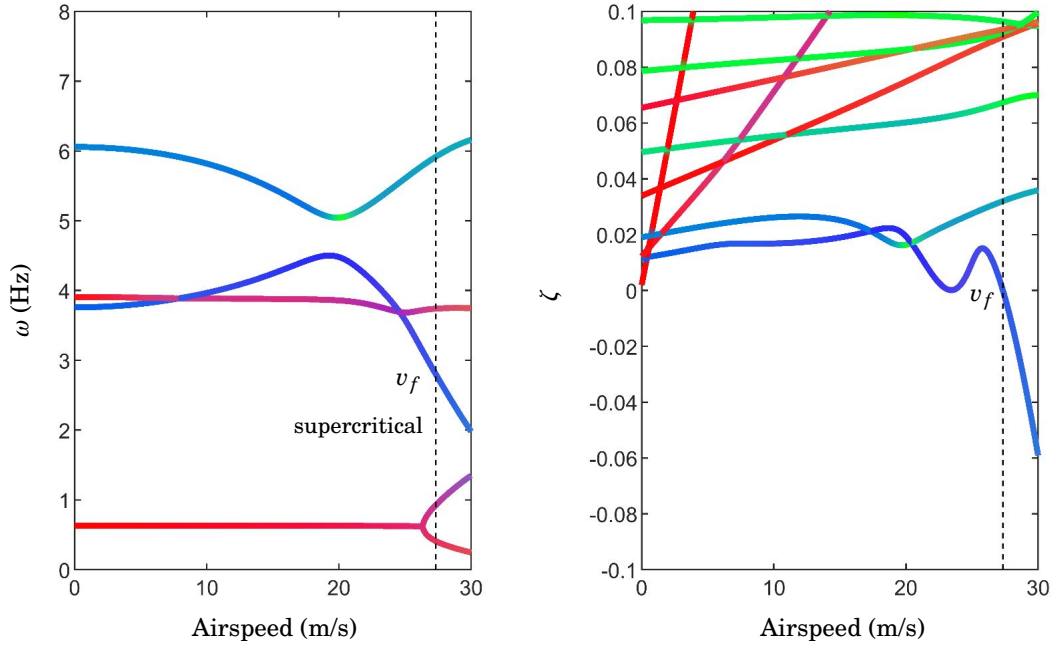

Figure 4.26: Variation of mode frequencies and damping, for varying airspeed, for HALE wing when $EI_{\text{out}} = 310\%$.

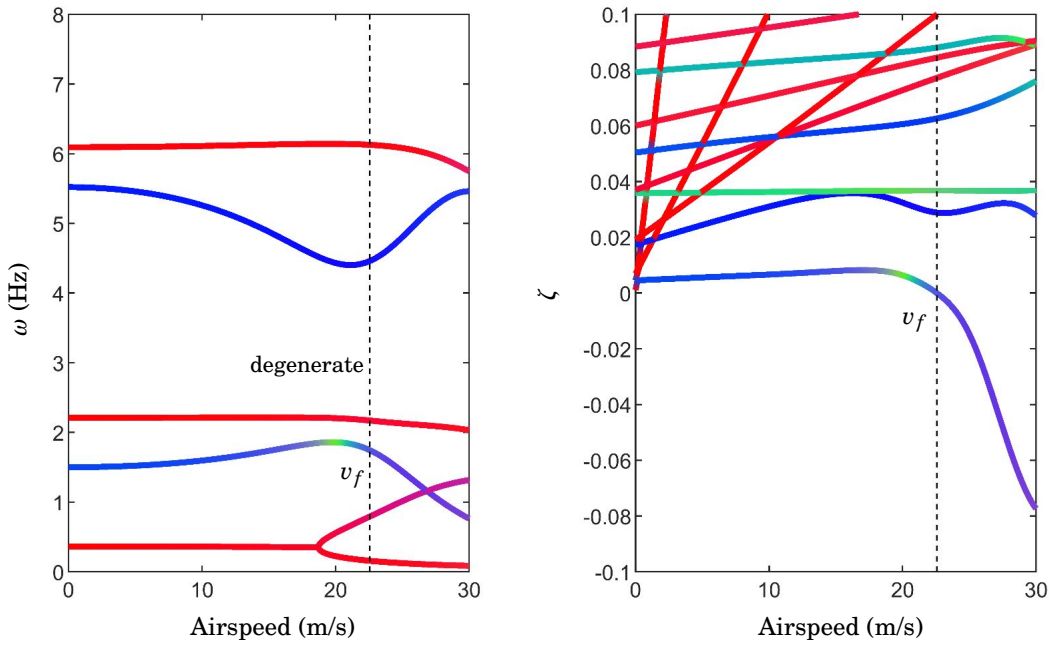

Figure 4.27: Variation of mode frequencies, for varying airspeed, for HALE wing when $EI_{\text{in}} = 13.6\%$.

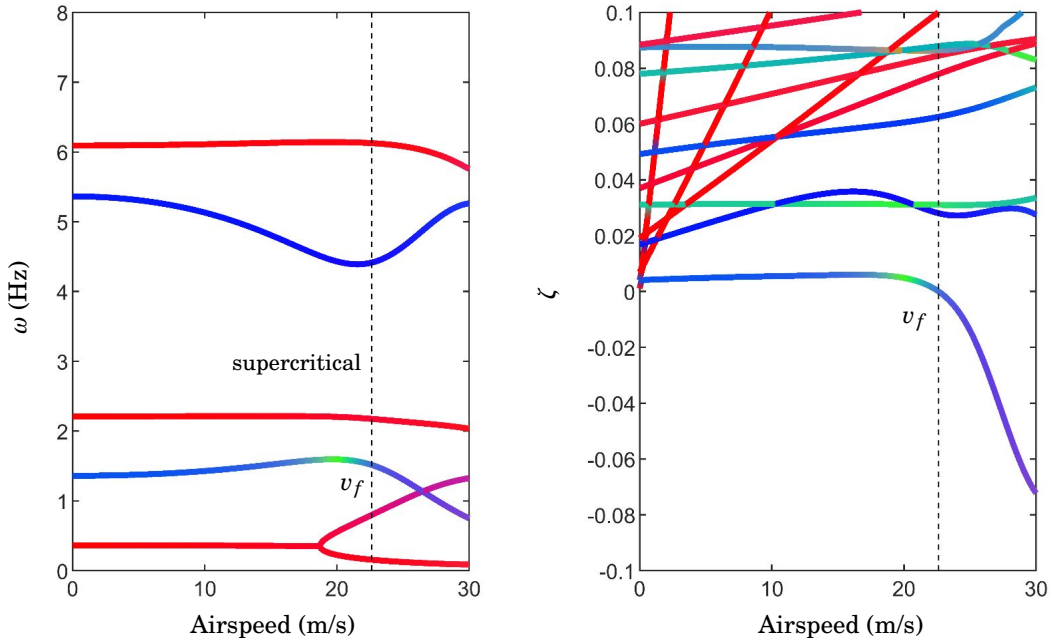

Figure 4.28: Variation of mode frequencies and damping, for varying airspeed, for HALE wing when $EI_{\text{in}} = 10\%$.

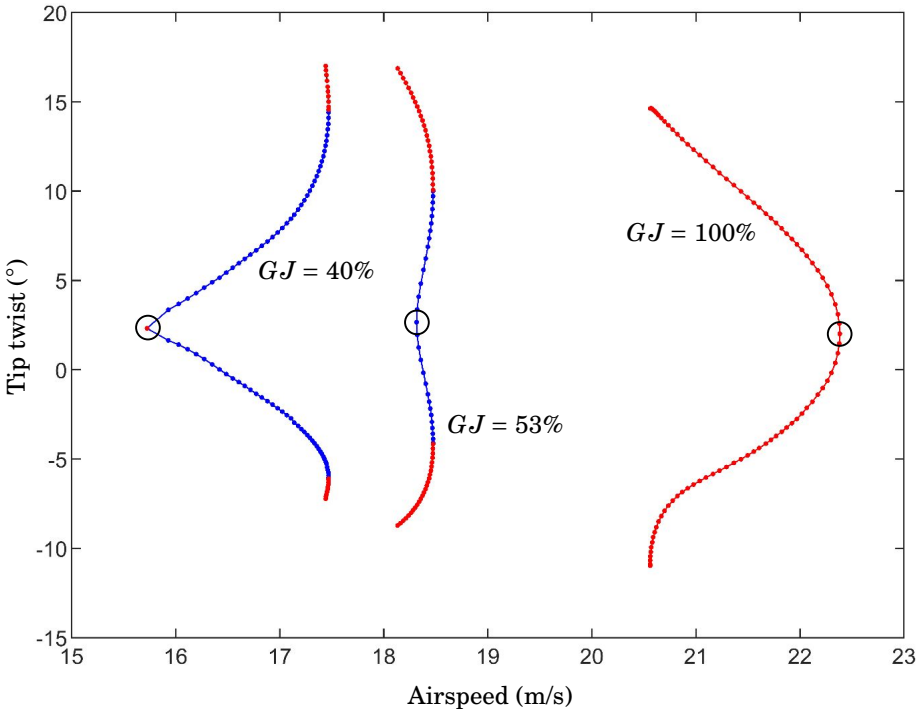

Figure 4.29: One-parameter continuation of LCO solutions, for varying airspeed, for HALE wing when GJ = 50%, 53% and 100%.

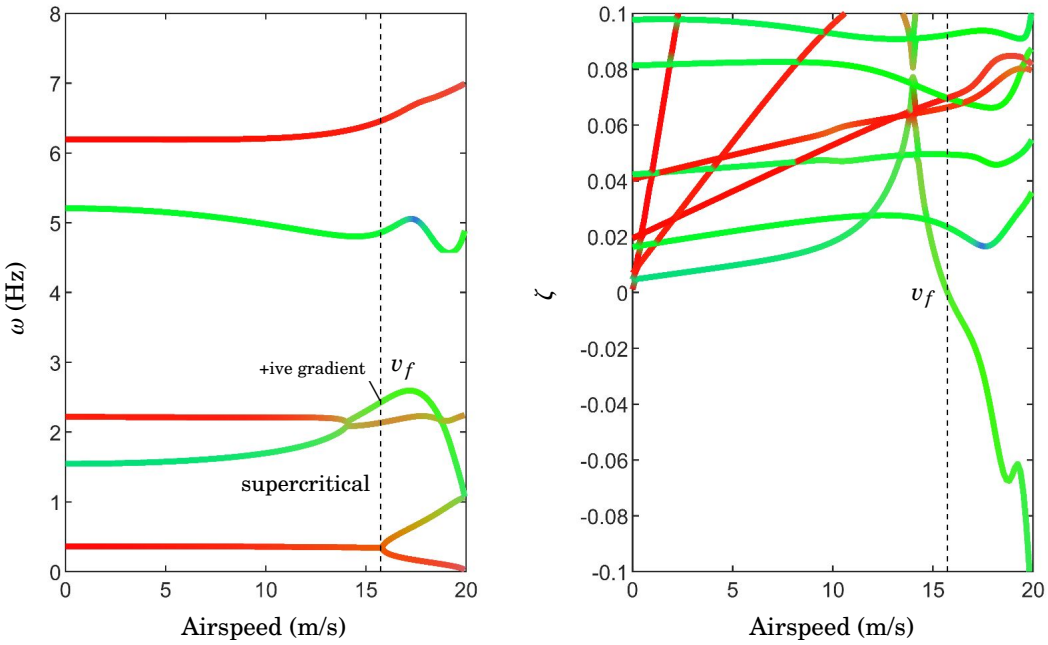

Figure 4.30: Variation of mode frequencies and damping, for varying airspeed, for HALE wing when GJ = 40%.

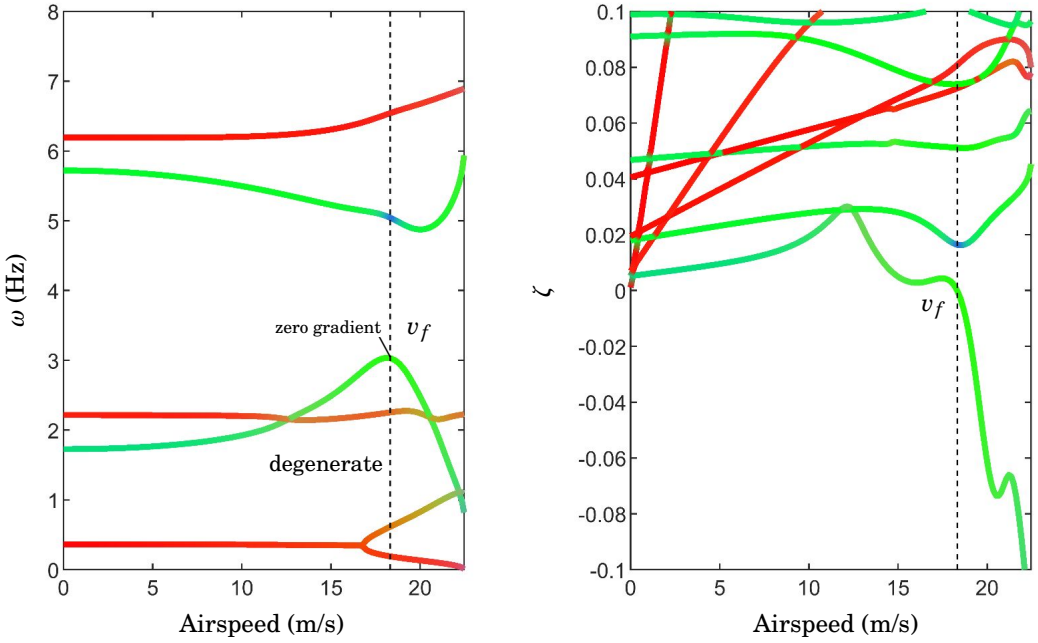

Figure 4.31: Variation of mode frequencies and damping, for varying airspeed, for HALE wing when $GJ = 53\%$.

4.8 Conclusions

This chapter has demonstrated the use of numerical continuation for obtaining the complex nonlinear aeroelastic dynamics of a flexible, high-aspect-ratio wing. A reduced-order nonlinear beam model was used with linear, quasi-steady aerodynamics, and one-parameter continuation showed that subcritical limit cycle oscillations (LCOs), which are detrimental solutions existing at airspeeds below the nonlinear flutter airspeed, exist due to geometric nonlinearity. The two-parameter continuation of Hopf and periodic fold bifurcations revealed the sensitivity of the nominal dynamics to variations in out-of-plane, in-plane and torsional stiffness, and a 'wash out' stiffness coupling parameter. By the inspection of these complex bifurcation diagrams, regions in parameter space where subcritical LCOs exist were easily identified, and it was shown that such phenomena are present for a wide range of stiffness values. Indeed, the only instance where subcritical LCOs did not exist is when torsional stiffness is reduced to 52% of the nominal value. Following on from the discussions in Chapter 3, the criticality of the Hopf bifurcation in the HALE wing was found to be affected by the variation of structural damping and stiffness; these changes were similarly related to the modes of the linearised system at the flutter airspeed.

Given the results in this chapter, it is clear that the geometric nonlinearity inherent in flexible, high-aspect-ratio wings can be a fundamental driver of complex phenomena, without the need for aerodynamic nonlinearity. Overall, this chapter has shown that the effects of geometric nonlinearity must be adequately captured in the analysis of high-aspect-ratio wings if undesirable dynamical phenomena (e.g. subcritical LCOs) are to be mitigated by design. Moreover, it has shown that numerical continuation techniques are applicable to this type of analysis.

CHAPTER 5

NONLINEAR AEROELASTIC DYNAMICS OF AN AIRCRAFT

This chapter examines the nonlinear dynamics of an aircraft with flexible, high-aspect-ratio wings. Trim solutions are obtained for varying airspeed and are compared to those for the equivalent rigid aircraft. One-parameter continuation is used to obtain the nonlinear dynamics of the flexible case, and it is revealed that periodic fold bifurcations, which occur after a supercritical Hopf bifurcation, have a detrimental effect on the behaviour. Variation of torsional stiffness is shown to remove these phenomena.

5.1 Introduction

So far, the nonlinear dynamics investigated in this thesis have solely pertained to flexible, high-aspect-ratio wings with fixed root conditions. As has been demonstrated, highly complex dynamical phenomena can exist in such systems, due to the geometric nonlinearity inherent in large deformations, without the need for aerodynamic stall. In this chapter, the focus turns to the nonlinear dynamics of a full aircraft that features high-aspect-ratio wings. The behaviour of this system comprises the combined effects of: i) aeroelastic phenomena, which are the result of flexible modes and large wing deformations, and ii) the rigid-body motion of the aircraft. In this study, one-parameter numerical continuation is used to obtain equilibrium solutions and sustained periodic motions, i.e. limit cycle oscillations (LCOs), of the aircraft for increasing airspeed. While the Hopf bifurcation occurring at the flutter point is found to be supercritical (i.e. the desirable outcome when compared to the subcritical case, see Fig. 2.6), it is shown that detrimental nonlinear phenomena nevertheless exist in the system, due to the existence of periodic fold bifurcations.

The complete flight dynamics of any aircraft are inherently nonlinear, regardless of whether the airframe is flexible or not. The fundamental equations of rigid-body motion (as found in

many textbooks, for example Refs. [48] & [95]) reveal that nonlinearity exists due to kinematic coupling (e.g. between angle of attack and sideslip), gyroscopic effects (involving angular rates of change) and gravitational effects. For a given aircraft, the typical approach comprises obtaining a *trim solution*, i.e. a steady flight condition where all forces and moments are balanced, about which the nonlinear dynamical system (with fixed parameters) is linearised. The stability of this linearised system, to small perturbations in state, is then obtainable from eigenanalysis; classical responses are characterised as *longitudinal* modes (variations in heave and pitch, i.e. the phugoid or short-period), or *lateral-directional* modes (variations in roll, yaw and sideslip, such as the Dutch roll or spiral divergence). Provided that the trimmed aircraft is symmetric about the fuselage, longitudinal dynamics are easily uncoupled and examined in isolation. However, as with any linearisation approach, behaviours away from the equilibrium (or in this case, the trim solution) are not captured and the complete dynamics are only obtainable using nonlinear methods. Consequently, the study of rigid-body aircraft behaviour has been a key area in which nonlinear tools have been exploited; this is particularly true in the analysis of fighter aircraft, where numerical continuation has successfully been used for determining of critical flight regimes (e.g. Refs. [96, 97, 47, 98]). More recently, the techniques have been used for the study of airliner loss-of-control (i.e. upset) dynamics [99].

The impact of nonlinear aeroelastic phenomena on the flight dynamics of aircraft has been of increasing interest in recent decades. This is mainly due to the increased interest in high altitude, long endurance (HALE) vehicles, which are flexible configurations designed for the provision of scientific data and military reconnaissance [100] (see Section 2.4). A variety of low-order frameworks have been developed to enable the aeroelastic modelling of such aircraft, as shown in Refs. [101, 71, 102–106, 67, 107, 108]; such studies invariably adopt the typical approach described above, i.e. solving for a nonlinear equilibrium (i.e. deformed trim condition) and performing linear stability analysis, sometimes with numerical integration (i.e. time-stepping). Patil *et al.* [71] showed that, compared to a rigid HALE case, the presence of large wing flexibility can lead to greater trim angles of attack and the short-period mode becoming non-oscillatory at certain airspeeds. The phenomenon called 'body-freedom flutter', i.e. the oscillatory instability caused by a critical interaction between flexible and rigid-body modes, has been the focus of several studies [109–111]; such behaviour is particularly problematic for flying wing configurations, as these aircraft have a high short-period frequencies, due to low pitch inertia, making interactions with flexible bending modes more likely. Fuselage-tail configurations are less susceptible to this type of instability, by virtue of the inertia and damping provided by the tail.

In the present study, the longitudinal nonlinear dynamics of the HALE aircraft (first introduced in Ref. [71] and shown in Fig. 2.9) are investigated using numerical continuation. This aircraft consists of highly flexible wings (which are implemented identically to the wing examined in Chapter 4), a rigid horizontal tailplane and a point-mass payload. Fig. 5.1 shows the deformed aircraft, in a steady trim condition, in the global inertial frame; note that Z is positive upwards in

this instance. The force and moment balances required for trim solutions are obtained by varying i) the angle of incidence of the tailplane, and ii) the magnitude of a horizontal thrust vector, which acts through the centre of gravity (CG) of the aircraft. In Section 5.2, the general form of the aeroelastic system is described, extending the formulation from Section 4.2. Section 5.3 provides an overview of the aircraft parameters, mostly derived from Ref. [71], that describe the nominal (i.e. flexible) configuration. Section 5.4 compares the trim solutions of this system, obtained at varying airspeeds, to the equivalent rigid configuration, i.e. where stiffness is sufficiently high such that the wings do not deform. In Section 5.5, the trim solutions for the flexible aircraft are combined with one-parameter numerical continuation to obtain the equilibria and LCOs. In Section 5.6, the torsional stiffness of the wing is varied. Upset dynamics, which describe uncontrolled aircraft behaviours away from a trim condition, are not investigated.

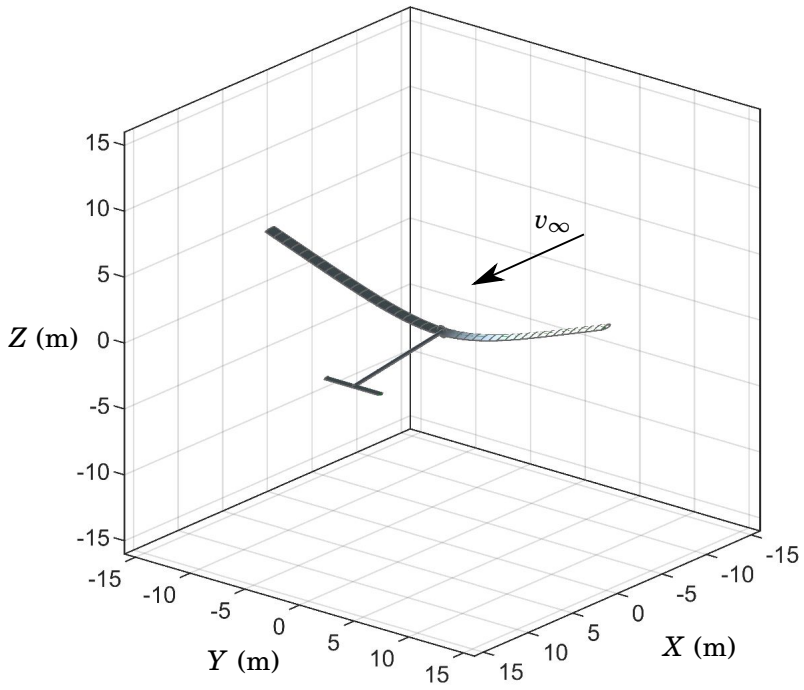

Figure 5.1: Visualisation of the HALE aircraft in a global inertial frame.

As with the vast majority of the work in this thesis, the aeroelastic formulation used is based the theory of Howcroft *et al.* [6] (see Section 4.2). This is a very low-order, geometrically exact method that describes the spanwise kinematic quantities of a flexible beam using a series of shape functions. The aerodynamics are modelled using linear, quasi-steady strip theory; consequently, quantitative comparison with the aeroelastic results in Ref. [71], which were obtained using the aerodynamic model of Peters *et al.* [93, 94], is not targeted. (Note that a comparison of the structural frequencies of the deformed wing was previously shown in Fig. 4.4.) A comparison of the rigid aircraft modes can be made, however; this will be discussed in Section 5.4.

5.2 Aeroelastic formulation

The aeroelastic formulation used in this chapter is an extension to the theory previously described in Chapter 4. In the present study, the general flexible beam formulation from Section 4.2 is appended with six rigid-body coordinates to describe 'free-free' translational and rotational dynamics. The generalised coordinates are

$$\underline{q} = \begin{pmatrix} q_{\mathrm{f}} \\ q_{\mathrm{T}} \\ q_{\mathrm{R}} \end{pmatrix}, \qquad \text{where} \quad q_{\mathrm{T}} = \begin{pmatrix} X \\ Y \\ Z \end{pmatrix}, \quad q_{\mathrm{T}} = \begin{pmatrix} \alpha \\ \beta \\ \phi \end{pmatrix}, \tag{5.1}$$

where q_{f} comprises the coordinates that describe flexible wing deformation (see Section 4.2) and q_{T} and q_{R} define the global position and rotation vectors of the aircraft, respectively. The rigid-body derivative $\dot{q}_{\mathrm{R}}$ is expressed as

$$\dot{q}_{\mathrm{R}} = \begin{pmatrix} \dot{\alpha} \\ \dot{\beta} \\ \dot{\phi} \end{pmatrix} = \mathfrak{T}_{\mathrm{tan.}}(q_{\mathrm{R}}) \frac{\mathrm{d}}{\mathrm{d}t} \begin{pmatrix} \alpha \\ \beta \\ \phi \end{pmatrix} \tag{5.2}$$

where $\mathfrak{T}_{\mathrm{tan.}}$ is a tangent operator (see Chapter 4 of Ref. [112]).

Similarly to in Section 4.2, the equations of motion are assembled by summing the virtual work terms, this time for each constituent aircraft part, which may be flexible or rigid, using the expressions (4.3) - (4.8). Thus, d'Alembert's principle can be stated as

$$\frac{\partial W_T}{\partial \underline{q}} + \frac{\partial W_C}{\partial \underline{q}} + \frac{\partial W_K}{\partial \underline{q}} + \frac{\partial W_F}{\partial \underline{q}} + \frac{\partial W_M}{\partial \underline{q}} = 0 \tag{5.3}$$

In the present study, there are two flexible wings, a rigid tailplane (with angle of incidence i_t; see Ref. [48]), a rigid massless fuselage and a point-mass payload. A thrust vector T acts through the CG in the X direction. For rigid parts (i.e. the tailplane, fuselage and payload), stiffness and damping virtual work terms are alway zero, so their contributions to δW_K and δW_C are zero; moreover, for all (flexible and rigid) parts, the derivatives of wing curvature κ, with respect to the rigid-body coordinates, are similarly zero, i.e.

$$\frac{\partial}{\partial q_{\mathrm{T}}} \kappa_{[I]} = \begin{pmatrix} 0 & 0 & 0 \\ 0 & 0 & 0 \\ 0 & 0 & 0 \end{pmatrix}, \quad \frac{\partial}{\partial q_{\mathrm{R}}} \kappa_{[I]} = \begin{pmatrix} 0 & 0 & 0 \\ 0 & 0 & 0 \\ 0 & 0 & 0 \end{pmatrix}, \tag{5.4}$$

The derivatives of the global position and rotation of the aircraft, with respect to the rigid-body coordinates, are simply

$$\frac{\partial}{\partial q_{\mathrm{T}}} \overline{r}_{A[G]} = \begin{pmatrix} 1 & 0 & 0 \\ 0 & 1 & 0 \\ 0 & 0 & 1 \end{pmatrix}, \quad \frac{\partial}{\partial q_{\mathrm{R}}} \overline{r}_{A[G]} = \begin{pmatrix} 0 & 0 & 0 \\ 0 & 0 & 0 \\ 0 & 0 & 0 \end{pmatrix}, \tag{5.5}$$

and

$$\frac{\partial}{\partial q_{\mathrm{T}}}\vartheta_{A[G]} = \begin{pmatrix} 0 & 0 & 0 \\ 0 & 0 & 0 \\ 0 & 0 & 0 \end{pmatrix}, \quad \frac{\partial}{\partial q_{\mathrm{R}}}\vartheta_{A[G]} = \begin{pmatrix} 1 & 0 & 0 \\ 0 & 1 & 0 \\ 0 & 0 & 1 \end{pmatrix}. \tag{5.6}$$

Since the present work is concerned with longitudinal aircraft dynamics only, the flexible wings are assigned the same set of kinematic shape functions ($q_{\mathrm{f}} \in \mathbb{R}^{12}$), ensuring they are always symmetric; moreover, the rigid-body motions in Y, β and ϕ are neglected. Thus, (5.3) can be expressed as

$$\underbrace{\boldsymbol{M}_{\mathrm{a/c}}\big(\underline{q}(t), B'(s)\big)}_{15\times 15}\ddot{\underline{q}} = \underbrace{\boldsymbol{g}_{\mathrm{a/c}}\big(\underline{q}(t), \dot{\underline{q}}(t), B(s), B'(s)\big)}_{15\times 1}, \tag{5.7}$$

where $B(s)$ is the basis of shape functions (see Fig. 4.3) and

$$\boldsymbol{M}_{\mathrm{a/c}} = \boldsymbol{M}_{\mathrm{wing}} + \boldsymbol{M}_{\mathrm{tail}} + \boldsymbol{M}_{\mathrm{fuselage}} + \boldsymbol{M}_{\mathrm{payload}}, \qquad \boldsymbol{g}_{\mathrm{a/c}} = \boldsymbol{g}_{\mathrm{wing}} + \boldsymbol{g}_{\mathrm{tail}} + \boldsymbol{g}_{\mathrm{fuselage}} + \boldsymbol{g}_{\mathrm{payload}}. \tag{5.8}$$

In first-order form, the system may be expressed as

$$\frac{\mathrm{d}}{\mathrm{d}t}\begin{pmatrix} q_{\mathrm{f}} \\ q_{\mathrm{T}} \\ q_{\mathrm{R}} \\ \dot{\underline{q}} \end{pmatrix} = \underbrace{\begin{pmatrix} \dot{q}_{\mathrm{f}} \\ \dot{q}_{\mathrm{T}} \\ \mathfrak{T}_{\mathrm{tan.}}(q_{\mathrm{R}}) \setminus \dot{q}_{\mathrm{R}} \\ \boldsymbol{M}_{\mathrm{a/c}}^{-1}\boldsymbol{g}_{\mathrm{a/c}} \end{pmatrix}}_{30\times 1}. \tag{5.9}$$

5.3 Nominal aircraft configuration

The nonlinear dynamics of the HALE aircraft can be described by expressing (5.9) in the parameterised first-order form

$$\dot{x} = f\big(x, v_\infty, i_{\mathrm{t}}, T\big), \tag{5.10}$$

where $v_\infty \in \mathbb{R}$ is airspeed, $i_{\mathrm{t}} \in \mathbb{R}$ is the tailplane angle of incidence and $T \in \mathbb{R}$ is the thrust magnitude. The state vector may be written as

$$x = [x_{\mathrm{flex.}},\ x_{\mathrm{rigid}}]^{\mathsf{T}}, \tag{5.11}$$

where $x_{\mathrm{flex}} \in \mathbb{R}^{24}$ describes the deformation of the flexible wings and $x_{\mathrm{rigid}} \in \mathbb{R}^4$ are the rigid-body states. As noted in Section (5.2), the present study is concerned with longitudinal motion only, so both wings are described by a single shape function set, which ensures symmetric deformation. The freed rigid-body states, which describe the longitudinal aircraft motion in the global inertial frame shown in Fig. 5.1, may be written as

$$x_{\mathrm{rigid}} = \big[\alpha\ \dot{\alpha}\ \dot{X}\ \dot{Z}\big]^{\mathsf{T}}, \tag{5.12}$$

where α is the angle of attack of the aircraft, $\dot{\alpha}$ is the rate of change and $\dot{X}$ and $\dot{Z}$ are the translational velocities[1]. To ensure that the numerical continuation problem is well-posed, the

[1] Note that the true forward velocity of the aircraft is equal to $\dot{X} - v_\infty$.

Table 5.1: Nominal HALE aircraft parameters from Ref. [71].

Original parameters	
Wing	
Semi-span	16 m
Chord	1 m
Mass per unit length	0.75 kg/m
Out-of-plane stiffness (EI_{out})	2×10^4 N m^2
In-plane stiffness (EI_{in})	4×10^6 N m^2
Torsional stiffness (GJ)	1×10^4 N m^2
Moment of inertia	0.1 kg m
Spanwise elastic axis	0.5 chord
Centre of gravity	0.5 chord
Payload and tailboom	
Mass (payload)	50 kg
Moment of inertia (payload)	200 kg m^2
Length of tail boom	10 m
Tail	
Half span	2.5 m
Chord	0.5 m
Mass per unit length	0.08 kg/m
Moment of inertia	0.01 kg m
Centre of gravity	0.5 chord
Flight condition	
Altitude	20 km
Air density	0.0889 kg/m^3
Additional parameters	
Aerofoil	NACA0012
Structural damping factor (wing)	1×10^{-3}

states corresponding to translational positions X and Z are not captured[2].

The parameters of the nominal HALE configuration are shown Table 5.1. The aircraft has an aspect ratio of 32 and features highly flexible wings, the properties of which are identical to the half wing studied in Chapter 4 and include a non-zero (stiffness proportional) structural damping term. In the present study, the 50kg payload carried by the aircraft is located on the beam axis of the wings, and the tailboom does not have mass. A rigid aircraft configuration, which is useful for comparative purposes, is obtained by increasing the nominal wing stiffness EI_{out}, EI_{in} and GJ to sufficiently large values to prevent wing deformation.

[2]Inclusion of these position states would result in a non-invertible Jacobian matrix.

5.4 Trim solutions

The trim solutions (i.e. static equilibria) of the nonlinear dynamical system (5.10) are described by the implicit curve

$$f\left(x, v_\infty, i_\mathrm{t}, T\right) = 0, \tag{5.13}$$

which may be solved for given values of airspeed. Since the translational displacement states X and Z are not present in (5.12), the solutions of (5.13) actually describe *all* force/moment-balanced flight conditions, including cases where $\dot{X}, \dot{Z} \neq 0$ (i.e. steady translational motion). Thus, the trim solutions corresponding to rectilinear level flight, which are of most interest, must be obtained by solving the constrained trim problem

$$f\left(x, v_\infty, i_\mathrm{t}, T\right) = 0, \qquad \dot{X} = \dot{Z} = 0. \tag{5.14}$$

In the present study, solutions of (5.14) are found using a standard gradient-based optimisation routine, which is implemented to obtain the trimmed state vector x^* and trimmed parameters i_t^* and T^* as functions of v_∞. Thus, the original dynamical system (5.10) may be expressed as

$$\dot{x} = f\left(x, v_\infty, i_\mathrm{t}^*(v_\infty), T^*(v_\infty)\right) \tag{5.15}$$

and now describes the longitudinal dynamics of the aircraft, at a given airspeed, about a trim solution that satisfies (5.14).

Figure 5.2 (a, b) shows the trim solutions and resulting trimmed angles of attack, α^*, for both the flexible and rigid HALE aircraft configurations. In both cases, the requisite (negative[3]) i_t^* reduces with airspeed, as does the necessary thrust T^*; however, the magnitude of both trim parameters is greater for the flexible aircraft. The flexible case also necessities larger α^* than the rigid case, as expected due to the deformation of the wings, although this discrepancy reduces with airspeed. Figure 5.2 (c) shows that the wings provide a lower proportion of the overall lift in the flexible case. Overall, an appreciable difference exists between the two aircraft at lower airspeeds; however, this becomes smaller as airspeed is increased. At 30 m/s, Fig. 5.2 shows that the trim solutions for both aircraft are very similar.

Figures 5.3 & 5.4 shows the variation of the system modes for both cases. These are obtained using the linearisation of (5.15) about the trim conditions described in Fig. 5.2. The colouring of the solutions denotes the relative flexible/rigid modal compositions (magenta = flexible and black = rigid-body), which are derived from the eigenvectors converted to $\mathbb{R}$. In the rigid case (Fig. 5.3), the two modes in the system have no flexible component, as expected, and represent the classical phugoid and short-period responses. The frequencies of these rigid modes respectively decrease and increase with airspeed; at 15 m/s, they are 0.102 Hz and 0.523 Hz, whereas at 30 m/s they

[3]Note that, given large α^*, the tailplane still produces upwards force, which is as expected given the location of the aircraft CG.

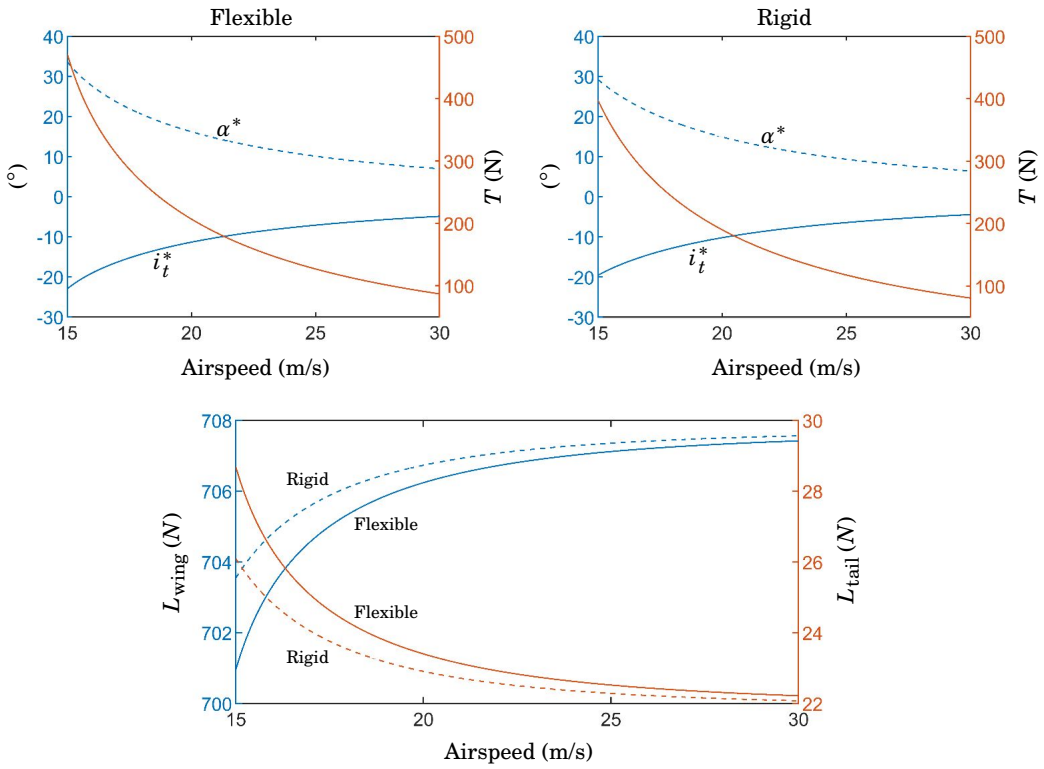

Figure 5.2: Trim solutions for the nominal (i.e. flexible) and rigid HALE aircraft configurations, for varying airspeed.

are 0.048 Hz and 1.03 Hz. As can be seen from the variation of modal damping, both modes are stable within the examined airspeed region, although the damping of the phugoid mode is very small at 30 m/s. As stated in Section 5.1, the rigid aircraft modes in the present study can be compared to those shown in Ref. [71]; at 25 m/s, the phugoid and short-period frequencies from this previous study are 0.051 Hz and 0.87 Hz, with damping ratios of 0.07 and 0.91. In the present study, the comparable frequencies are found to be 0.057 Hz and 0.86 Hz, with damping of 0.048 and 0.90 (Fig. 5.3). Thus, the largest discrepancy lies in the phugoid damping, which is as expected, due to the dominance of drag (and thus higher sensitivity to aerodynamic modelling) in this mode.

When the modes of the flexible aircraft are examined (Fig. 5.4), the presence of aeroelastic effects is clear. Distinct modes that are dominated by wing deformation now exist in the system (indicated by the magenta solutions); at 15 m/s, the lowest four have frequencies of 0.37 Hz, 2.25 Hz, 3.46 Hz and 6.21 Hz, respectively. The first, second and fourth of these modes correspond to the 1$^{\text{st}}$, 2$^{\text{nd}}$ and 3$^{\text{rd}}$ out-of-plane bending modes, whereas the third is the 1$^{\text{st}}$ torsion/in-plane coupled mode (this structural coupling was discussed in Section 2.4). From its varying colouring, it can be seen that the 1$^{\text{st}}$ bending mode gains an increasingly large rigid-body component as airspeed increases. At 21.93 m/s, the torsion/in-plane flexible mode becomes negatively damped,

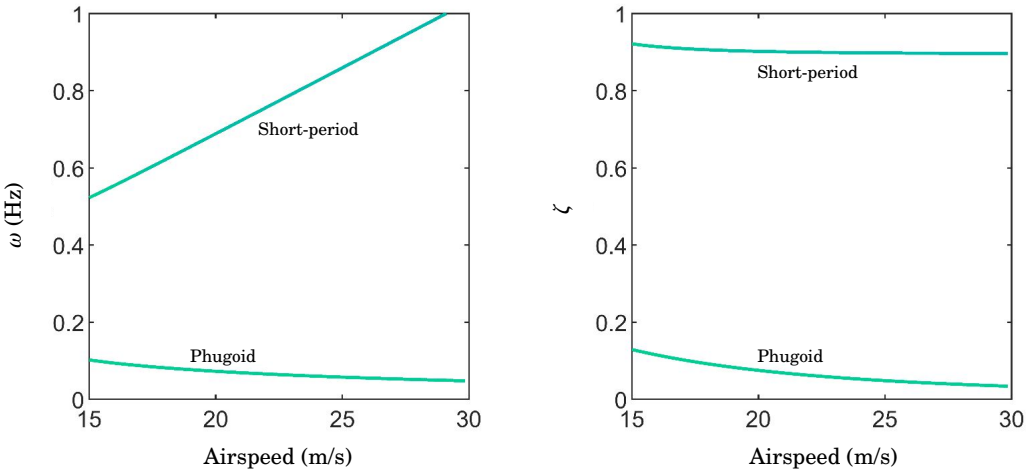

Figure 5.3: Variation of phugoid and short-period frequencies and damping, for varying airspeed, for rigid HALE aircraft.

as shown by the vertical dashed line, indicating the occurrence of a critical flutter interaction. This interaction destabilises the trim solutions beyond 21.93 m/s; at airspeeds above this boundary, tiny perturbations to the system will result in divergent oscillatory behaviour. The flutter frequency is 3.51 Hz; the nature of the oscillations will be discussed in Section 5.5.

The mode in Fig. 5.4 that has the lowest frequency comprises purely rigid-body motion and corresponds to the phugoid mode. This mode varies very similarly to that of the rigid aircraft; at 15 m/s, it has a frequency of 0.104 Hz, whereas at 30 m/s this has decreased to 0.047 Hz. Moreover, the damping similarly decreases with airspeed, as shown in the right panel. The short-period mode, however, is significantly different compared to the rigid case; in the low-airspeed region close to 15 m/s (Fig. 5.4, a), the mode actually comprises two real eigenvalues and is non-oscillatory, whereas in region (b) the eigenvalues have become complex-conjugate and the mode is oscillatory. In the airspeed region beyond 23.13 m/s (c), the mode is non-oscillatory again. Thus, the presence of wing flexibility leads to a qualitatively different short-period mode compared to the rigid aircraft; this was similarly observed in Ref. [71].

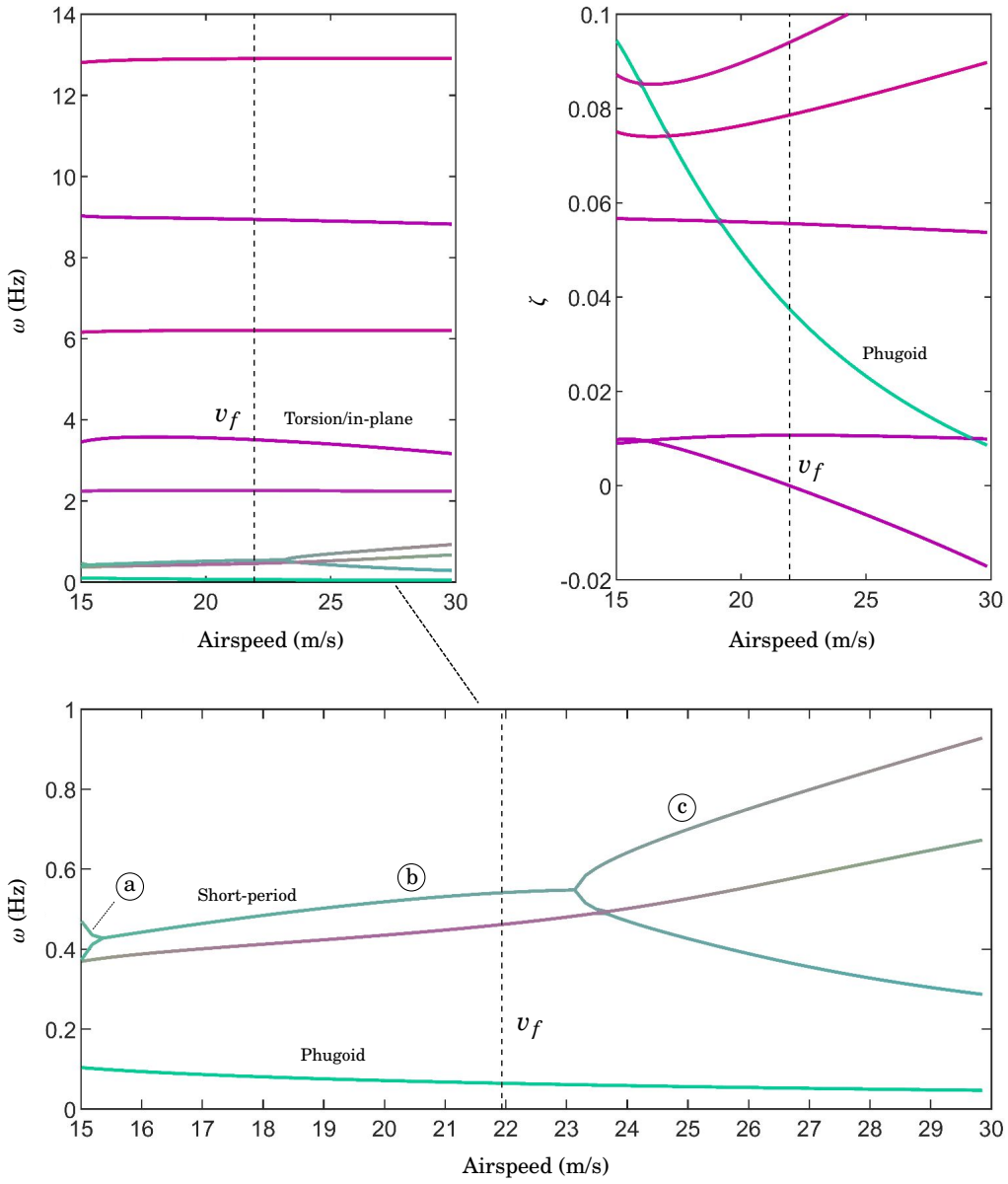

Figure 5.4: Variation of modal frequencies and damping, for varying airspeed, for nominal (i.e. flexible) HALE aircraft (magenta = flexible, black = rigid).

5.5 Nominal aircraft bifurcation results

Figures 5.5 and 5.6 show the one-parameter continuation of equilibria and LCOs for the nominal (i.e. flexible) HALE aircraft. Here, solutions are shown in terms of out-of-plane bending displacement and twist, at the wing tip, as observed in the local aircraft frame. A Hopf bifurcation at 21.93 m/s indicates flutter, which is as expected from the negative modal damping shown in Fig. 5.4. This Hopf is supercritical, as is evident from the stable LCO solution emanating from the

bifurcation point. Periodic fold bifurcations occur at 25.67 m/s and at 23.69 m/s, respectively; within this airspeed interval, there exists a sensitivity to initial conditions, due to the coexistence of two attracting LCOs, and a hysteresis loop. The result is a discontinuous jump after the the first fold at 25.67 m/s; the detrimental effects of this phenomena will become evident. In both figures, single-period time histories are shown for selected LCO solutions at 22.14 m/s, 25.07 m/s and 29.96 m/s respectively; these will be discussed later.

The equilibrium solution in Fig. 5.5 shows that the trim tip displacement, and thus overall out-of-plane bending of the wing, decreases with airspeed. This is as expected from Fig. 5.2, which shows that the difference between the flexible and rigid aircraft trim solutions reduces as airspeed increases. Beyond the flutter point, the LCOs have small amplitude and remain close to the destabilised equilibria; after the first fold at 25.67 m/s, the oscillations maintain a similarly small amplitude, but the mean deformation drops. The solutions further depart from the equilibrium solution as airspeed further increases. The variation of tip twist in Fig. 5.6 shows that, while there is negligible deformation in the trim conditions, this is not true beyond the flutter point, as the LCOs have a large torsional component that monotonically increases with airspeed. (Just after the first fold, the amplitude jumps from $\pm 4.34^\circ$ to $\pm 13.89^\circ$.) Thus, while the out-of-plane bending deformation is most present in the trim solutions, it is the twisting of the wing that is most significant in the oscillations beyond the flutter point (this is expected, given that it is the torsion/in-plane mode that loses stability).

As was shown in Chapter 4, the existence of periodic folds in the system may be understood by considering the physical characteristics of the LCOs. The time history for the LCO at 22.14 m/s (i.e. just beyond the Hopf bifurcation), which is shown in both Figs. 5.5 & 5.6, reveals that the out-of-plane bending component has twice the frequency of the torsional component. Thus, the critical interaction that destabilises the equilibrium at the flutter point actually comprises a 2:1 ratio, involving the 3^{rd} out-of-plane bending mode, which has a frequency of 6.21 Hz at the critical airspeed (see Fig. 5.4). This is in contrast to the flutter mechanism observed for the half wing with a fixed root, where the critical interaction instead involved the 2^{nd} bending mode (as shown in Fig. 4.11). The selected LCO at 25.07 m/s, which occurs within the fold interval, clearly shows an additional frequency component, which is indicative of a 4:1 interaction with the 4^{th} bending mode; this interaction also exists, to a lesser extent, in the LCO at 29.96 m/s. Figure 5.7 shows the mean spanwise out-of-plane deformation for each of the selected oscillations, and illustrates that the 4^{th} bending mode is indeed present at 25.07 m/s and at 29.96 m/s.

The relevance of the higher mode is as follows. Recall, from Section 2.2.1, that LCOs in a nonlinear aeroelastic system are the result of critical interactions occurring intermittently during its time-varying deformation. Thus, for two stable periodic motions to coexist at the same airspeed, the interaction that necessarily decreases for the first LCO must be replaced by another as the system further deforms; this second interaction necessarily increases and then also decreases with deformation. In the current example, it is clear that between 25.67 m/s -

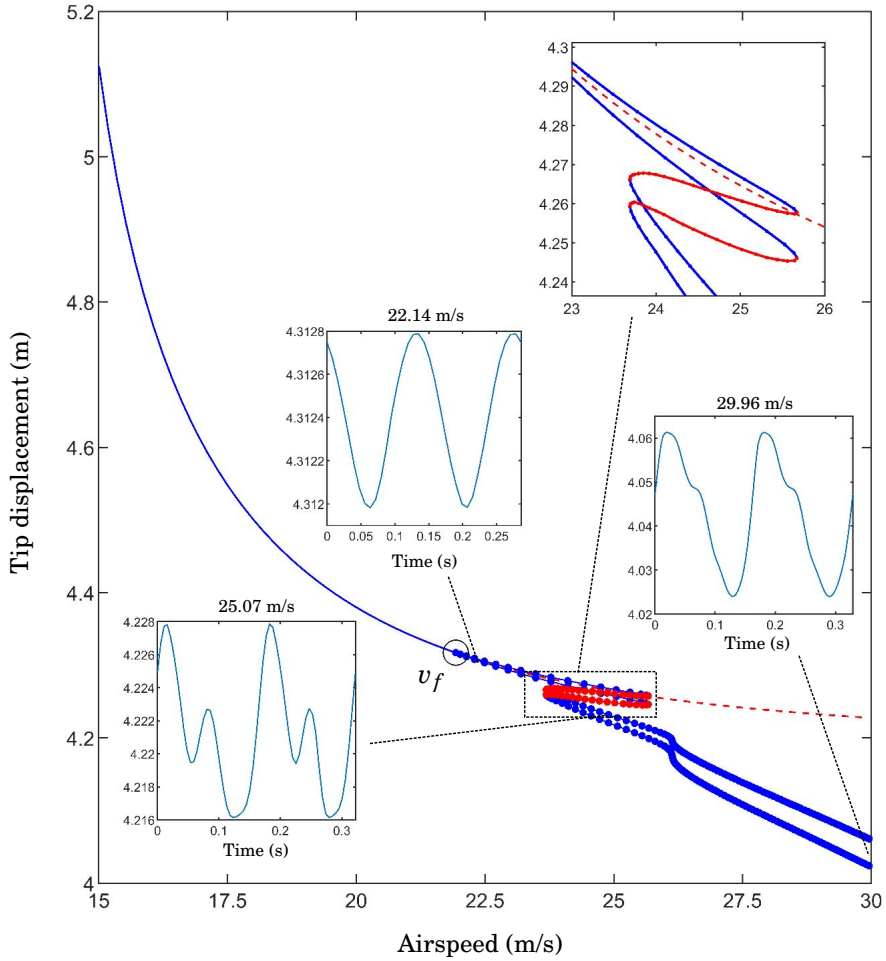

Figure 5.5: One-parameter continuation of equilibria and LCOs, for varying airspeed, for the flexible HALE aircraft.

23.69 m/s, the torsional/in-plane motion of the wing strongly interacts with both the 3rd and 4th out-of-plane bending modes, respectively, at different deformations. At the linearised flutter point, these modes have frequencies of 6.21 Hz and 12.91 Hz, which are respectively ~1.8 and ~3.7 multiples of the 3.51 Hz flutter mode.

As has been emphasised throughout this thesis, a supercritical Hopf bifurcation is the desired outcome at the flutter point of a nonlinear aeroelastic system (see Section 2.2.2). While this desired bifurcation is indeed present in the current aircraft system, the subsequent periodic fold bifurcations lead to phenomena that, despite occurring beyond the flutter point, are nevertheless detrimental. The aforementioned sensitivity to initial conditions, between 25.67 m/s - 23.69 m/s, means that finite disturbances to the aircraft within this interval may result in large unexpected twisting of the wing (as is evident from Fig. 5.6; the oscillations could more than double in amplitude), which cannot be removed immediately due to the hysteresis. The detrimental effects

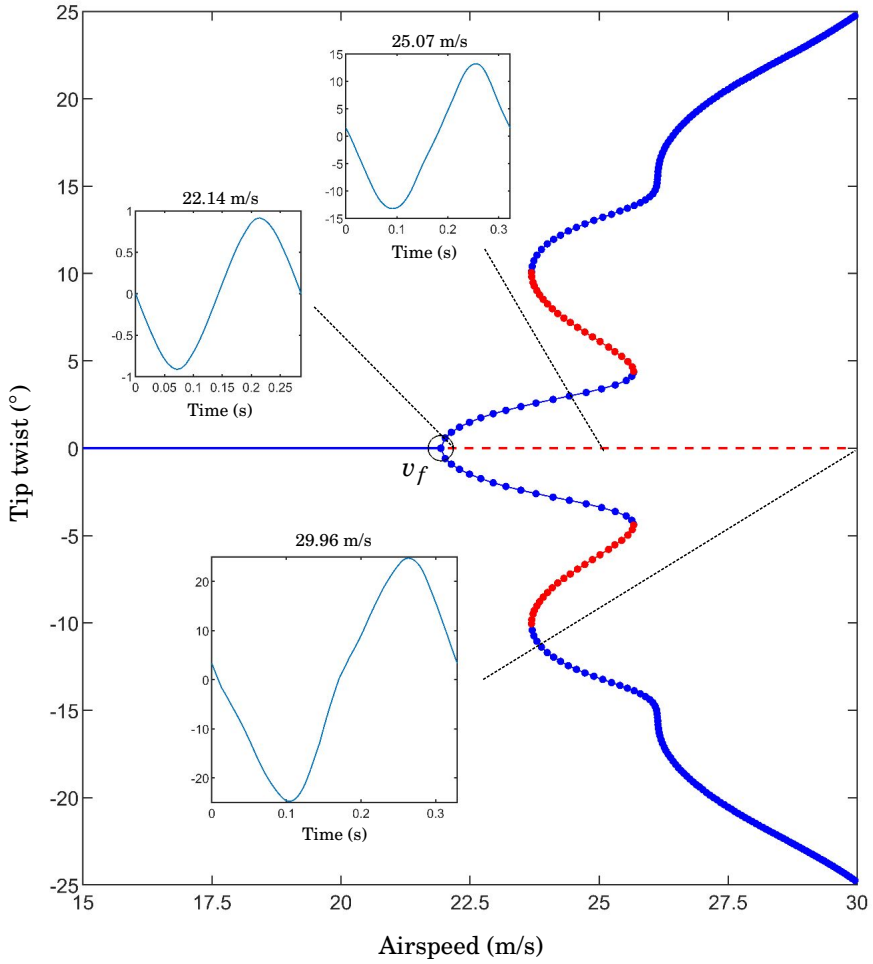

Figure 5.6: One-parameter continuation of equilibria and LCOs, for varying airspeed, for the flexible HALE aircraft.

of the folds are also impactful when the overall rigid-body motion of the aircraft is considered, as will now be discussed.

Figures 5.8 - 5.11 show the above continuation results in terms of the rigid-body states α, $\dot{\alpha}$, $\dot{X}$ and $\dot{Z}$. In all cases, the periodic solutions emanating from the Hopf have very small amplitude, indicating that very little oscillatory motion of the aircraft, as a whole, is present in the LCOs. (In fact, the amplitudes of the oscillations in α, $\dot{X}$ and $\dot{Z}$ are negligible, and can practically be viewed as equilibria.) At any supercritical airspeed, the aircraft has almost-steady (i.e. balanced forces and moments) translational motion; this lack of interaction with the oscillating wings is not unexpected, given the large frequency difference between the critical flutter mode and the rigid-body modes (shown in Fig. 5.4). This behaviour is clearly the desirable outcome when compared to other more deleterious possibilities (e.g. the upset and loss of aircraft control); moreover, just beyond the Hopf bifurcation, the LCO solutions remain very close the equilibria

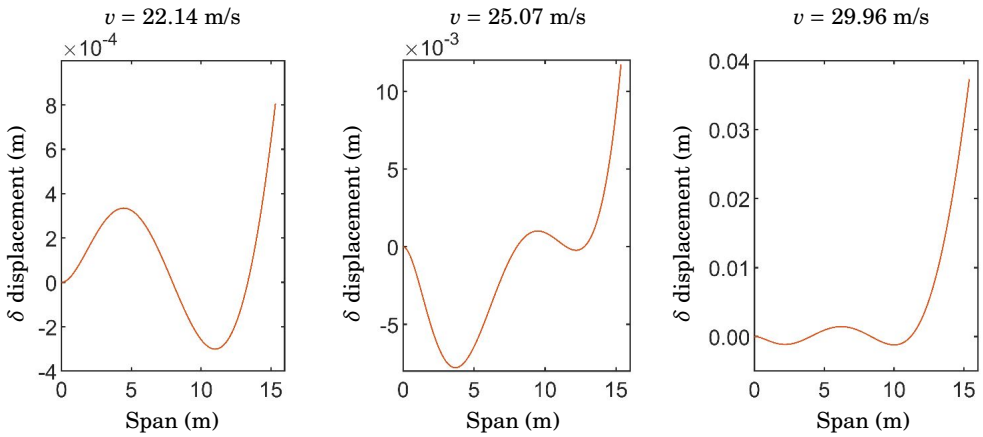

Figure 5.7: Mean spanwise out-of-plane deformation of wing, for the selected LCOs at 22.14 m/s, 25.07 m/s and 29.96 m/s shown in Fig. 5.5.

solution, meaning that the aircraft remains practically stationary just after the boundary is exceeded.

The detrimental effect of the periodic folds, however, is significant. The discontinuous jump at 25.67 m/s is found to be large in all rigid-body states; α jumps from 9.1° to 6°, and $\dot{X}$ and $\dot{Z}$ jump from 0.23 m/s and -0.24 m/s to 2.07 m/s and -2.05 m/s respectively. Thus, while marginally exceeding the 21.93 m/s flutter point is not particularly detrimental, exceeding 25.67 m/s results in an immediate change in both the angle of attack and the translational velocity of the aircraft, which cannot be reversed unless the airspeed is reduced to below 23.69 m/s.

Figure 5.12 shows time histories for the rigid states at 26.5 m/s, after a +1° perturbation to α at the trim condition. The slowly-decaying phugoid mode is clearly evident in the initial part of the response, however, after ~100s the system rapidly converges to the almost-steady LCO; the resulting steady descent in Z is shown in Fig. 5.13 (recall that Z is positive upwards, as shown in Fig. 5.1).

Given the above discussion, a practical scenario for the flight dynamics of the flexible HALE aircraft could be as follows, assuming that airspeed increases slowly and the trim parameters i_t and T are scheduled per Fig. 5.2. At airspeeds below the flutter point (i.e. 21.93 m/s), the aircraft is in a 'straight line' trim condition, where any small disturbance (e.g. to α) results in the expected decaying phugoid and short-period response. (The frequencies of these modes vary with airspeed as shown in Fig. 5.4.) As airspeed increases, the static deformation of the trimmed wings reduces, as does α. When the airspeed exceeds 21.93 m/s, the wings begin to oscillate, due to a critical interaction between torsion/in-plane and 3$^{\text{rd}}$ bending, and the aircraft gains very slow translational motion. When the airspeed exceeds 23.13 m/s, the short-period response is no longer oscillatory, as shown in Fig. 5.4. As the airspeed exceeds the periodic fold at 25.67 m/s, the wing oscillations now have a large component of the 4$^{\text{th}}$ bending mode, and have almost twice the

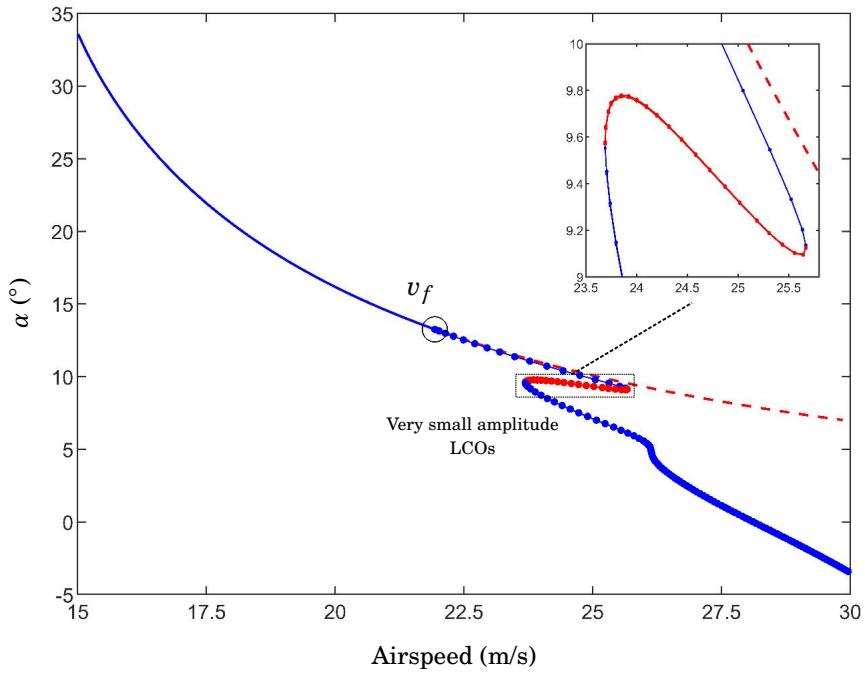

Figure 5.8: One-parameter continuation of equilibria and LCOs, for varying airspeed, for the flexible HALE aircraft (rigid-body).

torsional amplitude. As a consequence, the practically-steady α jumps from 9.13° to 6.11°, and the horizontal and vertical translational velocities increase in magnitude to 2.14 m/s and -1.99 m/s, respectively. At even higher airspeeds, α eventually become negative, the amplitude of the periodic twisting of the wing further increases, as do the translational velocities.

In summary, while the trim solutions for the flexible aircraft are not hugely dissimilar to the rigid case, the onset of flutter and the subsequent folds in the LCO solutions means that the stability and overall behaviour is significantly different. Thus, despite the minimal interaction between the flexible and rigid-body modes, rigid analysis alone does not adequately predict the flight dynamics of the aircraft beyond the flutter point.

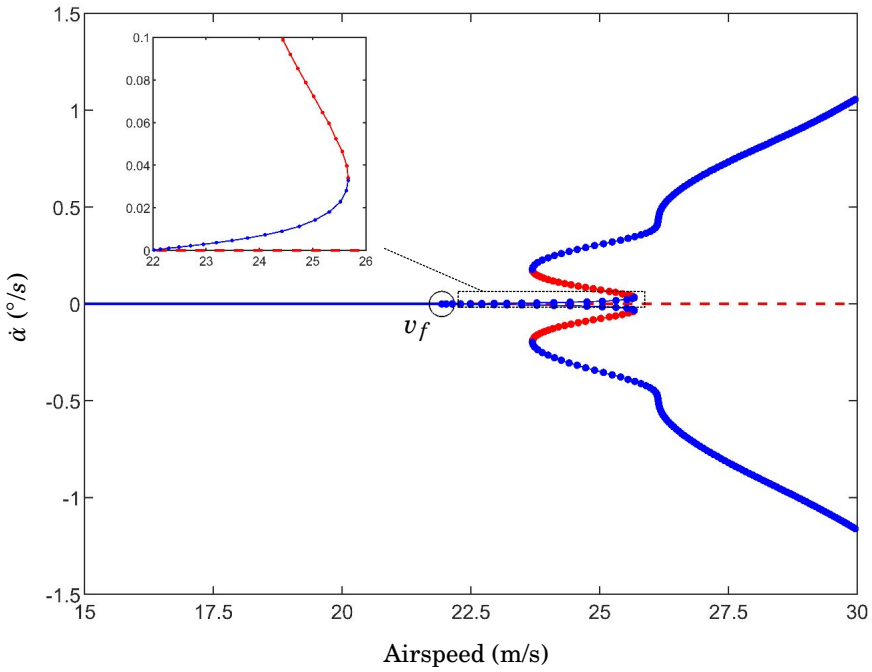

Figure 5.9: One-parameter continuation of equilibria and LCOs, for varying airspeed, for the flexible HALE aircraft (rigid-body).

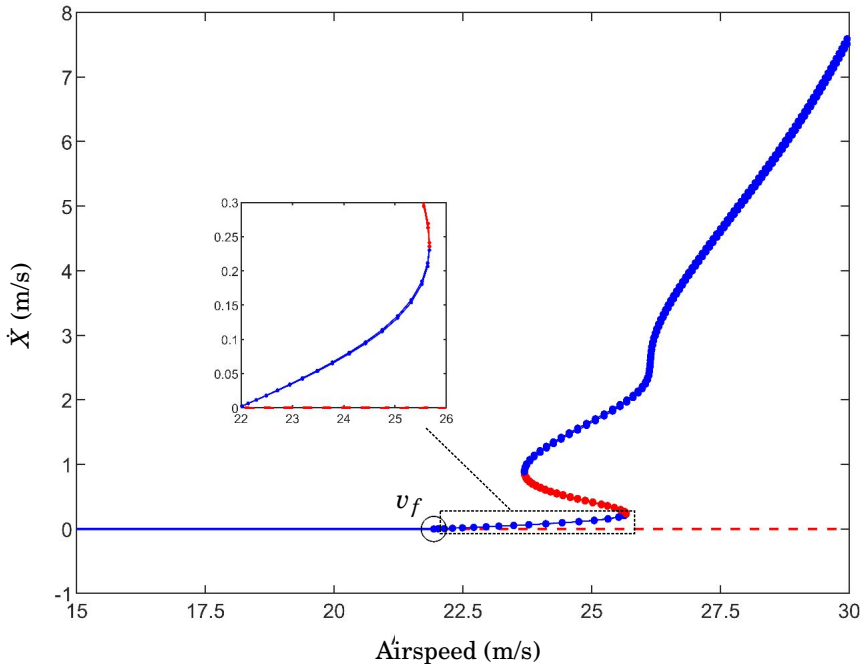

Figure 5.10: One-parameter continuation of equilibria and LCOs, for varying airspeed, for the flexible HALE aircraft (rigid-body).

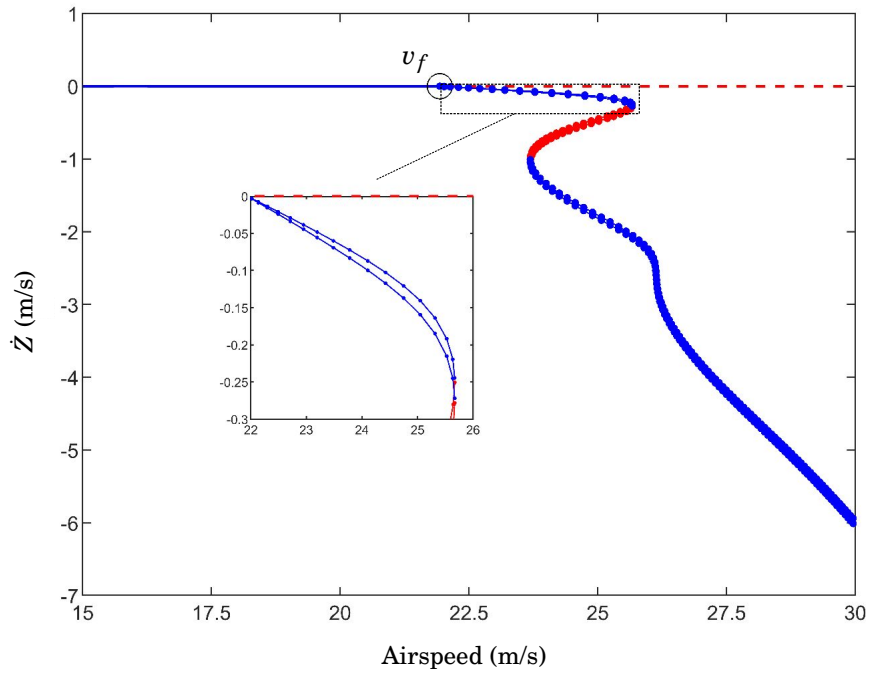

Figure 5.11: One-parameter continuation of equilibria and LCOs, for varying airspeed, for the flexible HALE aircraft (rigid-body).

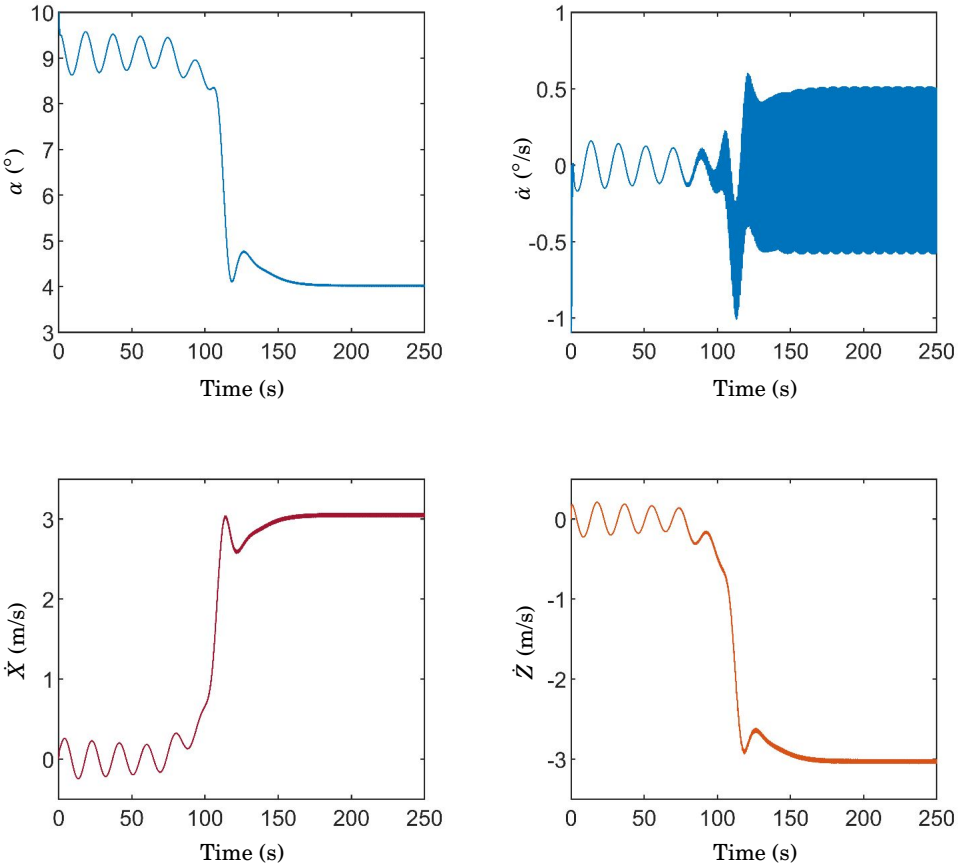

Figure 5.12: Time history of flexible HALE aircraft, showing rigid-body states.

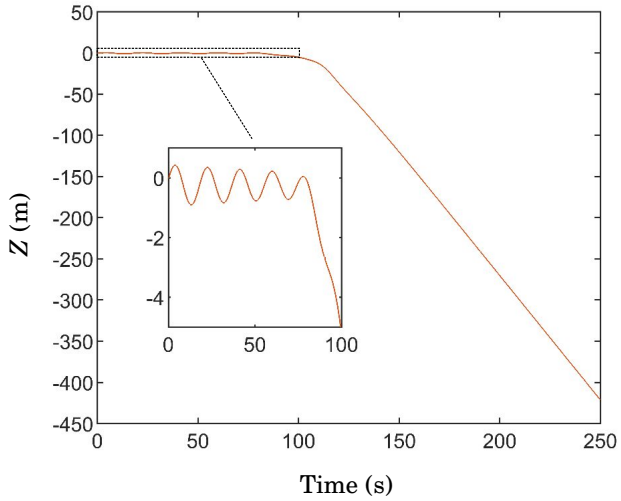

Figure 5.13: Time history of flexible HALE aircraft, showing vertical rigid-body displacement.

5.6 Variation of torsional stiffness

As discussed above, coexisting LCOs in a nonlinear aeroelastic system are the result of several different critical interactions occurring as the system deforms. In the present aircraft system, the 1st torsional/in-plane mode of the flexible wing critically interacts with both the 3rd and 4th out-of-plane bending modes in the airspeed region 25.67 m/s - 23.69 m/s. The resulting coexisting LCOs, and more pertinently, the periodic fold bifurcations, have been shown to detrimentally affect the performance of the aircraft, particularly when the rigid-body motion is considered; it is therefore useful to investigate how readily the phenomena can be removed. In the present system, the simplest means of affecting the LCOs is to vary the torsional stiffness GJ, as doing so will largely affect the flutter frequency, whilst having little effect on the out-of-plane bending frequencies. Moreover, given that the secondary LCOs have frequency lower than the torsional mode (e.g. see the time history for 25.07 m/s in Fig. 5.5), it follows that sufficiently raising GJ may prevent the interaction from critically occurring.

Figures 5.14 & 5.15 show the equilibria and LCOs, in terms of tip displacement and twist, for the case where GJ is increased to 150% of the nominal value shown in Table 5.1. Here, flutter occurs at a higher airspeed of 26.2 m/s and, similarly to the nominal case, is caused by a 2:1 interaction involving the 3rd bending mode. The periodic folds no longer exist, however, indicating that the 4:1 interaction with the 4th bending mode is no longer sufficient for the additional LCOs. (Note that the frequency of the flutter mode has increased to 4.16 Hz in this case.) Figure 5.16 shows the rigid-body states and demonstrates that, although there are no folds, the LCO solutions in $\dot{X}$ and $\dot{Z}$ do not stay close to the equilibria immediately after the Hopf, as was seen for the nominal case; thus, should the aircraft marginally exceed the flutter point, the translational motion is no longer very slow. Depending on the exact flight requirements, these dynamics may or may not be more favourable than the nominal system, despite the removal of the detrimental periodic fold bifurcations.

Figure 5.17 compares the LCO solutions for GJ = 100%, GJ = 125% and GJ = 150%, which are shown in terms of α. In the intermediate case (125%), the folds are evidently still present in the system, but occur at very close airspeeds, indicating that they are close to vanishing. Thus, the transition is smooth; should a two-parameter continuation of periodic folds be performed for varying airspeed and GJ, a fold in the solutions would be expected at a critical stiffness just higher than 125%. The flutter frequencies for these cases are 3.5 Hz, 3.86 Hz and 4.16 Hz respectively.

Figures 5.18 & 5.19 show the flexible solutions for the case where GJ is reduced to 50%. The flutter point now occurs at a lower airspeed, and has a frequency of 2.6 Hz. The folds still exist in the system, at 18.98 m/s and 18.11 m/s respectively; the unstable LCO solution is very close to the unstable equilibria, indicating that, in the fold region, the critical interaction involving the 4th bending mode occurs very close to the trim condition. Figure 5.19 shows the tip twist and shows that very large angles (which, in reality, would be prohibited by aerodynamic nonlinearity)

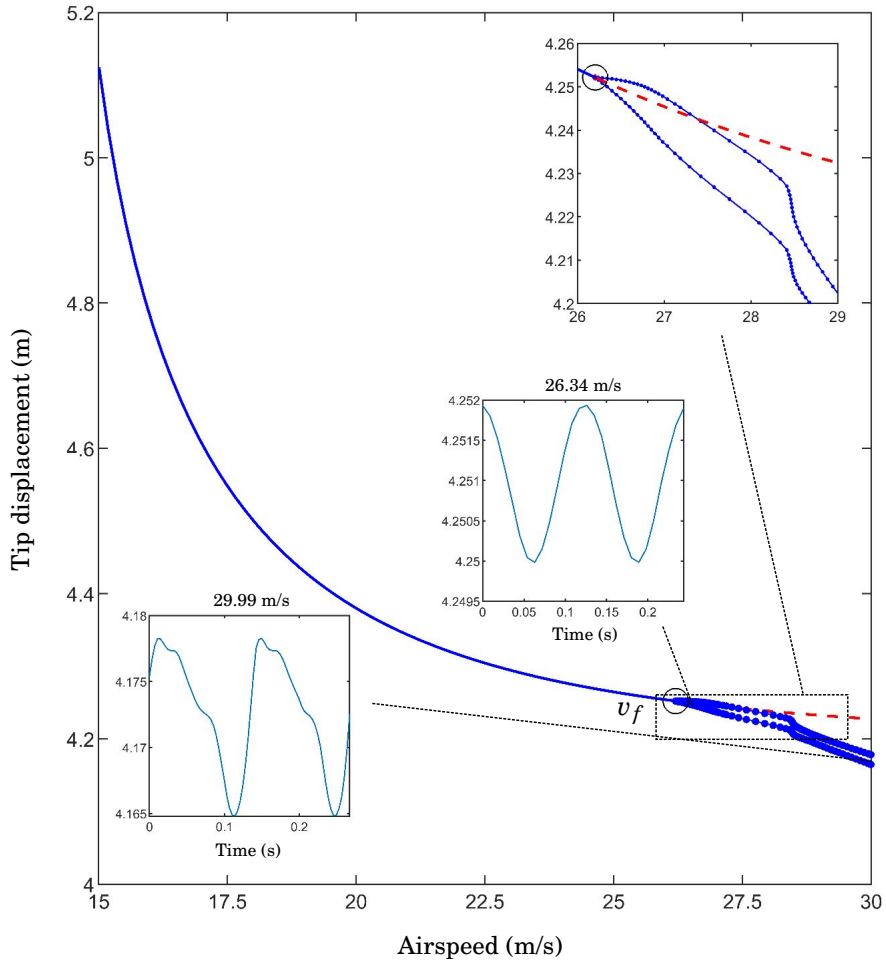

Figure 5.14: One-parameter continuation of equilibria and LCOs, for varying airspeed, for the flexible HALE aircraft when $GJ = 150\%$ nominal.

are present in the LCOs beyond the folds. Figures 5.20 - 5.23 show the rigid-body states; in each case, the unstable LCOs are similarly close to the equilibria and, moreover, the resulting discontinuous jump is less significant compared to the nominal case. Thus, while reducing GJ causes the critical 4:1 interaction to occur more readily (i.e. closer to the trim condition), the overall effect on the supercritical dynamics is actually beneficial when compared to the nominal aircraft. This benefit, however, is clearly offset by the significantly reduced flutter airspeed.

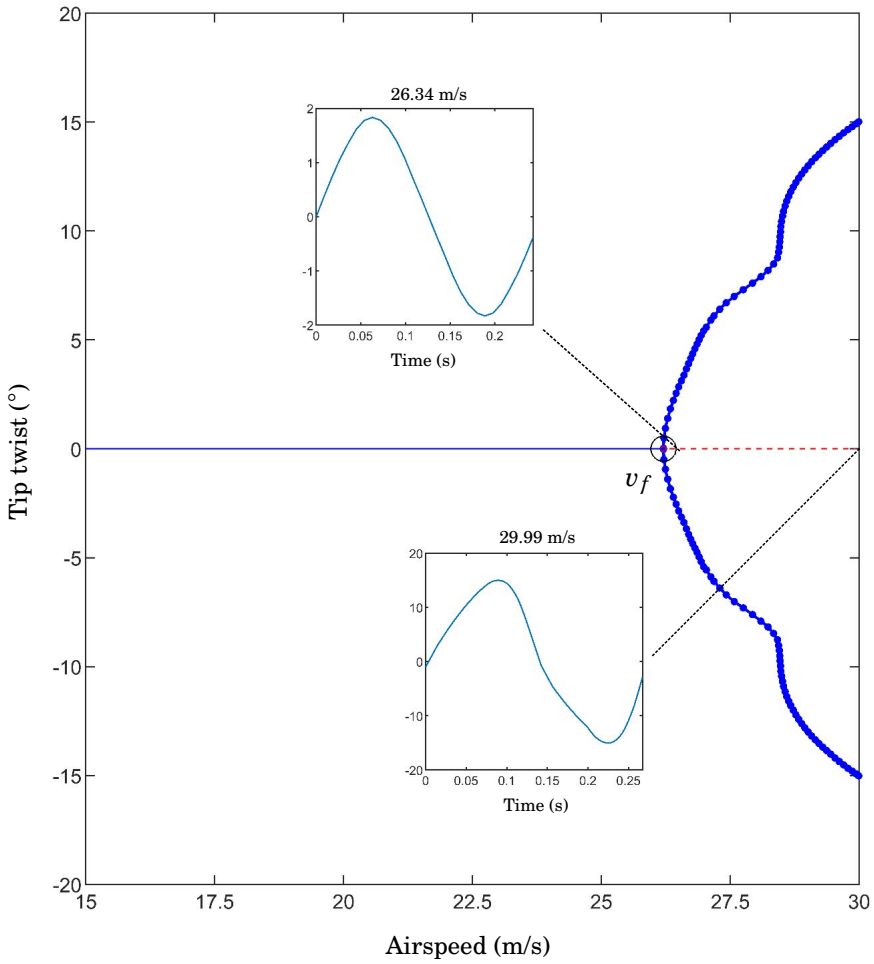

Figure 5.15: One-parameter continuation of equilibria and LCOs, for varying airspeed, for the flexible HALE aircraft when $GJ = 150\%$ nominal.

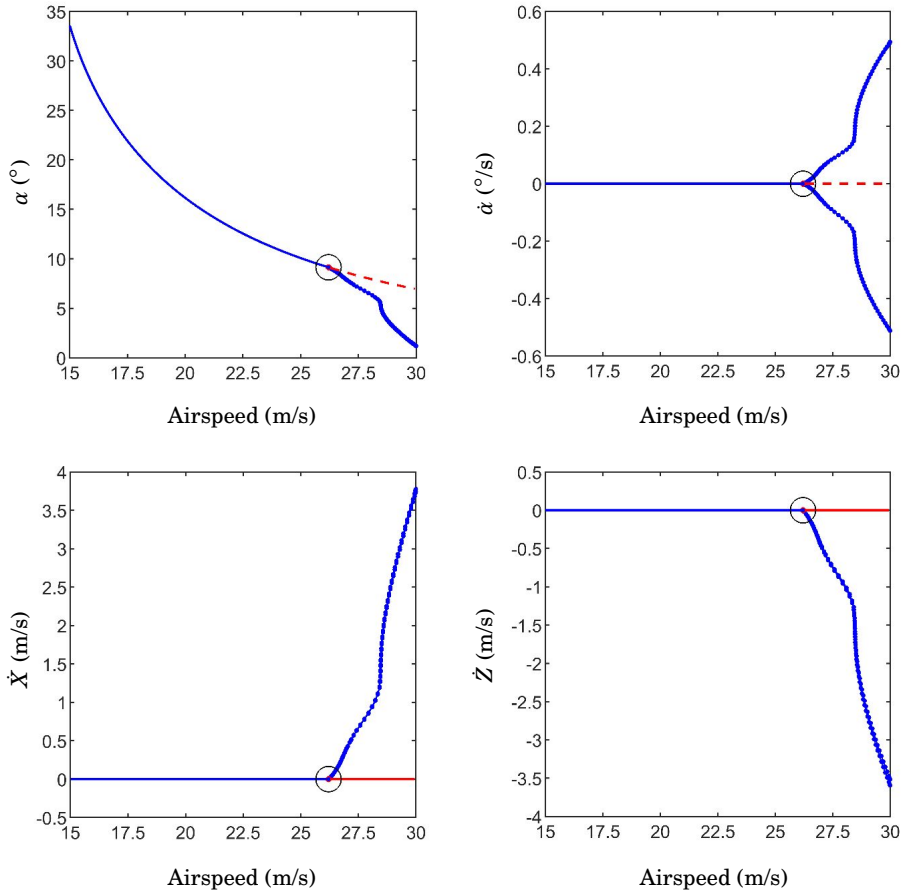

Figure 5.16: One-parameter continuation of equilibria and LCOs, for varying airspeed, for the flexible HALE aircraft (rigid-body states) when $GJ = 150\%$.

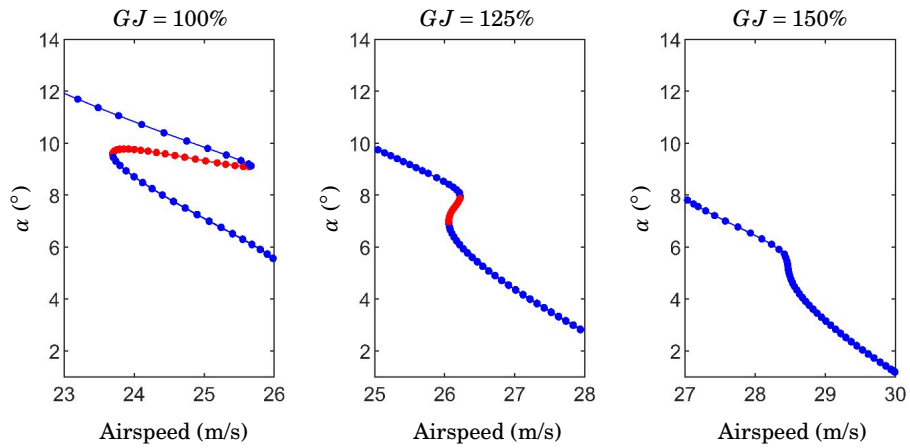

Figure 5.17: One-parameter continuation of LCOs, for varying airspeed, for the flexible HALE aircraft (increasing GJ).

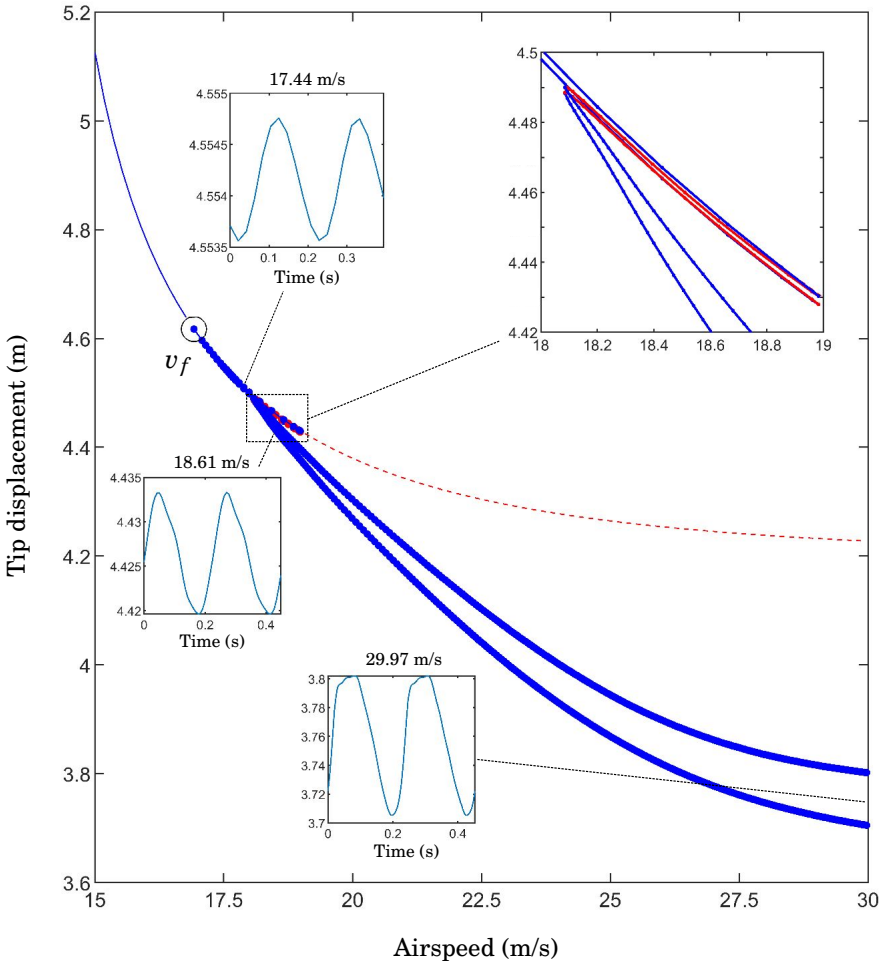

Figure 5.18: One-parameter continuation of equilibria and LCOs, for varying airspeed, for the flexible HALE aircraft when $GJ = 50\%$ nominal.

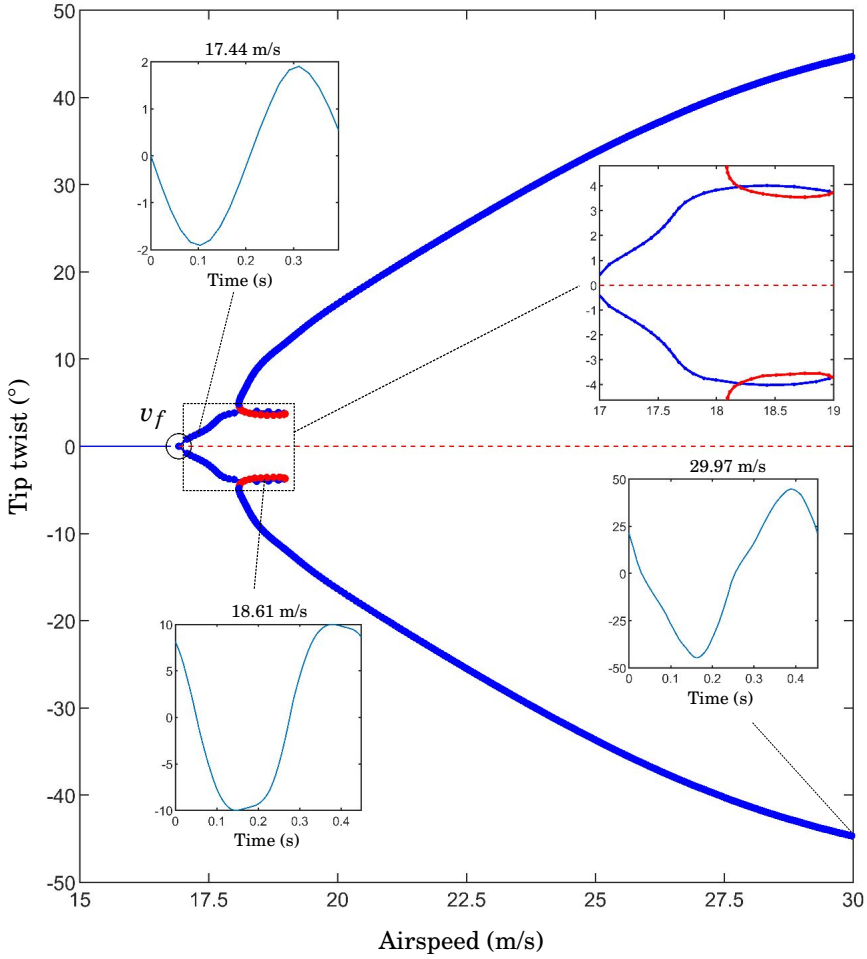

Figure 5.19: One-parameter continuation of equilibria and LCOs, for varying airspeed, for the flexible HALE aircraft when $GJ = 50\%$ nominal).

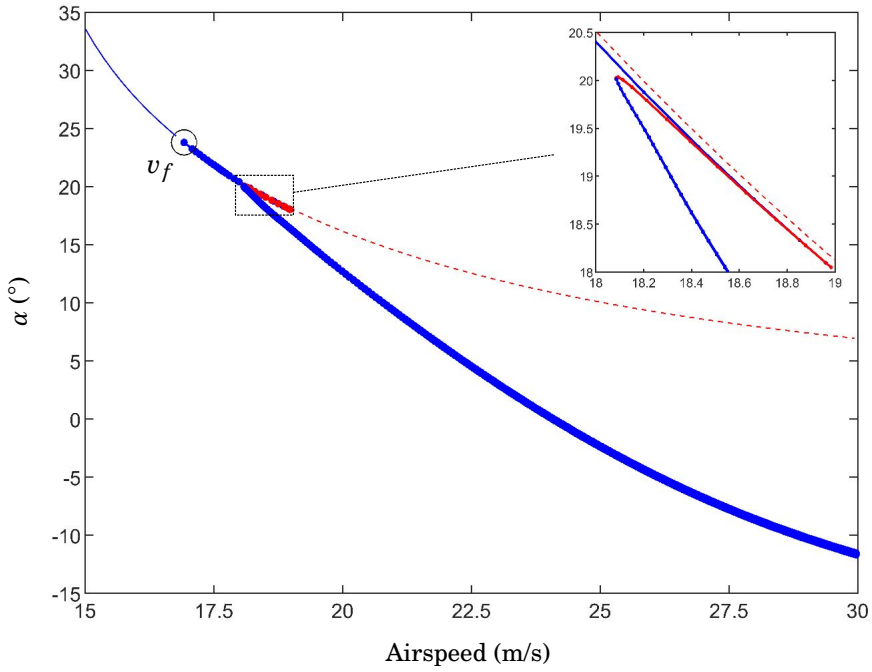

Figure 5.20: One-parameter continuation of equilibria and LCOs, for varying airspeed, for the flexible HALE aircraft (rigid-body, when $GJ = 50\%$ nominal).

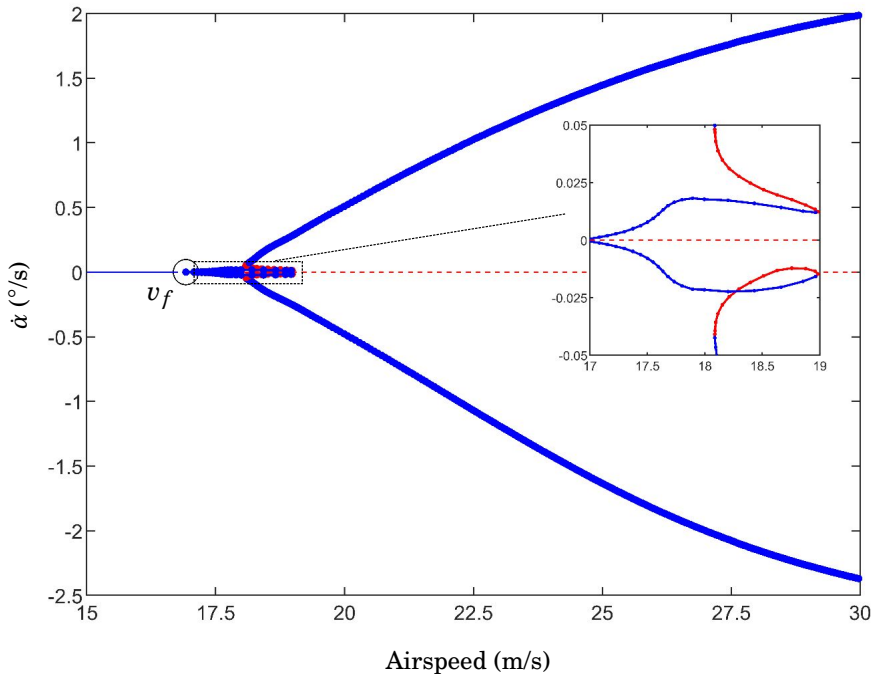

Figure 5.21: One-parameter continuation of equilibria and LCOs, for varying airspeed, for the flexible HALE aircraft (rigid-body, when $GJ = 50\%$ nominal).

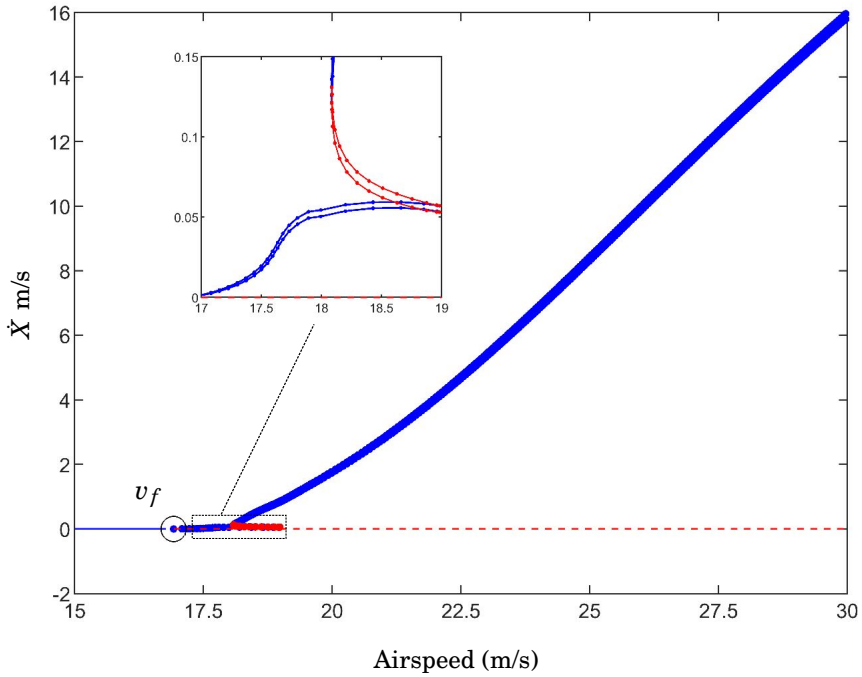

Figure 5.22: One-parameter continuation of equilibria and LCOs, for varying airspeed, for the flexible HALE aircraft (rigid-body, when $GJ = 50\%$ nominal).

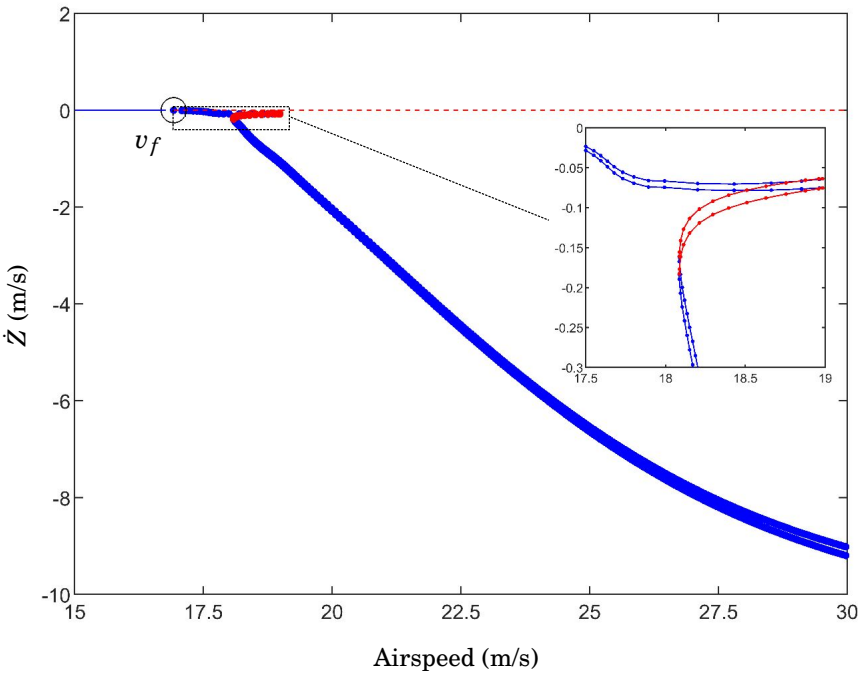

Figure 5.23: One-parameter continuation of equilibria and LCOs, for varying airspeed, for the flexible HALE aircraft (rigid-body, when $GJ = 50\%$ nominal).

5.7 Conclusions

In this chapter, numerical continuation has been used to investigate the nonlinear longitudinal dynamics of a high altitude, long endurance (HALE) aircraft with flexible, high-aspect-ratio wings. Trim conditions have been obtained for the nominal (i.e. flexible) aircraft and compared to the equivalent rigid configuration; while the phugoid mode is similar, the short-period mode is qualitatively different between the two. The numerical continuation of equilibria and limit cycle oscillations (LCOs) reveals that flutter occurs in the system due to an interaction between two flexible modes of the wing, although the involved bending mode is not the same as that previously observed for the half wing in a fixed root condition. The Hopf bifurcation at the flutter point is supercritical, and the resulting small-amplitude oscillations almost solely involve the wings, due to a lack of significant interaction between the flexible and rigid-body modes. However, the presence of periodic fold bifurcations in the LCO solutions leads to detrimental phenomena, particularly in the translational rigid-body velocities of the aircraft. Increasing the torsional stiffness of the wing is seen to remove the periodic folds, although the resulting dynamics are not necessarily more desirable than the nominal case. Conversely, reducing the torsional stiffness causes the folds to occur closer to the trim solutions; due to this, the detrimental effects are observed to be less impactful compared to the nominal case. Overall, this chapter has shown that the flutter analysis of an aircraft with flexible, high-aspect-ratio wings with geometric nonlinearity necessitates the use of nonlinear methods, and that even a supercritical Hopf with small-amplitude LCOs can lead to negative effects on the overall aircraft flight dynamics.

CHAPTER 6

CONCLUSIONS

This chapter summarises the key outcomes and overall conclusions from the research in this thesis. Potential extensions of the work are proposed, and there is a discussion regarding the future outlook for high-aspect-ratio wings and the use of numerical continuation techniques in the civil aviation industry.

6.1 Research outcomes

This thesis has investigated the nonlinear dynamics of flexible, high-aspect-ratio wings. The aerodynamic benefit afforded by high-aspect-ratio wings means they are likely to play a role in the design of future commercial aircraft; the flexibility of these wings, however, may lead to nonlinear dynamical phenomena that cannot be investigated using traditional flutter methods. In the present research, novel contributions have been made by using numerical continuation to obtain equilibria, limit cycle oscillations (LCOs), and bifurcations, for low-order models describing high-aspect-ratio wings with geometric nonlinearity. Chapter 3 investigated Hopf criticality in a nonlinear, 2 degree-of-freedom (DoF) flutter wing model and demonstrated how criticality is related to physical characteristics of the modes of the linearised system; specifically the convergence of the mode frequencies. Chapter 4 used a fully nonlinear beam model of a high altitude, long endurance (HALE) wing and revealed complex dynamics; moreover, the observations from Chapter 3 relating to Hopf criticality were built upon. Chapter 5 investigated the complete HALE aircraft, and while the flutter point of the flexible system was found to be supercritical and led to small-amplitude LCOs, the existence of periodic fold bifurcations resulted in undesirable phenomena, particularly when considering the rigid-body flight dynamics.

Extending the conclusions drawn within each chapter, a number of more general conclusions can be made:

1. **Geometric nonlinearity must be captured, as it can be the cause of detrimental phenomena**

   In all of the studies in this thesis, undesirable nonlinear dynamics (e.g. subcritical LCOs or periodic folds) were shown to exist, due to the presence of large wing flexibility and the resulting variation of structural modes, without aerodynamic nonlinearity. (The implications of using linear aerodynamics will be discussed in Section 6.2.) Detrimental phenomena were either observed in the nominal wing configurations, or after the variation of a structural parameter (e.g. stiffness or damping). Indeed, as explained in Chapter 3, provided no part of a given aeroelastic system is stalled at the bifurcation condition, flutter criticality is entirely prescribed by nonlinearity in the structure. Further to this, Chapter 5 showed that undesirable dynamics can still be encountered even when a flutter outcome is relatively benign. Thus, the effects of flexibility *must be adequately captured* in the analysis and design of high-aspect-ratio wings.

2. **Properties of a linearised system can help predict the nonlinear dynamics**

   As was established in Chapter 2, flutter describes a static, aeroelastic equilibrium losing oscillatory stability to small perturbations; thus, it is a local phenomenon, where the underlying physical mechanisms are prescribed by the linearised characteristics of the system. Once a nonlinear system deforms, the dynamics are no longer strictly governed by these characteristics; however, insight can nevertheless be gained by maintaining a 'quasi-linear' view, even for complex cases. LCOs can generally be characterised in terms of linearised modes, and as shown in Chapter 3, indications of Hopf criticality can be found by inspecting the mode variation in traditional frequency/damping plots. Thus, while obtaining the complete behaviour of a high-aspect-ratio wing necessitates the use of nonlinear techniques, indicators can be found in the linearised properties.

3. **Uncertainties in structural damping could be important**

   Structural damping is a notoriously difficult property to quantify. Indeed, when flutter analysis is conducted within industry, the effects of structural damping are sometimes neglected, the intention being to obtain a 'worst-case' boundary prediction, to which a predetermined safety margin may then be applied. While this strategy is perfectly applicable if the wing is assumed linear (i.e. sufficiently rigid), the possibility of detrimental LCOs in high-aspect-ratio wings means that it *must be used with caution*. Given the relationship between damping and flutter criticality shown in Chapter 3, uncertainty in damping, which would lead to uncertainty in the flutter airspeed, could result in an erroneous supercritical/subcritical Hopf prediction. The risk of this is clearly greatest in cases where the Hopf is nominally close to the degenerate case, or where there is a rapid variation in the linearised modes caused by the geometric nonlinearity inherent in largely deformed equilibria.

While it is, theoretically, possible to construct a system where increasing the structural damping has a detrimental effect (i.e. it causes a supercritical Hopf to become subcritical, e.g. see two of the cases in Fig. 3.9), this was not observed in the more representative HALE wing investigated in Section 4.7; here, maximising the structural damping, which is typically desirable anyway for increasing the flutter airspeed, was also favourable with regards to Hopf criticality.

It should be noted that the above discussion also applies to the additional aerodynamic damping provided by unsteadiness; this will be discussed in Section 6.2.

4. **Numerical continuation techniques are appropriate methods**

   The nature of the dynamical phenomena shown in this work clearly demonstrates the applicability of continuation methods for the investigation of high-aspect-ratio wings. Detrimental phenomena were readily found in all cases; moreover, very complex LCO behaviours were revealed, particularly in Chapter 4). Thus, continuation techniques (or path-following methods, in general) are the *only feasible means* of obtaining the complete dynamics of these systems. Furthermore, the coupling with the low-order beam formulation of Howcroft *et al.* [6] demonstrated that continuation is particularly effective for exploratory research, i.e. where the objective is to obtain the topological structure of the dynamics, over a very wide range of parameters (this was particularly true for the work in Chapter 3).

6.2 Extensions

There are several areas where further work may build on the findings of this thesis and yield interesting results. Suggested extensions are described below.

- **Aerodynamic nonlinearity (e.g. dynamic stall) could be investigated**

  As stated above, provided the aerodynamics are linear at the flutter condition of a nonlinear system, aerodynamics do not affect the criticality of the Hopf bifurcation. In all studies in this thesis, flutter occurs at low angles of attack; thus, the dynamics are topologically valid near the equilibrium. While aerodynamic nonlinearities are not essential for investigating the near-equilibria effects of geometric nonlinearity, they are clearly important for the capture of larger-amplitude LCOs, where spanwise sections may experience flow separation. It would be interesting to investigate whether the inclusion of the hysteresis effects relating to dynamic stall can lead to any detrimental, high-amplitude LCOs in a wing where the geometric nonlinearity prescribes a relatively benign and supercritical flutter point. This study could be achieved, using continuation, via the implementation of a *parameterised nonlinear aerodynamic model* that allows the continuation of periodic bifurcations with respect to, for example, stall angle. The sensitivity of the LCO solutions to uncertainty in the aerodynamic parameters could thus be investigated. Of course, any further studies that

more precisely target quantitative behaviour should include both nonlinear and unsteady aerodynamic effects as a necessity.

- **Unsteady aerodynamics effects should be included**

  In all studies within this thesis, quasi-steady aerodynamics (where the loads are a function of the effective angle of attack, with no unsteadiness) were implemented. For a given high-aspect-ratio wing, the effect of geometric nonlinearity does not change when linear unsteady aerodynamics are included; of course, the airspeed of the flutter point may be different (typically, it increases due to additional aerodynamic damping), but any resulting change in the nonlinear dynamics (i.e. the criticality of the Hopf bifurcation) is not caused by unsteadiness. Thus, the inclusion of unsteady aerodynamics is not a requisite for investigating the fundamental geometric nonlinearity that characterises high-aspect-ratio wings in isolation. For this reason, together with the extra computational costs of capturing aerodynamic states, unsteady effects were omitted; however, much like the effects of structural damping, unsteadiness must be modelled with low uncertainty in the future if precise predictions of behaviours are sought.

- **Trends relating flutter criticality to the convergence of modes could be tested experimentally**

  Further verification of the flutter criticality observations found in Chapter 3 is highly desirable, particularly if obtained empirically, e.g. by varying the structural damping of an experimental wing and observing a change of Hopf criticality that relates to the convergence of the linearised modes. Should this 'rule of thumb' become well-established, it would serve as a very useful tool in both the design and testing of flexible, high-aspect-ratio wings.

- **Body-freedom flutter, or asymmetric aircraft dynamics, could be investigated**

  An extension to the study in Chapter 5 may comprise varying the HALE configuration in a way that causes *body-freedom flutter* to occur; this could be achieved by altering the nominal aircraft parameters, such that the short-period frequency increases and moves closer to the flutter frequency of the wing. This frequency increase could be achieved by reducing the aircraft pitch inertia, which could be acheived by reducing the payload or shortening the fuselage, etc. Alternatively, a study of the *asymmetric* aeroelastic flight dynamics (i.e. including both longitudinal and lateral-directional dynamics) would be interesting, although this would require an individual set of shape functions for each wing, and hence would be more computationally expensive.

On a more general note, the application of numerical continuation in the study of high-aspect-ratio wings is not restricted to the typical objectives of flutter analysis. Fundamentally, the techniques seek to obtain the parameter-dependant behaviour of a given dynamical system; thus, their applicability is limited only by how adequately the system in question is parameterised. In

this thesis, the primary continuation parameter used in all studies was airspeed, and secondary parameters included structural properties, such as stiffness and damping. However, any of the parameters in a given wing may be used; for example, the root angle of attack, sweep angle, taper, span, stiffness distribution etc. could all be used as primary or secondary continuation parameters, and may yield interesting results. As noted above, the use of a parameterised aerodynamic model could provide insight into how wing behaviour may be affected by uncertainties in the lift/stall profile. The benefit of using continuation, in this context, is that the most critical parameters, i.e. those which the dynamics are most sensitive to, can be readily identified; thus, use of techniques can direct the focus of more computationally expensive, high-fidelity studies (e.g. FEA, CFD).

6.3 General outlook

Regarding the general question of whether continuation techniques (or more broadly, nonlinear dynamical systems approaches) can be impactful on the design of high-aspect-ratio wings, it is clear that several obstacles must be overcome first. Civil aviation is a *highly conservative* engineering environment, for obvious reasons; not only must new technologies present a convincing business case ('buy their way' onto an aircraft), they must also comply with the stringent airworthiness regulations that ensure passenger safety. Flutter phenomena are treated with particular caution, due to the unbounded, catastrophic failure predicted by linear methods, so central use of nonlinear tools in this area would likely necessitate significant amendments to existing regulations (for example, see EASA CS 25.629 - 'aeroelastic stability requirements'[1]), or the formulation of new ones, which may demand extensive evidence of empirical data verifying numerical predictions. The tests required by new regulations would likely be significant engineering challenges in and of themselves; the pursuit of nonlinear behaviour in a real-life system is potentially dangerous, so the costly development of novel experimental techniques might be necessary. Consequently, it is likely that nonlinear approaches would have to permeate *multiple* areas of the engineering lifecycle before continuation techniques can make sizeable impacts in design. This industry conservatism is also compounded by the fact that i) nonlinear dynamics are not a core part of undergraduate engineering courses, and ii) there is no production-ready, easy-to-use software that can readily be used with industry models for continuation analysis (although, an important step towards addressing this second point is detailed in Sharma *et al.* [56], which describes a toolbox that enabled use of AUTO for the analysis of Simulink-based Airbus landing gear models).

Currently, the virtues of nonlinear approaches are not easily visible to those without specialist expertise; thus, to facilitate more widespread use of continuation techniques, the key is to make the potential applications more tangible. Presently, points of entry are likely to only be instances when nonlinear analysis is unavoidable, i.e. where detrimental nonlinearity is found after a

[1] https://www.easa.europa.eu/document-library/certification-specifications (last accessed on 24th February 2019).

design solution has been frozen. An example of this could be the discovery of unwanted shimmy oscillations (i.e. LCOs), in an existing landing gear system, and the subsequent use of nonlinear tools for the retrofitting of a damping device. This use of nonlinearity would be entirely *reactive*, however, and is less applicable to the safety-critical design of wings; should a wing exhibit detrimental nonlinear phenomena (e.g. subcritical LCOs) in, say, flight test, it is likely that a solution/redesign would be found using established linear methods, rather than nonlinear analysis.

Further to the above, another potential issue that may hinder the use of continuation techniques in industry may lie in methods themselves. An important requirement for the success of continuation methods is the sufficient *smoothness* of the dynamical system in question, i.e. the existence of enough continuous derivatives, to enable the traversing of solution curves. Due to this requirement, empirically-obtained aerodynamic data, which is typically stored in tabulated form, may necessitate the fitting of a smooth function, resulting in a loss of information. This type of compromise would similarly apply to models featuring feedback control systems, where discontinuities or discrete control laws may be present. A further limitation commonly attributed to continuation is the requirement of low-order models; while it is true that the methods are most effective when coupled with simple systems, this can be said of any analysis technique. The use of continuation with a high-fidelity, nonlinear FE model of a high-aspect-ratio wing would indeed be computationally expensive; nevertheless, it would still be the most efficient means of obtaining the parameter-dependant dynamics when compared to other methods (e.g. time histories).

Despite the above reservations, there are reasons to be optimistic about the future role of continuation techniques in industry. Recent textbooks on both nonlinear aeroelasticity (Dimitriadis [30]) and flight dynamics (Sinha & Ananthkrishnan [48]) include detailed discussions of continuation in applied aerospace contexts; thus, there are encouraging signs that awareness of the methods may become more commonplace amongst non-specialist engineers. Importantly, in the particular area of flexible wing aeroelastics, there is clearly scope for *exploiting nonlinearity* in the context of flutter; if nonlinear tools are used to ensure that the flutter point is supercritical, they could facilitate the use of an active LCO suppression system, which could substantially extend the aircraft flight envelope. Compared to reactive uses of nonlinear analysis (e.g. the aforementioned example of landing gear shimmy), this type of 'enhancing' impact is far more likely to garner interest, as it presents compelling opportunities for *performance benefit* and hence a competitive advantage. Provided the aerodynamic benefits of high-aspect-ratio wings remain an attraction for aircraft designers, and the aeroelastic behaviours of flexible wings with geometric nonlinearity are better understood through research, there will likely be strong incentives for the development of LCO suppression technology using nonlinear methods.

APPENDIX

A.1 Hodges & Dowell model

The original Hodges & Dowell [68] beam equations, discussed in Section 2.4.1, can be written as

$$EI_2 v'''' + (EI_2 - EI_1)\big(\phi(w+w_0)''\big)'' + m\ddot{v} + M\ddot{v}_{x=L} = \frac{\mathrm{d}F_v}{\mathrm{d}x},$$

$$EI_1(w+w_0)'''' + (EI_2 - EI_1)\big(\phi v''\big)'' + m\ddot{w} + M\ddot{w}_{x=L} - Mg\delta(x-L) = \frac{\mathrm{d}F_w}{\mathrm{d}x},$$

$$GJ\phi'' + (EI_2 - EI_1)(w+w_0)''v'' + mK_m^2\ddot{\phi} = \frac{\mathrm{d}M_x}{\mathrm{d}x},$$

where the symbols are defined in Table A.1.

Table A.1: Symbols of the Hodges-Dowell model.

Symbol	***Definition***
$\mathrm{d}F_v$, $\mathrm{d}F_x$	Section chordwise and vertical component forces
$\mathrm{d}M_x$	Section pitch moment about elastic axis
E	Modulus of elasticity
g	Gravitational constant
G	Shear modulus
I_1, I_2	Vertical, chordwise moments of area
J	Torsional stiffness constant
K_m	Wing mass radius of gyration
L	Wing span
m	Mass per unit length
M	Tip mass
v	Chordwise bending deflection
w	Vertical bending deflection
x	Position coordinate along wing span
ϕ	Twist about deformed elastic axis

A.2 Additional terms from Howcroft *et al.*

The terms M and w in equation (4.21) can be expressed as

$$\boldsymbol{M} = \int_0^L m(s)\left(\frac{\partial r_{m[G]}}{\partial q}\right)^T\left(\frac{\partial r_{m[G]}}{\partial q}\right) + \left(\frac{\partial \vartheta_{[G]}}{\partial q}\right)^T \mathbf{e}_{[G]} I_{\vartheta[I]} \mathbf{e}_{[G]}^T \left(\frac{\partial \vartheta_{[G]}}{\partial q}\right) \mathrm{d}s, \tag{A.1}$$

$$\boldsymbol{w} = \int_0^L m(s)\left(\frac{\partial r_{m[G]}}{\partial q}\right)^T \ddot{r}^*_{m[G]} + \left(\frac{\partial \vartheta_{[G]}}{\partial q}\right)^T \dot{\mathbf{e}}_{[G]} I_{\vartheta[I]} \mathbf{e}_{[G]}^T \dot{\vartheta}_{[G]} + \left(\frac{\partial \vartheta_{[G]}}{\partial q}\right)^T \mathbf{e}_{[G]} I_{\vartheta[I]} \mathbf{e}^*_{[G]} \ddot{\vartheta}^*_{[G]} \, \mathrm{d}s. \tag{A.2}$$

Details of the steps required to obtain this expressions, and expressions for $\ddot{r}^*_{m[G]}$ and $\ddot{\vartheta}^*_{[G]}$, can be found in Ref. [6].

A.3 Beam frequency formulae

The formulae for the natural frequencies of a uniform beam, fixed at one end, can be derived from e.g. Ref. [113] and are stated here for completeness.

The bending frequencies are given by

$$\omega_n = \alpha_n^2 \sqrt{\frac{EI}{mL^4}},$$

where m is the mass per unit length, L is total length of the beam, and EI is the bending stiffness. The first three bending modes are obtained using $\alpha_1 = 1.875$, $\alpha_2 = 4.694$, and $\alpha_3 = 7.885$. The fundamental torsional frequency can be obtained using

$$\omega_1 = \frac{\pi}{2L}\sqrt{\frac{GJ}{I}},$$

where I is the inertia per unit length, and GJ is the torsional stiffness. In each case, division by 2π obtains the frequencies in Hz.

BIBLIOGRAPHY

[1] F. Alfonso, J. Vale, E. Oliveira, F. Lau, and A. Suleman, "A review on non-linear aeroelasticity of high aspect-ratio wings," *Progress in Aerospace Sciences*, no. 89, pp. 40–57, 2017.

[2] M. K. Bradley and C. K. Droney, "Subsonic ultra green aircraft research phase ii: N+ 4 advanced concept development," *NASA/CR-2012-217556*, pp. 111–123, 2012.

[3] T. Strganac, P. Cizmas, C. Nichkawde, J. Gargoloff, and P. Beran, "Aeroelastic analysis for future air vehicle concepts using a fully nonlinear methodology," in *46th AIAA/ASME/ASCE/AHS/ASC Structures, Structural Dynamics and Materials Conference, Austin, Texas*, AIAA 2005-2171, 2005.

[4] A. J. Eaton, C. Howcroft, E. B. Coetzee, S. A. Neild, M. H. Lowenberg, and J. E. Cooper, "Numerical continuation of limit cycle oscillations and bifurcations in high-aspect-ratio wings," *Aerospace*, vol. 5(3), 78, 2018.

[5] A. J. Eaton, C. Howcroft, S. A. Neild, M. H. Lowenberg, J. E. Cooper, and E. B. Coetzee, "Flutter in high aspect ratio wings using numerical continuation," in *Proceedings of Royal Aeronautical Society 5th Structural Design Conference, Manchester, UK*, 2016.

[6] C. Howcroft, R. G. Cook, S. A. Neild, M. H. Lowenberg, J. E. Cooper, and E. B. Coetzee, "On the geometrically exact low-order modelling of a flexible beam: formulation and numerical tests," *Proceedings of the Royal Society A: Mathematical, Physical and Engineering Sciences*, vol. 474, no. 20180423, 2018.

[7] Y. Kuznetsov, *Elements of Applied Bifurcation Theory*.
Springer Science & Business Media, 3 ed., 2013.

[8] J. Guckenheimer and P. Holmes, *Nonlinear oscillations, dynamical systems, and bifurcations of vector fields*.
Springer Science & Business Media, 1 ed., 2013.

[9] S. Wiggins, *Introduction to applied nonlinear dynamical systems and chaos*.
Springer Science & Business Media, 2 ed., 2003.

[10] S. Strogatz, *Nonlinear Dynamics and Chaos with Applications to Physics, Biology, Chemistry and Engineering*.
CRC Press, 1 ed., 1994.

[11] R. L. Bisplinghoff, H. Holt, and R. L. Halfman, *Aeroelasticity*.
Courier Corporation, 2013.

[12] Y. C. Fung, *An Introduction to the Theory of Aeroelasticity*.
Courier Dover Publications, 2008.

[13] D. H. Hodges and G. A. Pierce, *Introduction to Structural Dynamics and Aeroelasticity*.
Cambridge, 2 ed., 2011.

[14] J. R. Wright and J. E. Cooper, *Introduction to Aeroelasticity and Loads*.
Wiley, 2 ed., 2014.

[15] R. W. H. Scanlan, "Developments in low-speed aeroelasticity in the civil engineering field," *AIAA Journal*, vol. 20, no. 6, pp. 839–844, 1982.

[16] H. Pomin and S. Wagner, "Aeroelastic analysis of helicopter rotor blades on deformable chimera grids," *Journal of Aircraft*, vol. 41, no. 3, pp. 577–584, 2004.

[17] Q. Xiao and Q. Zhu, "A review on flow energy harvesters based on flapping foils," *Journal of Fluids and Structures*, vol. 46, pp. 174–191, 2014.

[18] R. Beck, M. Odeh, A. Oliven, and N. Gavriely, "The acoustic properties of snores," *European Respiratory Journal*, vol. 8, no. 12, pp. 2120–2128, 1995.

[19] A. R. Collar, "The first fifty years of aeroelasticity," *Aerospace (Royal Aeronautical Society Journal)*, vol. 5, no. 2, pp. 12–20, 1978.

[20] P. P. Friedmann, "Renaissance of aeroelasticity and its future," *Journal of Aircraft*, vol. 36, no. 1, pp. 105–121, 1999.

[21] I. E. Garrick and W. H. Reed, "Historical development of aircraft flutter," *Journal of Aircraft*, vol. 18, no. 11, pp. 817–912, 1981.

[22] R. E. Bartels, C. J. Funk, and R. C. Scott, "Limit-cycle oscillation of the subsonic ultra-green aircraft research truss-braced wing aeroelastic model," *Journal of Aircraft*, vol. 54, no. 5, pp. 1605–1613, 2017.

[23] C. P. Szczyglowski, S. A. Neild, B. Titurus, J. Z. Jiang, and E. B. Coetzee, "Passive gust load alleviation in a truss-braced wing using an inerter-based device," in *2018 AIAA/ASCE/AHS/ASC Structures, Structural Dynamics, and Materials Conference, Orlando, Florida*, AIAA 2018-1958, 2018.

[24] A. Castrchini, V. Siddaramaiah, D. E. Calderon, J. E. Cooper, T. Wilson, and Y. Lemmens, "Nonlinear folding wing tips for gust loads alleviation," *Journal of Aircraft*, vol. 53, no. 5, pp. 1391—1399, 2016.

[25] O. Stodieck, J. E. Cooper, P. M. Weaver, and P. Kealy, "Improved aeroelastic tailoring using tow-steered composites," *Composite Structures*, vol. 106, pp. 703–715, 2013.

[26] K. Y. Billah and R. W. H. Scanlan, "Resonance, tacoma narrows bridge failure, and undergraduate physics textbooks," *American Journal of Physics*, vol. 59, no. 2, pp. 118–124, 1991.

[27] E. Livne, "Aircraft active flutter suppression: State of the art and technology maturation needs," *Journal of Aircraft*, vol. 55, no. 1, pp. 410–451, 2018.

[28] K. G. Bhatia, "Airplane aeroelasticity: Practice and potential," *Journal of Aircraft*, vol. 40, no. 6, pp. 1010–1018, 2003.

[29] R. Seydel, *Practical Bifurcation and Stability Analysis*.
Springer, 3 ed., 2010.

[30] G. Dimitriadis, *Introduction to Nonlinear Aeroelasticity*.
Wiley, 2017.

[31] F. O. Carta, "An analysis of the stall flutter instability of helicopter rotor blades," *Journal of the American Helicopter Society*, vol. 12, no. 4, pp. 1–18, 1967.

[32] W. Govaerts, Y. Kuznetsov, and B. Sijnave, "Numerical methods for the generalized hopf bifurcation," *Society for Industrial and Applied Mathematics*, vol. 38, no. 1, pp. 329–346, 2005.

[33] E. H. Dowell, J. Edwards, and T. Strganac, "Nonlinear aeroelasticity," *Journal of Aircraft*, vol. 40, no. 5, pp. 857–874, 2003.

[34] B. H. K. Lee, S. J. Price, and Y. S. Wong, "Nonlinear aeroelastic analysis of airfoils: bifurcations and chaos," *Progress in Aerospace Sciences*, vol. 35, no. 5, pp. 205–334, 1999.

[35] E. L. Allgower and K. Georg, *Numerical Continuation Methods: An introduction*.
Springer, 1990.

[36] E. J. Doedel, H. B. Keller, and J. P. Kernevez, "Numerical analysis and control of bifurcation problems I Bifurcation in finite dimensions," *International Journal of Bifurcation and Chaos*, no. 1, pp. 493–520, 1991.

[37] E. J. Doedel, H. B. Keller, and J. P. Kernevez, "Numerical analysis and control of bifurcation problems II Bifurcation in infinite dimensions," *International Journal of Bifurcation and Chaos*, no. 1, pp. 745–772, 1991.

[38] B. Krauskopf, H. Osinga, and J. Galán-Vioque, *Numerical Continuation Methods for Dynamical Systems*.
Canopus Publishing Ltd., 2007.

[39] W. J. F. Govaerts, *Numerical Methods for Bifurcations of Dynamical Equilibria*.
Society for Industrial and Applied Mathematics, 2000.

[40] E. J. Doedel, "AUTO: A program for the automatic bifurcation analysis of autonomous systems," *Congressus Numerantium*, vol. 30, pp. 265–284, 1981.

[41] E. J. Doedel, A. Champneys, T. Fairgieve, Y. Kuznetsov, B. Sandstede, and X. Wang, "AUTO 97: Continuation and bifurcation software for ordinary differential equations (with HomCont)," *Concordia University, Canada*, 1997.

[42] E. J. Doedel, R. Paffenroth, A. Champneys, T. Fairgieve, Y. Kuznetsov, B. Oldeman, B. Sandstede, and X. Wang, "AUTO 2000: Continuation and bifurcation software for ordinary differential equations (with HomCont)," *California Institute of Technology, USA*, 2000.

[43] W. Govaerts, Y. Kuznetsov, and A. Dhooge, "Numerical continuation of bifurcations of limit cycles in Matlab," *SIAM Journal on Scientific Computing*, vol. 27, no. 1, pp. 231–252, 2005.

[44] E. Coetzee, B. Krauskopf, and M. Lowenberg, "The Dynamical Systems Toolbox: integrating AUTO into MATLAB," in *16th US National Congress of Theoretical and Applied Mechanics, State College, Pennsylvania*, 2010.

[45] H. Dankowicz and F. Schilder, *Recipes for Continuation*.
Society for Industrial and Applied Mathematics (SIAM), 2013.

[46] M. Goman, G. Zagainov, and A. Khramtsovsky, "Application of bifurcation methods to nonlinear flight dynamics problems," *Progress in Aerospace Sciences*, vol. 33, no. 9-10, pp. 539–586, 1997.

[47] J. Thompson, *Nonlinear Flight Dynamics of High-performance Aircraft: A Theme*.
Royal Society, 1998.

[48] N. Sinha and N. Ananthkrishnan, *Elementary flight dynamics with an introduction to bifurcation and continuation methods*.
CRC Press, 2016.

[49] C. Howcroft, B. Krauskopf, M. H. Lowenberg, and S. A. Neild, "Influence of variable sidestay geometry on the shimmy dynamics of an aircraft dual-wheel main landing gear," *SIAM Journal on applied dynamical systems*, vol. 12, no. 3, pp. 1181–1209, 2013.

[50] H. Alighanbari and S. J. Price, "The post-hopf-bifurcation response of an airfoil in incompressible two-dimensional flow," *Nonlinear Dynamics*, vol. 10, no. 4, pp. 381–400, 1996.

[51] G. Dimitriadis, "Continuation of higher-order harmonic balance solutions for nonlinear aeroelastic systems," *Journal of Aircraft*, vol. 45, no. 2, pp. 523–537, 2008.

[52] G. Dimitriadis, "Bifurcation analysis of aircraft with structural nonlinearity and freeplay using numerical continuation," *Journal of Aircraft*, vol. 45, no. 3, pp. 893–905, 2008.

[53] G. Dimitriadis, "Shooting-based complete bifurcation prediction for aeroelastic systems with freeplay," *Journal of Aircraft*, vol. 48, no. 6, pp. 1864–1877, 2011.

[54] G. A. Vio, G. Dimitriadis, and J. Cooper, "Bifurcation analysis and limit cycle oscillation amplitude prediction methods applied to the aeroelastic galloping problem," *Journal of Fluids and Structures*, vol. 23, no. 7, pp. 983–1011, 2007.

[55] H. Shukla and M. J. Patil, "Nonlinear state feedback control design to eliminate subcritical limit cycle oscillations in aeroelastic systems," *Nonlinear Dynamics*, vol. 88, no. 3, pp. 1599–1614, 2017.

[56] S. Sharma, E. B. Coetzee, M. H. Lowenberg, S. A. Neild, and B. Krauskopf, "Numerical continuation and bifurcation analysis in aircraft design: an industrial perspective," *Phil. Trans. R. Soc. A*, vol. 373, no. 20140406, 2015.

[57] D. Rezgui, M. H. Lowenberg, M. Jones, and C. Monteggia, "Continuation and bifurcation analysis in helicopter aeroelastic stability problems," *Journal of Guidance, Control, and Dynamics*, vol. 37, no. 3, pp. 889–897, 2014.

[58] M. Jones, A. Bernascone, P. Masarati, G. Quaranta, and D. Rezgui, "Ongoing developments in the use of continuation/bifurcation methodology at AugustaWestland," *Proceedings of 40th European Rotorcraft Forum, Southampton, UK*, 2014.

[59] D. A. Barton, "Control-based continuation: bifurcation and stability analysis for physical experiments," *Mechanical Systems and Signal Processing*, vol. 84, pp. 54–64, 2017.

[60] L. Renson, A. Gonzalez-Buelga, D. Barton, and S. Neild, "Robust identification of backbone curves using control-based continuation," *Journal of Sound and Vibration*, vol. 367, pp. 145–158, 2016.

[61] C. De Boor and B. Swartz, "Collocation at Gaussian points," *SIAM Journal on Numerical Analysis*, vol. 10, no. 4, pp. 582–606, 1973.

[62] E. H. Dowell and D. Tang, "Nonlinear aeroelasticity and unsteady dynamics," *AIAA Journal*, vol. 40, no. 9, pp. 1697–1707, 2002.

[63] E. H. Dowell, *A Modern Course in Aeroelasticity*.
Springer, 5 ed., 2015.

[64] E. H. Dowell, "Some recent advances in nonlinear aeroelasticity: fluid-structure interaction in the 21st century," in *51st AIAA/ASME/ASCE/AHS/ASC Structures, Structural Dynamics, and Materials Conference, Orlando, Florida*, AIAA 2010-3137, 2010.

[65] M. J. C. Henshaw, K. J. Badcock, G. A. Vio, C. B. Allen, J. Chamberlain, I. Kaynes, G. Dimitriadis, J. E. Cooper, M. A. Woodgate, A. M. Rampurawala, *et al.*, "Non-linear aeroelastic prediction for aircraft applications," *Progress in Aerospace Sciences*, vol. 43, no. 4-6, pp. 65–137, 2007.

[66] E. Livne, "Future of airplane aeroelasticity," *Journal of Aircraft*, vol. 40, no. 6, pp. 1066–1092, 2003.

[67] J. Xiang, Y. Yan, and D. Li, "Recent advance in nonlinear aeroelastic analysis and control of the aircraft," *Chinese Journal of Aeronautics*, vol. 27, no. 1, pp. 12–22, 2014.

[68] D. H. Hodges and E. H. Dowell, "Nonlinear equations of motion for the elastic bending and torsion of twisted nonuniform rotor blades," *NASA/ TN D-7818*, 1974.

[69] C. T. Tran and D. Petot, "Semi-empirical model for the dynamic stall of airfoils in view of the application to the calculation of responses of a helicopter blade in forward flight," *Vertica*, vol. 5, no. 1, pp. 35–53, 1981.

[70] M. J. Patil, D. H. Hodges, and C. E. S. Cesnik, "Characterizing the effects of geometrical nonlinearities on aeroelastic behaviour of high-aspect-ratio wings," *International Forum on Aeroelasticity and Structural Dynamics, Williamsburg, Virginia, USA*, June 1999.

[71] M. J. Patil, D. H. Hodges, and C. E. S. Cesnik, "Nonlinear aeroelasticity and flight dynamics of high-altitude long-endurance aircraft," *Journal of Fluids and Structures*, vol. 38, pp. 88–94, 2001.

[72] M. J. Patil and D. H. Hodges, "On the importance of aerodynamic and structural geometrical nonlinearities in aeroelastic behaviour of high-aspect-ratio wings," *Journal of Fluids and Structures*, vol. 19, no. 19, pp. 905–915, 2004.

[73] M. J. Patil, D. H. Hodges, and C. E. S. Cesnik, "Limit-cycle oscillations in high-aspect-ratio wings," *Journal of Fluids and Structures*, vol. 15, no. 1, pp. 107–132, 2001.

[74] D. Tang and E. H. Dowell, "Experimental and theoretical study on aeroelastic response of high-aspect-ratio wings," *AIAA Journal*, vol. 39, no. 8, pp. 1430–1441, 2001.

[75] D. Tang and E. H. Dowell, "Limit-cycle hysteresis response for a high-aspect-ratio wing model," *AIAA Journal*, vol. 39, no. 8, pp. 885–888, 2002.

[76] D. Tang and E. H. Dowell, "Effects of geometric structural nonlinearity on flutter and limit cycle oscillations of high-aspect-ratio wings," *Journal of Fluids and Structures*, vol. 19, no. 3, pp. 291–306, 2004.

[77] D. Tang and E. H. Dowell, "Experimental and theoretical study of gust response for high-aspect-ratio wing," *AIAA Journal*, vol. 40, no. 3, pp. 419–429, 2002.

[78] D. H. Hodges, "A mixed variation formulation based on exact intrinsic equations for dynamics of moving beams," *Internal Journal of Solids and Structures*, vol. 26, pp. 1253–1273, 1990.

[79] B. Stanford and P. Beran, "Direct flutter and limit cycle computations of highly flexible wings for efficient analysis and optimization," *Journal of Fluids and Structures*, vol. 36, pp. 111–123, 2013.

[80] J. W. Jaworski, "Nonlinear aeroelastic analysis of flexible high aspect ratio wings including correlation with experiment," *PhD thesis, Duke University*, 2009.

[81] K. Eskandary, M. Dardel, M. H. Pashaei, and A. K. Moosavi, "Nonlinear aeroelastic analysis of high-aspect-ratio wings in low subsonic flow," *Acta Astronautica*, vol. 70, pp. 6–22, 2012.

[82] D. H. Hodges, "Geometrically exact, intrinsic theory for dynamics of curved and twisted anisotropic beams," *AIAA Journal*, vol. 41, no. 6, pp. 1131–1137, 2003.

[83] M. C. D. Silva, "Non-linear flexural-flexural-torsional-extensional dynamics of beams—I. Formulation," *International Journal of Solids and Structures*, vol. 24, no. 12, pp. 1225–1234, 1988.

[84] J. G. Leishman and K. Q. Nguyen, "State space representation of unsteady airfoil behaviour," *AIAA Journal*, vol. 28, no. 5, pp. 836–844, 1990.

[85] J. G. Leishman and T. S. Beddoes, "A semi-empirical model for dynamic stall," *Journal of the American Helicopter Society*, vol. 34, no. 3, pp. 3–17, 1989.

[86] F. Afonso, G. Leal, J. Vale, E. Oliveira, F. Lau, and A. Suleman, "The effect of stiffness and geometric parameters on the nonlinear aeroelastic performance of high aspect ratio wings," *Proceedings of the Institution of Mechanical Engineers, Part G: Journal of Aerospace Engineering*, vol. 231, no. 10, pp. 1824–1850, 2017.

[87] F. Afonso, J. Vale, E. Oliveira, F. Lau, and A. Suleman, "Non-linear aeroelastic response of high aspect-ratio wings in the frequency domain," *The Aeronautical Journal*, vol. 121, no. 1240, pp. 858–876, 2017.

[88] A. Arena, W. Lacarbonara, and P. Marzocca, "Nonlinear aeroelastic formulation and post-flutter analysis of flexible high-aspect-ratio wings," *Journal of Aircraft*, vol. 50, no. 6, pp. 1748–1764, 2013.

[89] J. Zhang and J. Xiang, "Nonlinear aeroelastic response of high-aspect-ratio flexible wings," *Chinese Journal of Aeronautics*, vol. 22, no. 4, pp. 355–363, 2009.

[90] K. Kim and T. Strganac, "Nonlinear responses of a cantilever wing with an external store," in *44th AIAA/ASME/ASCE/AHS/ASC Structures, Structural Dynamics, and Materials Conference, Norfolk, Virginia*, AIAA 2003-1708, 2003.

[91] C. Howcroft, S. A. Neild, M. H. Lowenberg, and J. E.Cooper, "Efficient aeroelastic beam modelling and the selection of a structural shape basis," *International Journal of Non-Linear Mechanics*, vol. 112, pp. 73–84, 2019.

[92] C. Howcroft, D. Calderon, L. Lambert, M. Castellani, J. E. Cooper, M. H. Lowenberg, and S. A. Neild, "Aeroelastic modelling of highly flexible wings," in *AIAA 15th Dynamics Specialists Conference, San Diego, California*, AIAA 2016-1798, 2016.

[93] D. A. Peters and M. J. Johnson, "Finite-state airloads for deformable airfoils on fixed and rotating wings," *Aeroelasticity and Fluid/Structure Interaction*, vol. 44, pp. 1–28, 1994.

[94] D. A. Peters, S. Karunamoorthy, and W. M. Cao, "Finite-state induced flow models Part I: two-dimensional thin airfoil," *Journal of Aircraft*, vol. 32, pp. 313—322, 1995.

[95] L. Roskam, *Airplane flight dynamics and automatic flight controls*. DARcorporation, 1998.

[96] M. G. Goman, G. I. Zagainov, and A. V. Khramtsovsky, "Application of bifurcation methods to nonlinear flight dynamics problems," *Progress in Aerospace Sciences*, vol. 33, no. 9-10, pp. 539–586, 1997.

[97] M. G. Goman and A. V. Khramtsovsky, "Application of continuation and bifurcation methods to the design of control systems," *Proceedings of the Royal Society A: Mathematical, Physical and Engineering Sciences*, pp. 2277–2296, 1998.

[98] J. V. Carroll and R. K. Mehra, "Bifurcation analysis of nonlinear aircraft dynamics," *Journal of Guidance, Control, and Dynamics*, vol. 5, no. 5, pp. 529–536, 1982.

[99] S. J. Gill, M. H. Lowenberg, S. A. Neild, B. Krauskopf, G. Puyou, and E. Coetzee, "Upset dynamics of an airliner model: a nonlinear bifurcation analysis," *Journal of Aircraft*, vol. 50, no. 6, pp. 1832–1842, 2013.

[100] M. C. V. Schoor and A. H. von Flotow, "Aeroelastic characteristics of a highly flexible aircraft," *Journal of Aircraft*, vol. 27, no. 10, pp. 901–908, 1990.

[101] M. Drela, "Integrated simulation model for preliminary aerodynamic, structural and control-law design of aircraft," *AIAA Journal*, vol. 99, no. 1, 1999.

[102] M. J. Patil and D. H. Hodges, "Flight dynamics of highly flexible flying wings," *Journal of Aircraft*, vol. 43, no. 6, pp. 1790–1799, 2006.

[103] C. M. Shearer and C. E. S. Cesnik, "Nonlinear flight dynamics of very flexible aircraft," *Journal of Aircraft*, vol. 44, no. 5, pp. 1528–1545, 2007.

[104] C. E. S. Cesnik and W. Su, "Nonlinear aeroelastic modeling and analysis of fully flexible aircraft," in *46th AIAA/ASME/ASCE/AHS/ASC Structures, Structural Dynamics and Materials Conference, Austin, Texas*, AIAA 2005-2169, 2005.

[105] R. Palacios, J. Murua, and R. Cook, "Structural and aerodynamic models in nonlinear flight dynamics of very flexible aircraft," *AIAA Journal*, vol. 48, no. 11, pp. 2648–2659, 2010.

[106] Z. Zhao and G. Ren, "Multibody dynamic approach of flight dynamics and nonlinear aeroelasticity of flexible aircraft," *AIAA Journal*, vol. 49, no. 1, pp. 41–54, 2011.

[107] J. Murua, R. Palacios, and J. M. R. Graham, "Applications of the unsteady vortex-lattice method in aircraft aeroelasticity and flight dynamics," *Progress in Aerospace Sciences*, vol. 55, pp. 46–72, 2012.

[108] H. Hesse, R. Palacios, and J. Murua, "Consistent structural linearization in flexible aircraft dynamics with large rigid-body motion," *AIAA Journal*, vol. 52, no. 3, pp. 528–538, 2014.

[109] T. Weisshaar and T. Zeiler, "Dynamic stability of flexible forward swept wing aircraft," *Journal of Aircraft*, vol. 20, no. 12, pp. 1014–1020, 1983.

[110] M. Love, P. Zink, P. Wieselmann, and H. Youngren, "Body freedom flutter of high aspect ratio flying wings," in *46th AIAA/ASME/ASCE/AHS/ASC Structures, Structural Dynamics and Materials Conference, Austin, Texas*, AIAA 2005-1947, 2005.

[111] W. Su and C. E. S. Cesnik, "Nonlinear aeroelasticity of a very flexible blended-wing-body aircraft," *Journal of Aircraft*, vol. 47, no. 5, pp. 1539–1553, 2010.

[112] A. Cardona and M. Géradin, *Flexible multibody dynamics: a finite element approach*. John Wiley, 2001.

[113] C. M. Harris and A. G. Piersol, *Harris' shock and vibration handbook*, vol. 5. McGraw-Hill New York, 2002.